On the transition from nuclear matter to finite nuclei

Dissertation

Zur Erlangung des Grades eines Doktors
der Naturwissenschaften
der Fakultät für Mathematik und Physik
der Eberhard-Karls-Universität zu Tübingen

vorgelegt von

Pavlo Grygorov
aus Kupyansk, der Ukraine

2010

to Punya
to my Parents

Contents

Chapter 1

Introduction

In 1932, Sir James Chadwick after a series of experiments suggested a hypothesis of the existence of the neutron [Ch32]. His discovery gave rise to a new branch of natural science – physics of atomic nuclei. Soon thereafter Ivanenko and Heisenberg independently proposed a proton-neutron model of nuclear structure [Iv32]. Already in 1936 a significant success in the description of binding energies of nuclei was achieved on the basis of the semi-empirical mass formula by Bethe and Weizsäcker. Since then the main question lying at the heart of nuclear physics still remains the same: What is the origin of the nucleon-nucleon (NN) interaction? A big step towards the understanding of the nature of nuclear forces was made by Yukawa. Following his idea the interaction between two nucleons is mediated by the exchange of massive particles. Nowadays the one-pion exchange model is used in the modern realistic NN forces for the description of the long-range part of the interaction.

From the underlying theory of the strong interaction, quantum chromodynamics (QCD), it became obvious that the NN interaction is not fundamental. However due to the non-perturbative character of QCD in the low-energy regime the rigorous derivation of the nucleon-nucleon interaction starting from the quark-gluon dynamics remains obscure. The so-called realistic models used instead, based on fitting of the scattering phase shifts, describe the interaction between nucleons neglecting the quark degrees of freedom. Another promising way to describe the bulk properties of finite nuclei over the whole periodic table is to construct a pure phenomenological density-dependent force, like Skyrme or Gogny. All these models of the nucleon-nucleon interaction, fitted to the properties of nucleons in vacuum as well as the

experimental data of finite nuclei should yield predictions for nuclear systems under extreme conditions. During the past several decades the properties of the matter under high densities and temperatures is one of the hottest topics both in theoretical and experimental nuclear physics. Exploring, e.g, the kaon production and the elliptical flow in heavy ion scattering experiments allows us to investigate the nuclear equation of state (EoS) at the high temperature and about 2-4 times nuclear saturation density. Such experiments with heavy ion beams is the only possible way to test the behavior of nuclear matter under extreme conditions in a laboratory. The alternative way for the experimental search is the observation of compact stars, like, radio pulsars, which are thought to be highly magnetized, rotating neutron stars emitting a beam of electromagnetic radiation at frequencies $10^8 - 10^{10}$ Hz. Thus the neutron stars (NS) are considered as natural astrophysical laboratories in the Universe.

Soon after Chadwick's experiment Landau theoretically predicted the star collapse, if the mass exceeds the critical value, known as the Chandrasekhar limit. Two years later, in 1934, Baade and Zwicky proposed a model of a neutron star as a remnant of the supernovae explosion [BZ34]. In 1967 Bell and Hewish discovered the regular radio pulsar CP1919 in the Crab Nebula, which was identified with an isolated, rotating neutron star. This event has ultimately confirmed that neutron stars really exist in nature and opened a new epoch in astrophysics. Nowadays about 2000 neutron stars have been discovered in the Milky Way and the Magellanic Clouds.

An ordinary star remains quasistatic for millions of years. During nearly all the lifetime of a star, the nuclear fusion reactions produce a thermal pressure which supports the star against the gravitational collapse. In the core of a star, hydrogen is fused into helium. After the hydrogen is exhausted the temperature is high enough to produce the carbon from helium fusion. In the stars with more than eight solar masses the fusion cycle continues until ^{56}Ni is produced. The later decays radioactively in a few months into ^{56}Co and then ^{56}Fe. Since iron has the highest binding energy per nucleon among all the elements, it cannot produce any more energy by fusion. At this point nothing can prevent the gravitational collapse. If the mass of the star exceeds the Chandrasekhar limit, it becomes energetically favorable for protons and electrons in the core to produce neutrons and neutrinos via the inverse beta decay. In this way the neutron rich core is formed. Finally the collapse is

stopped by the internal pressure of the degenerate neutron gas. Due to the low compressibility of the neutron rich core the in-falling matter rebounds, forming the shock wave propagating outwards. The surrounding outer core is blasted away by the shock wave, leaving a compact remnant – a young neutron star. A newly formed neutron star is very hot with temperatures as high as $T \sim 30 - 50$ MeV and a proton fraction of about 10 %. During the first seconds neutrinos are trapped within the star. Once the interior of the star cools down to the temperature of several MeV, the matter becomes transparent for neutrinos. The following cooling during the first thousand years is controlled by the neutrino emission. It is worth noting that the neutrino emission rates crucially depend on the matter composition.

A typical neutron star has the mass about M ~ 1.4 M$_\odot$ and the radius R ~ 10 km. The surface of NS is covered by a several centimeters thick atmosphere composed of hydrogen, helium, and other light elements. At the density of about $\rho = 10^6$ g cm^{-3} the matter consists of ^{56}Fe ions and electrons. In the density range $10^7 \leq \rho \leq 10^{11}$ g cm^{-3} (the outer crust) the matter consists of stable nuclei ^{62}Ni, ^{80}Zn, ^{82}Ge, ^{84}Se, ^{86}Kr, ^{120}Sr, ^{122}Zr, ^{124}Mo, and their isotopes. With increasing density, the nuclei become more and more neutron rich due to the electron capture which converts protons into neutrons. The chemical potential of neutrons rises and, finally, at the density $10^{11} \leq \rho \leq 10^{13}$ g cm^{-3} (the inner crust) some neutrons drip out of the nuclei. Therefore the nuclear matter consists of the neutron rich nuclei, the neutron sea and the relativistic degenerate electron gas. Further increase of the density leads to the spatial deformation of the nuclei. The cylindrical and planar quasi-nuclei may occur. These nonspherical quasi-nuclear structures are known as the pasta phase. The shape of the pasta is determined by the interplay between the Coulomb and surface energies. At the saturation density $\rho \simeq 2.4 \times 10^{14}$ g cm^{-3} the matter dissolves into a uniform mixture of protons, neutrons and electrons. The composition of the core of NS is still a matter of debate. Various theories predict the existence of hyperons, quark matter, pion and kaon condensate.

The question concerning the inhomogeneous structure of the crust is of fundamental interest for the NS cooling simulations and is tightly connected with the neutrino opacity. Since the crust of NS plays an important role in the neutrino transport, the occurrence of the pasta phase may significantly affect the neutrino opacity. One may expect that the scattering of neutrinos on the quasi-nuclei may reduce the neutrino

mean free path (NMFP) and change the cooling rate of the neutron stars. Therefore accurate calculations of the neutrino mean free path in the inhomogeneous crust are required.

In this Thesis the question of the neutrino propagation in the inhomogeneous nuclear matter is investigated by using the Hartree-Fock technique with the phenomenological Skyrme interaction as well as the density-dependent relativistic mean-field model. The calculations are performed within the cubic Wigner-Seitz (WS) cell, which allows to consider the nonspherical pasta phases. In the discussion of the pasta phase special attention is paid to its temperature stability. In the cooling simulations of the hot nuclear matter the knowledge of the critical temperature, at which the pasta may occur, is of high relevance. The neutrino mean free path in the inhomogeneous matter containing spherical droplets, cylindrical rods and planar slabs is extracted from the cross section on the WS cell [GGM10]. The scattering of neutrinos on the pasta structures is taken into account via the charged current absorption and neutral current scattering reactions. The dependence of the NMFP on the spatial distribution of the pasta phase are also highlighted.

The phenomenological interactions used to investigate the inhomogeneous nuclear matter in the crust of neutron stars have originally been adjusted to describe the experimental data for the ground states of the finite nuclei and the empirical saturation point of symmetric nuclear matter. A simple parameterization of such phenomenological forces through the local single-particle densities allows a simple solution of the Hartree-Fock (HF) equations [VB72]. In neutron stars, these models are extrapolated far from the condition where they have been adjusted and might in some cases become unstable [MNV02]. Thus the predictive power of such simple phenomenological approaches could be rather limited and their predictions for the nuclear matter calculations under extreme conditions may not be that reliable.

A possible way out of this problem is to investigate nuclear matter by using the realistic models of the NN interaction, fitted to the scattering data. A general feature of such realistic interactions is the strong short-range and tensor components, which cannot be handled within the standard perturbation theory. Different approaches have been suggested to overcome this problem: Bethe-Brueckner-Goldstone expansion [Ba99], correlated basis functions [Fe69] [FF98], quantum Monte Carlo [WP+00], self-consistent Green's function theory [DM92], [DV05]. These methods

were successfully applied to describe bulk properties of the homogeneous nuclear matter [GV$^+$09], pairing gap of nucleons [FF$^+$08], weak response [Fa08] and shear viscosity of nuclear matter [BC09]. However, these approaches are too complex to be applied directly to the description of the pasta phase.

An alternative method, which preserves the accuracy of the realistic NN interactions and allows to implement the Hartree-Fock technique similarly to the phenomenological forces is the low-momentum interaction $V_{\text{low-k}}$. The basic idea of $V_{\text{low-k}}$ is to separate the predictions for correlations at low momenta, constrained by the NN scattering matrix below the pion threshold, from the high-momentum components, which may strongly depend on the underlying model of the realistic NN interaction. By introducing a cutoff Λ in momentum space, one separates the Hilbert space into a low-momentum and a high-momentum part. The renormalization technique (see, e.g., [BK$^+$01], [LS80], [O54], [S82]) determines an effective Hamiltonian, which must be diagonalized within the model space (below the cutoff). With the cutoff in the range of $\Lambda = 2 \text{ fm}^{-1}$ $V_{\text{low-k}}$ becomes model independent, and reproduces the deuteron binding energy, low-energy phase shifts, and half-on-shell T matrix with the same accuracy as the initial realistic interaction. Therefore $V_{\text{low-k}}$ is also referred to as *realistic* low-momentum nucleon-nucleon interaction. The absence of the short-range core allows to employ $V_{\text{low-k}}$ in Hartree-Fock calculations. In this connection the low-momentum potential is considered as a solid starting point to produce a new set of nuclear equations of state, including the inhomogeneous structure of the crust.

In spite of its obvious advantages $V_{\text{low-k}}$ potential still remains quite a complicate object. On the one hand, being nonlocal, it is represented in terms of matrix elements in momentum space for each partial wave channel. This nonlocality increases the computational time in Hartree-Fock iterations, and prevents using $V_{\text{low-k}}$ if the number of nucleons is too large. On the other hand, the renormalization technique used to produce $V_{\text{low-k}}$ seems to be not that trivial. The resulting interaction is given as a matrix table which is not an easy-to-use form and prevents this potential to be popular in nuclear structure calculations. A possible way out is to find a separable representation of $V_{\text{low-k}}$, since it significantly simplifies the many-body calculation [BF88], [TMR09]. Moreover recent calculations of triton binding energies demonstrate that the $V_{\text{low-k}}$ can be very good approximated by a low-rank separable force for low values of the cutoff Λ [KF$^+$06]. In this Thesis the separability of $V_{\text{low-k}}$ is

investigated by using the diagonalization of the matrix in momentum space for each partial wave channel. This allows finding a low rank separable form of $V_{\text{low-k}}$, which can be used in the Hartree-Fock calculations of nuclear matter as well as finite nuclei. The resulted low-momentum separable interaction can be parameterized by a simple algebraic function [GV$^+$10]. This provides a particularly suitable framework for calculations with the realistic low-momentum interaction omitting the robust numerical technique producing it.

The present Thesis is organized as follows:

In Chapter 2 the general Hartree-Fock formalism is briefly outlined. After that it is applied to the density-dependent Skyrme force. The set of the Skyrme Hartree-Fock equations is outlined for the general case. Later it will be solved both for the spherical and cubic Wigner-Seitz cells.

Below the critical temperature $T_c \sim 1$ MeV all neutrons in the crust undergo a phase transition to the superfluid state. Therefore the pairing correlations are included in the Hartree-Fock code by means of the BCS approach. The details are reviewed at the beginning of Chapter 3. After that the finite temperature BCS limit of the general Bogoliubov theory is derived for a monopole pairing force. This provides the solution of the Hartree-Fock equations at finite temperatures.

The pasta objects resulted from the Skyrme Hartree-Fock calculations with cubic and spherical WS cells are displayed in Chapter 4. Varying the temperature in the HF code the stability of the pasta objects is investigated. Assuming the spherical symmetry, the single-particle structure of the droplet-phase is revealed and compared to the structure of the homogeneous nuclear matter at the same average density. Later on the dynamical response function $S(q, \omega)$ is calculated, and its connection with the microscopical structure is considered.

In the next Chapter 5 the single-particle wave functions and energies resulting from the Skyrme Hartree-Fock calculations within the cubic cell are used for computing of the neutrino mean free path. The nuclear matter in β-equilibrium contains three quasi nuclear structures: droplet, rod and slab. The scattering of neutrino on these pasta objects is discussed. Both the charged and neutral current contributions to the mean free path are considered in details. The comparison between the homogeneous and inhomogeneous nuclear matter is used to reveal the influence of the pasta phase on the neutrino opacity. The model dependence of the results is tested by performing

similar calculations for a relativistic mean-field model.

The main advantages of the low-momentum nucleon-nucleon interaction $V_{\text{low-k}}$ are discussed in Chapter 6. Thereafter both the renormalization group and unitary transformation method to produce $V_{\text{low-k}}$ from a bare realistic interaction are considered. The resulting low-momentum potential is used in the Hartree-Fock approximation to derive the bulk properties of nuclear matter. Later the bulk properties as well as the single-particle structure of various nuclei are discussed. The second part of this Chapter is dedicated to the construction of the separable version of $V_{\text{low-k}}$ interaction. The separability is investigated for various partial wave channels of a low-rank separable form of $V_{\text{low-k}}$, called $V_{\text{low-k}}^{[2,3]}$. It assumes the second rank approximation for the uncoupled channels and the third rank approximation for the coupled ones. The accuracy of $V_{\text{low-k}}^{[2,3]}$ is tested in the Hartree-Fock calculations of finite nuclei and nuclear matter. Finally a simple parameterization of this separable form is given.

The last Chapter 7 summarizes the main results of the Thesis and gives an outlook for future investigations.

Chapter 2

The Skyrme Hartree-Fock Approach

In this chapter we consider the Hartree-Fock method, which is an approximate method for the determination of the ground-state wave function and the ground state energy of a quantum many-body system. After the introduction to the general Hartree-Fock formalism we turn to the density-dependent Skyrme force. Later the Hartee–Fock method is applied to the Skyrme energy functional to derive the set of the Skyrme Hartree-Fock equations.

2.1   The General Hartree-Fock Formalism

To solve the nuclear many-body problem we start from a system of A interacting nucleons, which can be characterized by the Hamiltonian

$$H = \sum_{i=1}^{A} T_i + \sum_{i<j}^{A} V_{ij}, \tag{2.1}$$

where T_i stands for the kinetic energy operator of i-th nucleon, V_{ij} is the interaction between i-th and j-th particles. The Schrödinger equation for this system described by the many-body wave function $|\Phi(1 \ldots A)\rangle$ looks like

$$H|\Phi(1 \ldots A)\rangle = E|\Phi(1 \ldots A)\rangle \tag{2.2}$$

and can be simplified within the independent particle model, in which the main assumption is that all nucleons move independently in an average potential pro-

duced by all of the nucleons independently. Thus the two-body potential V_{ij} can be approximated by the single-particle potential

$$\sum_{i<j}^{A} V_{ij} \simeq \sum_{i}^{A} V_i \tag{2.3}$$

and the Hamiltonian (2.1) can be split and written as a sum over kinetic T_i and potential V_i energy for each nucleon. In this case the many-body wave function $|\Phi(1\ldots A)\rangle$ can be factorized and written as the multiplication of the single-particle wave functions $|\varphi_i\rangle$

$$|\Phi(1\ldots A)\rangle = \{|\varphi_1\rangle|\varphi_2\rangle\ldots|\varphi_A\rangle\}_A = \prod_{i=1}^{A} a_i^{\dagger}|0\rangle, \tag{2.4}$$

where the Fermion operator $a_i^{\dagger}$ creates a particle in φ_i state from the vacuum $|0\rangle$. Such a wave function (2.4) being antisymmetric due to a permutation between two nucleons to obey the Pauli principle is usually referred to as Slater determinant.

Now we define the Hartree-Fock method in the following way. We use the set of Slater determinants consisting of A arbitrary but orthogonal single-particle wave functions φ_i[1] as trial wave functions and minimize the energy within this set. Before this minimization we have to calculate the HF-energy with many-body Hamiltonian (2.1)

$$E^{HF} = \langle\Phi|H|\Phi\rangle. \tag{2.5}$$

On applying the second quantization formalism (also known as the Fock space) with basis operators $c_{\alpha}^{\dagger}, c_{\alpha}$ the Hamiltonian has the form

$$H = \sum_{i,j}^{A} \langle i|T|j\rangle c_i^{\dagger} c_j + \frac{1}{4} \sum_{i,j,k,l}^{A} \langle ij|V|\widetilde{kl}\rangle c_i^{\dagger} c_j^{\dagger} c_l c_k, \tag{2.6}$$

where $c_{\alpha}^{\dagger}, c_{\alpha}$, generally speaking, differ from the operators $a_{\alpha}^{\dagger}, a_{\alpha}$ (2.4) and due to the permutation asymmetry

$$\langle ij|V|\widetilde{kl}\rangle = \langle ij|V|kl\rangle - \langle ij|V|lk\rangle. \tag{2.7}$$

---

[1]Usually the harmonic oscillator or the plane wave basis is used to expend φ_i.

In virtue of the Wick's theorem one can express the HF-energy (2.5) through the single-particle density ρ

$$
\begin{aligned}
E^{HF}[\rho] &= \sum_{i,j}^{A} \langle i|T|j\rangle \langle\Phi|c_i^\dagger c_j|\Phi\rangle + \frac{1}{4}\sum_{i,j,k,l}^{A} \langle ij|V|\widetilde{kl}\rangle \langle\Phi|c_i^\dagger c_j^\dagger c_l c_k|\Phi\rangle \\
&= \sum_{i,j}^{A} \langle i|T|j\rangle\, \rho_{ji} + \frac{1}{2}\sum_{i,j,k,l}^{A} \rho_{ki}\langle ij|V|\widetilde{kl}\rangle\rho_{lj}.
\end{aligned}
\tag{2.8}
$$

Since the last expression does not depend on the basis we can assume that the HF-basis as a basis in which the density matrix ρ is diagonal with the eigenvalues 0 and 1. In this case the HF-energy looks like

$$
E^{HF} = \sum_{i}^{A} \langle i|T|i\rangle + \frac{1}{2}\sum_{i,j}^{A} \langle ij|V|\widetilde{ij}\rangle.
\tag{2.9}
$$

To determine the HF-basis, the energy E^{HF} has to be minimized with respect to all product wave functions $|\Phi\rangle$. The variation of the energy (2.8) is written

$$
\delta E = E[\rho + \delta\rho] - E[\rho] = \sum_{ij} H_{ij}^{HF}\delta\rho_{ij} = 0,
\tag{2.10}
$$

where the matrix H^{HF} is the hermitian matrix of the single-particle Hamiltonian

$$
H_{ij}^{HF} = \frac{\partial E^{HF}[\rho]}{\partial\rho_{ij}}.
\tag{2.11}
$$

Applying this derivative to (2.8) we obtain

$$
H_{ij}^{HF} = T_{ij} + \Gamma_{ij},
\tag{2.12}
$$

where Γ is a self-consistent one-body field, which depends on the density. Averaging over all two-body interactions one gets

$$
\Gamma_{ij} = \sum_{kl} \langle ik|V|\widetilde{jl}\rangle\rho_{lk}.
\tag{2.13}
$$

The variation (2.10) is possible for particle-hole (ph) configurations. In this case $\delta\rho_{ij}$ does not vanish and it requires that the ph matrix elements of H^{HF} have to vanish

$$
H_{ij}^{HF} = T_{ij} + \sum_{m} \langle mj|V|\widetilde{ij}\rangle = 0 \qquad (i \le A, j > A).
\tag{2.14}
$$

The last statement means that H^{HF} does not mix particle and hole states of density matrix ρ and therefore both matrix H^{HF} and ρ can be diagonalized simultaneously

$$[H^{HF}, \rho] = 0. \tag{2.15}$$

This defines the eigenvalue problem

$$H_{ij}^{HF} = T_{ij} + \sum_k \langle ik|V|\widetilde{jk}\rangle = \varepsilon_i \delta_{ij}, \tag{2.16}$$

from which we obtain the single-particle states $|\varphi_i\rangle$ and the single-particle energies ε_i. This eigenvalue problem (2.16) can be solved iteratively. First, one starts from the initial wave functions (e.g., the harmonic oscillator basis) and calculates the Hermitian matrix H_{ij}^{HF}, which is later diagonalized to get the single-particle energy spectrum and a new set of wave functions. After that this procedure should be repeated until the convergence is achieved, that is, the potential stays constant in two consecutive steps. After the single-particle basis set is defined one can obtain the energy of the ground state

$$E^{HF} = \langle\Phi|H|\Phi\rangle = \sum_i \varepsilon_i - \frac{1}{2}\sum_{ij}\langle ij|V|\widetilde{ij}\rangle, \tag{2.17}$$

where the total energy of the system is not equal to $\sum_{i=1}^{A}\varepsilon_i$, but differs on the half of interaction energy. Due to the Koopman's theorem the HF single-particle energy ε_i can be considered as the energy needed to remove the nucleon from i-th state.

Before we start the consideration of the density-dependent Skyrme interaction let us briefly discuss some important features of the HF theory. The HF method conserves the so-called self-consistent symmetries. This means that if the initial single-particle wave functions have a certain spatial symmetry and if this symmetry is not violated by the occupation of states, after the HF iteration the resulting wave functions will also have the same symmetry. Therefore, if we expect a symmetry for the solution, we can start with the initial single-particle wave functions, which possess this symmetry to enhance the convergence of each iteration. For example, if we consider the spherically symmetric nuclei a choice of the initial basis can be done among the spherically symmetric orthogonal functions. However, if the absolute minimum in (2.10) corresponds to the deformed Slater determinants, we will never reach it starting with the spherically symmetric wave functions.

Having the ground state defined we have to face other difficulties. The initial Hamiltonian (2.1) is usually translationally invariant, but the choice of initial basis as a combination of Slater determinants violates this symmetry. In other words, the mean field localizes the nucleus and thus breaks translational invariance. There are different methods to cure this lack. The center-of-mass corrections to the total energy can be made, e.g., by subtracting the center-of-mass kinetic energy from the many-body Hamiltonian. This correction is proportional to $\frac{1}{A}$ and therefore is very important for light nuclei. However this method is usually applied *after variation* and therefore has influence only on the total energy of the system. The resulting wave function remains, however, the same. A rigorous restoration of the translational invariance *before variation* is possible with the help of the projection techniques [SG90], [SR91], [Sc01].

The Hartree-Fock method fails in direct application to the bare NN interactions due to the strong short-range components, which are necessary to describe the NN data [MP00]. In case of the hard-core potentials like Hamada-Johnston [HJ62], which describe these short-range components in terms of an infinitely repulsive core, the Hartree-Fock calculations yield an infinite repulsive energy. The modern meson-exchange realistic models of NN interaction contain softer cores, however, in the Hartree-Fock approximation they lead to unbound nuclei [MuP00]. Different approaches have been developed to account for such correlations: Brueckner hole-line expansion [Br54], [Ba99], the coupled cluster approach [KLZ78], the self-consistent Greens functions method [DM92], correlated basis functions technique [Fe69], [FF98] and quantum Monte-Carlo theory [SC91], [WP+00]. In Chapter 6 of this Thesis we deal with the strong short-range components by using the low-momentum effective NN interaction constructed from the bare NN force and apply the resulted potential for calculations of the properties of finite nuclei and nuclear matter.

2.2 The Density-Dependent Skyrme Force

Since the density of heavy nuclei is rather a constant inside the nucleus, one can replace the density dependence of the G-matrix by dependence on the local density ρ. In such Local Density Approximation (LDA) the G-matrix inside the nucleus coincides with the G-matrix of nuclear matter at the same local density. The effective

density-dependent force constructed in this approximation may solve the hard core problem in the Hartree-Fock theory and lead to a consistent re-summation of higher order terms of the full many-body problem. The solution of the integrodifferential HF equations with the effective interaction derived from the self-consistent G-matrix still remains a very complicated problem. As an alternative approach one can replace the density-dependent effective interaction by a density-dependent phenomenological force. This idea was used to construct the Skyrme-like effective interaction which was found to be a very successful tool in the many-body calculations of finite nuclei and nuclear matter. In early 1950s Skyrme proposed a phenomenological velocity-dependent nuclear force, which is now called the conventional Skyrme force [Sk59]. This phenomenological interaction is of zero range and therefore it is easy to use in practical calculations. Later Vautherin and Brink [VB72] simplified the two-body interaction and determined two sets of the conventional Skyrme force parameters (the so-called SI and SIII) by fitting the experimental binding energies, nucleon densities and root-mean-radii of finite nuclei over the whole periodic table. At the same time Negele and Vautherin [NV72] explored the connection between Skyrme force and the Brückner G-matrix. Recently Chabanat *et al.* [CB$^+$97] constructed a new version of the Skyrme potential, which is constrained to obtain results for neutron-rich nuclear matter comparable to those of the microscopical calculations. The Skyrme force consists of the two-body and the three-body terms

$$V^{Sk} = \sum_{i<j} V^{(2)}(i,j) + \sum_{i<j<k} V^{(3)}(i,j,k). \tag{2.18}$$

Following the *standard* analytical form one can write the two-body part as [CB$^+$97]

$$\begin{aligned}
V^{(2)}(\boldsymbol{r}_1, \boldsymbol{r}_2) =\ & t_0(1 + x_0 P_\sigma)\delta(\boldsymbol{r}) \\
& + \frac{1}{2}t_1(1 + x_1 P_\sigma)\left[\boldsymbol{p'}^2\delta(\boldsymbol{r}) + \delta(\boldsymbol{r})\boldsymbol{p}^2\right] \\
& + t_2(1 + x_2 P_\sigma)\boldsymbol{p'} \cdot \delta(\boldsymbol{r})\boldsymbol{p} \\
& + iW_0\boldsymbol{\sigma} \cdot \left[\boldsymbol{p'} \times \delta(\boldsymbol{r})\boldsymbol{p}\right],
\end{aligned} \tag{2.19}$$

which contains a central term with the parameter t_0 and x_0, an effective range terms depending on the parameters t_1, x_1, t_2, x_2, and the spin-orbit term with the spin-orbit strength parameter W_0. The three-body potential was originally written as

$$V^{(3)}(\boldsymbol{r}_1, \boldsymbol{r}_2, \boldsymbol{r}_3) =\ t_3\delta(\boldsymbol{r}_1 - \boldsymbol{r}_2)\delta(\boldsymbol{r}_2 - \boldsymbol{r}_3). \tag{2.20}$$

Here we introduce the relative coordinate $\boldsymbol{r} = \boldsymbol{r}_1 - \boldsymbol{r}_2$, the center-of-mass coordinate of two particles $\boldsymbol{R} = \frac{1}{2}(\boldsymbol{r}_1 + \boldsymbol{r}_2)$, the relative momentum $\boldsymbol{p} = \frac{1}{2i}(\boldsymbol{\nabla}_1 - \boldsymbol{\nabla}_2)$ with its complex conjugate counterpart acting on the bra-state with momentum $\boldsymbol{p}'$, the two-body spin operator $\boldsymbol{\sigma} = \boldsymbol{\sigma}_1 + \boldsymbol{\sigma}_2$, and the spin exchange operator $P_\sigma = (1 + \boldsymbol{\sigma}_1 \cdot \boldsymbol{\sigma}_2)/2$. The three-body term is often modified to include the density dependence of σ-power

$$V^{(3')}(\boldsymbol{r}_1, \boldsymbol{r}_2) = \frac{1}{6}t_3(1 + x_3 P_\sigma)[\rho(\boldsymbol{R})]^\sigma \delta(\boldsymbol{r}). \tag{2.21}$$

For $\sigma = 1$ one recovers the original three-body interaction in equation (2.20). Except the *standard* form there were suggested some additional *non-standard* parameterizations, however, as it was shown by Negele and Vautherin [NV72], they often give collapses in the equation of state of the symmetric infinite nuclear matter.

2.3   The Skyrme Energy Functional

The derivation of the Skyrme energy functional is based mainly on the Density Functional Theory (DFT) which was developed to describe electronic systems [PS91], [DG95]. Within this theory the quantum many-body problem described in terms of the many-body wave functions $\Psi(\boldsymbol{r_1}, \boldsymbol{r_2}, \ldots, \boldsymbol{r_N})$ or, in other words, in terms of the many-body density matrices $\rho(\boldsymbol{r_1}, \ldots, \boldsymbol{r_N}; \boldsymbol{r'_1}, \ldots, \boldsymbol{r'_N})$, can be reduced to involve only one-particle density $\rho(\boldsymbol{r})$. Such reformulation of the many-body problem in terms of the density $\rho(\boldsymbol{r})$ instead of the wave function is based on the *Hohenberg-Kohn Theorem* [HK64]. In virtue of this theorem the ground state energy of a system of spinless fermions is uniquely determined by the functional of the local fermionic density $E[\rho]$. When the density of such system coincides with its correct ground-state value, the functional $E[\rho]$ achieves its minimum value. That is the ground state energy of the system. Later the *Hohenberg-Kohn Theorem* was extended to take into account the finite temperatures [Me65] and spin of fermions (see, e.g., [PR72]).

In accordance with DFT, the local one-body density $\rho(r)$ contains enough information to determine the ground state of the system, if the exact functional $E[\rho]$ is known. However the derivation of the exact functional $E[\rho]$ is equivalent to the exact solution of the many-body problem. In this case DFT is forced to adopt some approximations to the exact functional $E[\rho]$ which are easy to handle in practice. At the same time these approximations should reflect some important features of its

nontrivial structure. In this sense the Skyrme-type interaction is a good ansatz to refine the approximate ground-state energy-density functional.

The energy functional of Skyrme interaction depends not only on the nucleon density $\rho(r)$, but also on the kinetic energy density $\tau(r)$ and spin-orbit density $J(r)$. The two latter quantities can be expressed in terms of the single-particle wave functions. An advantage of the Skyrme interaction consists in a simple derivation of the Hartree-Fock equations, which are now differential equations. The total energy of a system is the expectation value of the corresponding Hamiltonian with respect to a Slater determinant $|\Phi\rangle$

$$E = \langle\Phi|H|\Phi\rangle, \tag{2.22}$$

where $|\Phi\rangle$ consists of the single-particle wave functions $\varphi_\alpha^q(\boldsymbol{r}, s)$ with the orbital, spin and isospin quantum numbers α, s, and q, respectively. The occupation factors η_α^q are determined by the Fermi energy $\varepsilon_{F,q}$ and the desired scheme of occupation described in Chapter 3. By using (2.1) and (2.18) one can rewrite the energy E as

$$
\begin{aligned}
E &= \langle\Phi|T + V^{(2)} + V^{(3)}|\Phi\rangle & (2.23)\\
&= \sum_i \langle i|\frac{p_i^2}{2m}|i\rangle + \sum_{i<j}\langle ij|V^{(2)}|\widetilde{ij}\rangle & (2.24)\\
&+ \frac{1}{3}\sum_{i<j<k}\langle ijk|V^{(3)}|\widetilde{ijk}\rangle, & (2.25)
\end{aligned}
$$

where T is the kinetic energy operator, $V^{(2)}$ is the two-body part, and $V^{(3)}$ is the three-body part of the Skyrme interaction. Because of zero range character of the Skyrme force, it is possible to express E by an integral over an energy density

$$E = \int \mathcal{H}(\boldsymbol{r})d^3r. \tag{2.26}$$

The quantity $\mathcal{H}(\boldsymbol{r})$ depends on various densities which are:

i) the nucleon density

$$\rho_q(\boldsymbol{r}) = \sum_{\alpha,s} \eta_\alpha^q \, |\varphi_\alpha^q(\boldsymbol{r}, s)|^2, \tag{2.27}$$

ii) the kinetic energy density

$$\tau_q(\boldsymbol{r}) = \sum_{\alpha,s} \eta_\alpha^q \, |\boldsymbol{\nabla}\varphi_\alpha^q(\boldsymbol{r}, s)|^2, \tag{2.28}$$

iii) the spin-orbit density

$$\boldsymbol{J}_q(\boldsymbol{r}) = -i \sum_{\alpha,s,s'} \eta_\alpha^q \, (\varphi_\alpha^q)^*(\boldsymbol{r}, s') \boldsymbol{\nabla} \varphi_\alpha^q(\boldsymbol{r}, s) \times \langle s'|\boldsymbol{\sigma}|s\rangle. \tag{2.29}$$

The gradient of the spin-orbit density $\boldsymbol{\nabla} \boldsymbol{J} = \boldsymbol{\nabla} \boldsymbol{J}_p + \boldsymbol{\nabla} \boldsymbol{J}_n$ can be directly evaluated without first calculating $\boldsymbol{J}$:

$$\boldsymbol{\nabla} \boldsymbol{J}_q(\boldsymbol{r}) = -i \sum_{\alpha,s,s'} \eta_\alpha^q \, \boldsymbol{\nabla}(\varphi_\alpha^q)^*(\boldsymbol{r}, s') \times \boldsymbol{\nabla} \varphi_\alpha^q(\boldsymbol{r}, s) \cdot \langle s'|\boldsymbol{\sigma}|s\rangle. \tag{2.30}$$

A lengthy but straightforward calculation [VB72] gives the Hamiltonian density $\mathcal{H}$

$$\mathcal{H} = \mathcal{H}_K + \mathcal{H}_0 + \mathcal{H}_3 + \mathcal{H}_{\text{eff}} + \mathcal{H}_{\text{fin}} + \mathcal{H}_{\text{so}} + \mathcal{H}_{\text{sg}} + \mathcal{H}_{\text{Coul}}, \tag{2.31}$$

where $\mathcal{H}_K$ is the kinetic energy term, $\mathcal{H}_0$ a zero range term, $\mathcal{H}_3$ a density dependent term, $\mathcal{H}_{\text{eff}}$ an effective mass term, $\mathcal{H}_{\text{fin}}$ a finite range term, $\mathcal{H}_{\text{so}}$ a spin–orbit term, and $\mathcal{H}_{\text{sg}}$ a term due to the tensor coupling with spin and gradient. Here are the explicit formulas for the parts of this functional:

$$
\begin{aligned}
\mathcal{H}_K &= \frac{\hbar^2}{2m}\tau, \\
\mathcal{H}_0 &= \tfrac{1}{4}t_0\big[(2 + x_0)\rho^2 - (2x_0 + 1)(\rho_p^2 + \rho_n^2)\big], \\
\mathcal{H}_3 &= \tfrac{1}{24}t_3\rho^\alpha\big[(2 + x_3)\rho^2 - (2x_3 + 1)(\rho_p^2 + \rho_n^2)\big], \\
\mathcal{H}_{\text{eff}} &= \tfrac{1}{8}\big[t_1(2 + x_1) + t_2(2 + x_2)\big]\tau\rho \\
&\quad + \tfrac{1}{8}\big[t_2(2x_2 + 1) - t_1(2x_1 + 1)\big]\big[\tau_p\rho_p + \tau_n\rho_n\big], \\
\mathcal{H}_{\text{fin}} &= -\tfrac{1}{32}\big[3t_1(2 + x_1) - t_2(2 + x_2)\big]\rho\Delta\rho \\
&\quad + \tfrac{1}{32}\big[3t_1(2x_1 + 1) + t_2(2x_2 + 1)\big]\big[\rho_p\Delta\rho_p + \rho_n\Delta\rho_n\big], \\
\mathcal{H}_{\text{so}} &= -\tfrac{1}{2}W_0\big[\rho\,\boldsymbol{\nabla}\boldsymbol{J} + \rho_p\,\boldsymbol{\nabla}\boldsymbol{J}_p + \rho_n\,\boldsymbol{\nabla}\boldsymbol{J}_n\big]. \\
\mathcal{H}_{\text{sg}} &= -\tfrac{1}{16}(t_1x_1 + t_2x_2)\boldsymbol{J}^2 + \tfrac{1}{16}(t_1 - t_2)\big[\boldsymbol{J}_p^2 + \boldsymbol{J}_n^2\big]
\end{aligned}
\tag{2.32}
$$

The coefficients t_i, x_i, W_0, and α are the parameters of the Skyrme interaction from Section 2.2 and m is the nucleon mass. Here we used the usual notations for the total density $\rho = \rho_n + \rho_p$, $\tau = \tau_n + \tau_p$, and $\boldsymbol{J} = \boldsymbol{J}_n + \boldsymbol{J}_p$.

Usually the time-odd part of interaction is omitted since the time-reversal invariance in such calculations is assumed. If this symmetry is broken, e.g., for rotating states, the density matrix and the resulting mean field have both time-even and time-odd components.

The energy density of equation (2.31) contains the contribution of the Coulomb force, $\mathcal{H}_{\text{Coul}}$, which is calculated from the charge density ρ_C as

$$\mathcal{H}_{\text{Coul}}(\boldsymbol{r}) = \frac{e^2}{2}\rho_C(\boldsymbol{r})\int d^3r'\,\frac{\rho_C(\boldsymbol{r}')}{|\boldsymbol{r}-\boldsymbol{r}'|} \ - \frac{3e^2}{4}\left(\frac{3}{\pi}\right)^{1/3}\rho_C^{4/3}. \tag{2.33}$$

Here the exchange part of the Coulomb term is calculated within the Slater approximation. Following Bonche *et al.* [BF+85] the charge density is replaced by the proton density ρ_p and, whenever electrons are present, the electron density ρ_e is to be subtracted

$$\rho_C(\boldsymbol{r}) = \rho_p(\boldsymbol{r}) - \rho_e(\boldsymbol{r}). \tag{2.34}$$

In Hartree-Fock method the center-of-mass motion generates spurious states and their contribution E_{cm} to the total energy must be extracted

$$E_{cm} = \frac{\boldsymbol{P}}{2mA} = \frac{(\sum_i \boldsymbol{p}_i)^2}{2mA} = \frac{1}{2mA}\left[\sum_i \boldsymbol{p}_i^2 + \sum_{i\neq j}\boldsymbol{p}_i\boldsymbol{p}_j\right]. \tag{2.35}$$

Usually one neglects the contribution of the second two-body term in (2.35), since it is difficult to calculate. In fact, its direct part vanishes, and only the exchange part gives non-zero contribution. In our calculations both terms of (2.35) are computed *after variation*, since the double sum over single-particle states may increase the calculation time for each HF-iteration. Therefore this correction does not contribute to the Hartree-Fock equations.

The calculation of asymmetric homogeneous nuclear matter can be directly performed from the energy functional (2.26), in which the kinetic energy density is obtained from

$$\tau_q = 2\int \frac{d^3p}{(2\pi)^3}p^2\eta_q(p) \tag{2.36}$$

or in the Hartree-Fock occupation

$$\tau_q = \frac{(3\pi^2\rho_q)^{5/3}}{5\pi^2}, \tag{2.37}$$

which demonstrates the explicit density dependence [RS80]. The spin-orbit term in asymmetric nuclear matter does not contribute to the energy and the Coulomb interaction is neglected because of the charge neutrality of nuclear matter. The baryon energy density is then $\mathcal{E} = \mathcal{H}$ and the baryon energy per nucleon becomes $E/A = \mathcal{E}/\rho$. Further the chemical potential is obtained by

$$\mu_q = \frac{p_{F,q}^2}{2m_q^*} + U_q(p_{F,q}), \tag{2.38}$$

where m_q^* is the effective mass and U_q the single-particle potential, which are both specified in the next Section. It is worth mentioning that the potential depends on the density and the kinetic energy density, which are both determined by the Fermi momentum $p_{F,q}$.

2.4 The Skyrme Hartree-Fock Equations

In accordance with the density functional theory we have to vary the energy functional (2.26) with respect to the density $\rho(\boldsymbol{r})$ to get the set of Hartree-Fock equations. However it is not possible since the kinetic energy density $\tau(\boldsymbol{r})$ and the spin-orbit energy density $\boldsymbol{J}(r)$ do not depend on $\rho(\boldsymbol{r})$ explicitly. This problem may be solved if we recall that the local density $\rho(\boldsymbol{r})$ determines completely the ground state, viz., the HF-density $\rho(\boldsymbol{r})$ uniquely defines the single particle wave function $\varphi_\alpha^q(\boldsymbol{r}, s)$. It allows us to replace the variation with respect to $\rho(\boldsymbol{r})$ by the variation with respect to $\varphi_\alpha^q(\boldsymbol{r}, s)$ with the constraint that the single particle wave functions are orthonormal. Thus we end up with the following variation

$$\frac{\delta}{\delta \varphi_\alpha^*} \left\{ E[\Phi] - \sum_{\alpha,s,q} \varepsilon_\alpha^q \left(\int d^3 r \, |\varphi_\alpha^q(\boldsymbol{r}, s)|^2 - 1 \right) \right\} = 0, \qquad (2.39)$$

where the single-particle energies are the Lagrange multipliers. The energy functional in the last formula can be used from (2.26). After the partial integration one obtains the set of the Hartree-Fock equations for Skyrme interaction [RS80]

$$\left\{ -\boldsymbol{\nabla} \frac{\hbar^2}{2m_q^*(\boldsymbol{r})} \boldsymbol{\nabla} + U_q(\boldsymbol{r}) - i \, \boldsymbol{W}_q(\boldsymbol{r}) \cdot (\boldsymbol{\nabla} \times \boldsymbol{\sigma}) \right\} \varphi_\alpha^q(\boldsymbol{r}, s) = \varepsilon_\alpha^q \, \varphi_\alpha^q(\boldsymbol{r}, s). \qquad (2.40)$$

The effective mass m^* depends on $\mathcal{H}_{\text{eff}}$ of the energy functional (2.26)

$$\frac{\hbar^2}{2m_q^*(\boldsymbol{r})} = \frac{\hbar^2}{2m} + \tfrac{1}{8}[t_1(2 + x_1) + t_2(2 + x_2)] \, \rho(\boldsymbol{r})$$
$$+ \tfrac{1}{8}[t_2(1 + 2x_2) - t_1(1 + 2x_1)] \, \rho_q(\boldsymbol{r}), \qquad (2.41)$$

a central potential

$$
\begin{aligned}
U_q(\boldsymbol{r}) = {}& \tfrac{1}{2}t_0\big[(2+x_0)\rho - (1+2x_0)\rho_q\big] \\
& + \tfrac{1}{24}t_3(2+x_3)(2+\alpha)\rho^{\alpha+1} \\
& - \tfrac{1}{24}t_3(2x_3+1)\big[2\rho^\alpha\rho_q + \alpha\rho^{\alpha-1}\big(\rho_p^2+\rho_n^2\big)\big] \\
& + \tfrac{1}{8}\big[t_1(2+x_1)+t_2(2+x_2)\big]\tau \\
& + \tfrac{1}{8}\big[t_2(2x_2+1)-t_1(2x_1+1)\big]\tau_q \\
& + \tfrac{1}{16}\big[t_2(2+x_2)-3t_1(2+x_1)\big]\Delta\rho \\
& + \tfrac{1}{16}\big[3t_1(2x_1+1)+t2(2x_2+1)\big]\Delta\rho_q \\
& - \tfrac{1}{2}W_0\big[\boldsymbol{\nabla}\boldsymbol{J}+\boldsymbol{\nabla}\boldsymbol{J}_q\big] \\
& + \delta_{q,p}\,V_{\text{Coul}}
\end{aligned}
\tag{2.42}
$$

with the Coulomb field

$$
V_{\text{Coul}}(\boldsymbol{r}) = e^2\int d^3r'\,\frac{\rho_C(\boldsymbol{r}')}{|\boldsymbol{r}-\boldsymbol{r}'|} - e^2\left(\frac{3}{\pi}\right)^{1/3}\rho_C^{1/3},
\tag{2.43}
$$

and a spin–orbit field:

$$
\begin{aligned}
\boldsymbol{W}_q(\boldsymbol{r}) = {}& \tfrac{1}{2}W_0\left(\boldsymbol{\nabla}\rho+\boldsymbol{\nabla}\rho_q\right) \\
& - \tfrac{1}{8}(t_1x_1+t_2x_2)\boldsymbol{J}+\tfrac{1}{8}(t_1-t_2)\boldsymbol{J}_q.
\end{aligned}
\tag{2.44}
$$

The binding energy E^{HF} can be calculated from the energy functional

$$
E_{HF} = \tfrac{1}{2}\left(\sum_{\alpha,\,q} t_\alpha^q + \varepsilon_\alpha^q\right) + E_r,
\tag{2.45}
$$

where the last term E_r is the rearrangement energy (also known as the saturation potential [RS80]) and it appears due to the density dependence of the underlying interaction [PGR91]. The rearrangement term plays an important role in simultaneous description of the binding energy and charge radii of finite nuclei over the whole periodic table. The rearrangement energy can be calculated after

$$
\begin{aligned}
E_r = {}& -\int d^3r\,\tfrac{\alpha}{48}t_3\rho^\alpha\big[(2+x_3)\rho^2-(1+2x_3)(\rho_p^2+\rho_n^2)\big] \\
& + \frac{1}{4}\left(\frac{3}{\pi}\right)^{1/3}\int d^3r\,\rho_p^{4/3},
\end{aligned}
\tag{2.46}
$$

where the Coulomb exchange part was also included as the second term.

All equations considered so far are written in the form which allows the HF calculations within the cubic WS cell. If the spherical symmetry is considered, all equations can be simplified. The general scheme of the solution of HF equations in this case is described in details by Reinhard [PGR91]. Going beyond the region of stable nuclei one can consider exotic nuclear structures, like the pasta phase, when the occupation scheme cannot be determined experimentally, and therefore cannot be used as a known input in the HF calculations. In this case, the occupation scheme is determined by varying the chemical potential of nucleons with a constraint on the desired particle number. It involves also the calculation of the pairing gap, if the pairing phenomenon is taken into account. In the next Chapter we consider the pairing of nucleons within the BCS approximation.

Chapter 3

Pairing of Nucleons

It is known from the standard theory of superconductivity [BCS57] that two nucleons on the same shell may form a pair – the energetically favourable state with the total zero angular momentum. The *pairing* is a collective effect, since it becomes possible in a field of other nucleons and cannot exist between two nucleons in vacuum. Therefore a many-body nuclear system may undergo a phase transition to a superfluid state. The pairing of nucleons is described in terms of the short-range residual interaction, since the preferable state of two nucleons has the zero total angular momentum and they remain very close to one other.

The superfluid model of finite nuclei describes many features which cannot be explained within the framework of the shell model, such as the mass difference of odd and even nuclei, the density of one-particle states, the moments of inertia of deformed nuclei and many others [RS80]. In early 1960's Migdal pointed out that the interacting nucleons in the highly compressed matter inside the neutron stars may become superfluid [Mi60]. The modern theory of NS considers three different regions, where the hadron superfluidity may exist: in the inner crust, at relatively low densities $10^{-3}\rho_0 \leq \rho \leq 0.7\rho_0$ neutrons form $^1S_0$ pairs, since $^1S_0$ partial wave channel of NN interaction is attractive; in the core at $\rho \geq 0.7\rho_0$ $^1S_0$ channel becomes repulsive and neutrons form $^3P_2$ pairs. The proton pairs exist in $^1S_0$ state, since their fraction is smaller than the neutron fraction. At baryonic density higher than $0.7\rho_0$ various hyperons may exist and form pairs in the same way as nucleons. Due to a significant difference in Fermi surfaces of protons and neutrons one usually neglects the proton-neutron pairing.

Since the pairing energy amounts to only about 1% of the total interaction energy, the hadronic superfluidity does not change the relation between the pressure and density inside a neutron star. Therefore the superfluidity has a minor influence on mass-radii relations of an isolated neutron star. However the superfluid state plays an important role in the description of the thermalization time and specific heat of the crust. In fact, the heat capacity of superfluid states is lower and proportional to $\exp\left(-\Delta/kT\right)$, where Δ is the pairing gap. The existing models of cooling are also very sensitive to the formation of the Cooper pairs. In the absence of superfluidity, the so-called "standard" scenario, the cooling rate is determined mainly by the direct and modified Urca reactions. The superfluidity suppresses the direct Urca processes and changes the cooling time significantly. In this case the radiation of neutrino-antineutrino pairs from the superfluid matter becomes possible [PGW06]. At the end, the creation of quantized vortices, which carry all the angular momentum of the superfluid, may explain the formation of pulsar glitches – sudden enhancement of their rotational frequency.

In this Chapter the pairing phenomenon on the base of BCS theory is outlined. Also the extension for finite temperatures is considered in the framework of Bogoliubov theory. This allows to include the pairing of nucleons in the Hartree-Fock calculations with finite temperatures.

3.1   The BCS Model

Analogously to the ground state of superconductors in the BCS theory [BCS57], let us consider the ground state of even-even nuclei in the form

$$|BCS\rangle = \prod_{i>0}(u_i + v_i c_i^\dagger c_{\bar{i}}^\dagger)|0\rangle. \tag{3.1}$$

Here the coefficients u_i and v_i can be determined from the condition that the corresponding energy has a minimum. Assuming that the BCS state is normalized to unity one obtains

$$u_i^2 + v_i^2 = 1. \tag{3.2}$$

In other words, the coefficient v_i^2 is a probability that the state i is occupied, and, respectively, the coefficient $u_i^2 = 1 - v_i^2$ is a probability that the same state is

empty. Now the ground state (3.1) is completely determined by the parameter v_i and condition (3.2).

The ground state (3.1), being the superposition of different number of pairs, violates the particle number conservation. This lack has no consequences in solid state physics due to enormous number of particles, however in nuclei this gives rise to serious errors. Therefore attempts have been made to project states with good particle number. Any variational calculation however must be constrained by a subsidiary condition, which fix the average particle number N

$$\langle BCS|\hat{N}|BCS\rangle = 2\sum_{i>0} v_i^2 = N. \tag{3.3}$$

Let us consider a system with N particles which is described by the Hamiltonian

$$H = \sum_{i,j \gtrless 0} \langle i|T|j\rangle c_i^\dagger c_j + \frac{1}{4}\sum_{i,j,k,l \gtrless 0} \langle ij|V|\widetilde{kl}\rangle c_i^\dagger c_j^\dagger c_k c_l, \tag{3.4}$$

where the first term is a single-particle energy and the second is the residual two-body interaction. The parameters u_i and v_i can be derived from the variation of energy with the constraint on the particle number. It leads to a new variational Hamiltonian

$$H' = H - \lambda\hat{N}, \tag{3.5}$$

where the Lagrange multiplier λ is known as the chemical potential or the Fermi energy of the system. The expectation value of (3.5) in BCS ground state reads

$$\langle BCS|H'|BCS\rangle = \sum_{i \gtrless 0}(\langle i|T|i\rangle - \lambda)v_i^2 + \frac{1}{2}\sum_{i,j \gtrless 0}\langle ij|V|\widetilde{ij}\rangle u_i^2 v_i^2 + \sum_{i,j>0}\langle i\bar{i}|V|\widetilde{j\bar{j}}\rangle u_i v_i u_j v_j. \tag{3.6}$$

The variation of (3.6) yields the set of BCS equations to determine v_i and λ

$$2\varepsilon_i u_i v_i + \Delta_i(v_i^2 - u_i^2) = 0, \tag{3.7}$$

with the single-particle energies

$$\varepsilon_i = \frac{1}{2}\left(\langle i|T|i\rangle + \langle\bar{i}|T|\bar{i}\rangle\right) + \sum_{j \gtrless 0}\left(\langle ij|V|\widetilde{ij}\rangle + \langle\bar{i}j|V|\widetilde{\bar{i}j}\rangle\right)v_j^2 - \lambda, \tag{3.8}$$

and the gap parameter

$$\Delta_i = -\sum_{j \gtrless 0}\langle i\bar{i}|V|\widetilde{j\bar{j}}\rangle u_j v_j. \tag{3.9}$$

29

Taking into account relations (3.2) and (3.7) one obtains two equations for v_i^2 and u_i^2

$$v_i^2 = \frac{1}{2}\left(1 - \frac{\varepsilon_i}{\sqrt{\varepsilon_i^2 + \Delta_i^2}}\right), \tag{3.10}$$

$$u_i^2 = \frac{1}{2}\left(1 + \frac{\varepsilon_i}{\sqrt{\varepsilon_i^2 + \Delta_i^2}}\right). \tag{3.11}$$

Equations (3.8), (3.9) and (3.10) must be solved self-consistently. The gap equation can be obtained by inserting (3.10) into (3.9)

$$\Delta_i = -\frac{1}{2}\sum_{j>0}\langle i\bar{i}|V|\widetilde{j\bar{j}}\rangle \frac{\Delta_j}{\sqrt{\varepsilon_j^2 + \Delta_j^2}}. \tag{3.12}$$

In the infinite matter the last equation can be written as [BC+90], [EH98], [KM+03]

$$\Delta(k) = -\frac{2}{\pi}\int_0^\infty dk' k'^2 V(k, k') \frac{\Delta(k')}{2E(k')}, \tag{3.13}$$

where $V(k, k')$ is the bare momentum-space NN interaction in the $^1S_0$ channel, $E(k')$ is the quasiparticle energy given by $E(k') = \sqrt{(\varepsilon(k') - \varepsilon_F)^2 + \Delta(k')^2}$, $\varepsilon(k)$ is the single-particle energy of a nucleon with momentum k, and k_F is the Fermi momentum. The singe-particle spectrum $\varepsilon(k)$ may be approximated by $\varepsilon(k) = k^2/2m$ [EH98]. In more sophisticated approaches, where the so-called conventional choice is used [KM+03], the single-particle energies below the Fermi energy are parameterized in terms of an effective mass of nucleons and a constant energy shift $\varepsilon(k) = k^2/(2m^*) + U$, while for the states above the Fermi energy the single-particle spectrum is replaced by the kinetic energy.

However in practical many-body calculations, e.g., in the Hartree-Fock method, the gap equation must be solved for every iteration. Therefore for the economy of cpu time the realistic interaction in (3.13) is usually replaced by an effective interaction. Bearing in mind that the pairing phenomenon is important for nucleons in vicinity of the Fermi surface, one can approximate the pairing interaction by a density-dependent zero-range effective potential, as it was suggested by Bertsch and Esbensen [BE91]

$$V_{pair}(\boldsymbol{r}_1, \boldsymbol{r}_2) = V_0\left(1 - \eta\left[\frac{\rho(\boldsymbol{r}_1)}{\rho_0}\right]^\alpha\right)\delta(\boldsymbol{r}_1 - \boldsymbol{r}_2), \tag{3.14}$$

where the parameters V_0, η, α were derived by Garrido *et al.* [GS$^+$99] by fitting the calculations of the symmetric matter with the Paris force. They found the following values: $V_0 = 481$ MeV fm^3, $\eta = 0.7$, and $\alpha = 0.45$. Integration in the gap equation (3.13) was performed below the cutoff parameter $\varepsilon_c = 60$ MeV, which corresponds to the cutoff in momentum space $k_c = \sqrt{2m\varepsilon_c} = 1.7$ fm^{-1}.

Solution of BCS equations must be performed for each iteration as it is shown on Fig.3.1. This includes the following steps:

i) One starts calculating the local gap function

$$\Delta^\tau(\mathbf{r}) = -V_{pair}(\mathbf{r})\,\chi^\tau(\mathbf{r}), \tag{3.15}$$

where $V_{pair}(\mathbf{r})$ is the contact interaction from (3.14), $\chi^\tau(\mathbf{r})$ is the anomalous density, and τ denotes the isospin number.

ii) From the local gap function the state-dependent pairing gap can be derived through

$$\Delta_\alpha^\tau = \int d^3\mathbf{r}\;\Delta^\tau(\mathbf{r})\;|\psi_\alpha^\tau(\mathbf{r})|^2 \tag{3.16}$$

and pairing energy, which contributes to the total energy per nucleon

$$E_{pair} = \frac{1}{2}\sum_{\alpha,q}\Delta_\alpha\zeta_\alpha. \tag{3.17}$$

iii) After that one should set a trial, initial value of the Fermi energy and calculate the quasi-particle energy E_α

$$E_\alpha = \sqrt{(\varepsilon_\alpha - \varepsilon_F)^2 + \Delta_\alpha^2}, \tag{3.18}$$

occupations v_α, u_α

$$v_\alpha^2 = \frac{1}{2}\left(1 - \frac{\varepsilon_\alpha - \varepsilon_F}{E_\alpha}\right), \tag{3.19}$$

$$u_\alpha^2 = \frac{1}{2}\left(1 + \frac{\varepsilon_\alpha - \varepsilon_F}{E_\alpha}\right), \tag{3.20}$$

and at the end the particle occupation η_α^τ

$$\eta_\alpha = v_\alpha^2, \qquad \zeta_\alpha = u_\alpha v_\alpha. \tag{3.21}$$

It allows to estimate the number of particles N from

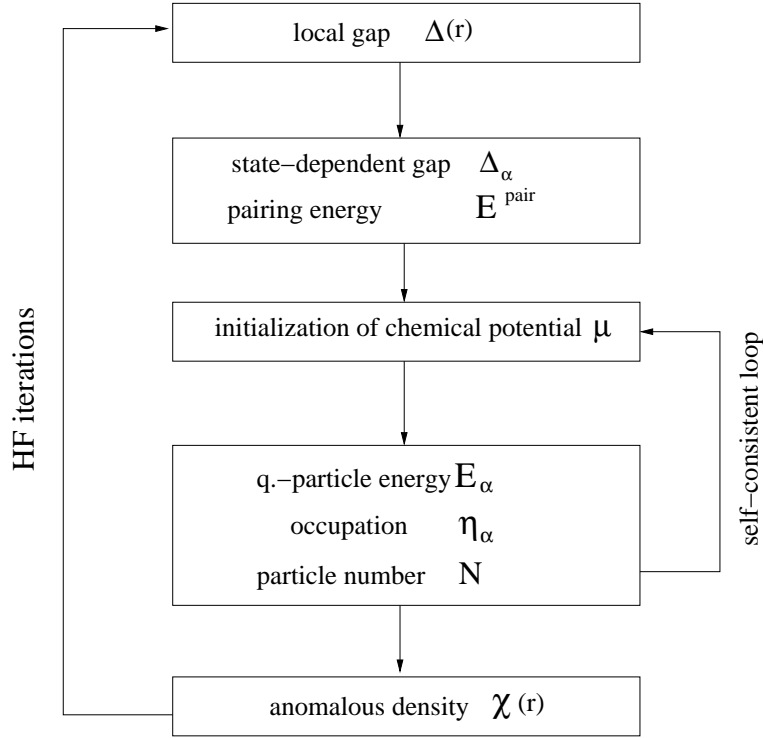$$N = \sum_\alpha \eta_\alpha. \tag{3.22}$$

Figure 3.1: The self-consistent loop to determine the pairing gap and the occupation scheme within the Hartree-Fock program.

If it is not equal to the desired number of nucleons – the Fermi energy ε_F in (3.18) should be modified. In such a way it makes the self-consistent loop at each HF iteration.

iv) Finally, the anomalous density is calculated from

$$\chi(\mathbf{r}) = \tfrac{1}{2} \sum_{\alpha} \zeta_\alpha \, |\psi_\alpha(\mathbf{r})|^2 \, f_{c,\alpha}. \tag{3.23}$$

To increase the convergence in the summation (3.23), the later must be multiplied with a sharp cutoff, which varies between 0 and 1. This procedure works well if the pairing phase space expanded up to 50 MeV above the Fermi surface. However more stable solution may be achieved by using a soft cutoff [BF+85]

$$f_{c,\alpha} = [1 + \exp((\varepsilon_\alpha - (\varepsilon_F + \varepsilon_c))/\Delta\varepsilon)]^{-1} \,, \tag{3.24}$$

where the cutoff energy $\varepsilon_c = 5$ MeV and $\Delta\varepsilon = \varepsilon_c/10$.

3.2 Pairing at Finite Temperatures

In the last section the zero temperature pairing phenomenon based on BCS was discussed. Being introduced into the Hartree-Fock calculations, this yields the so-called Hartree-Fock plus BCS (HF+BCS) approach. In this Section this model is extended in order to take into account the effects of finite temperatures.

The most general theory of pairing in the mean-field calculations allowing the finite temperature effects is the theory developed by Bogoliubov. Below the basic formalism of this theory is outlined. Later it is adopted to formulate the finite temperature BCS (FT-BCS) method used in the Hartree-Fock calculations. More detailed description can be found in textbooks (see, e.g., [RS80]).

The main idea of Bogoliubov theory is to represent the ground state (3.1) of interacting particles as a vacuum of non-interacting quasiparticles

$$\alpha_k |BCS\rangle = 0, \ \forall k \neq 0. \tag{3.25}$$

The particle creation and annihilation operators $c_i^\dagger$, c_i are related with the creation and annihilation operators for quasiparticles $\alpha_k^\dagger$, α_k by the Bogoliubov transformation. Its matrix form can be written as

$$\begin{pmatrix} \alpha^\dagger \\ \alpha \end{pmatrix} = \begin{pmatrix} U & V \\ V^* & U^* \end{pmatrix} \begin{pmatrix} c^\dagger \\ c \end{pmatrix}, \tag{3.26}$$

where matrices U and V satisfy

$$UU^\dagger + VV^\dagger = 1, \qquad UV^T + VU^T = 0. \tag{3.27}$$

By using the algebraic relations between particles and quasiparticles one can obtain the Hartree-Fock-Bogoliubov (HFB) Hamiltonian from (3.5)

$$H - \mu \hat{N} \approx H_{HFB} = E_0 + \sum_k E_k \alpha_k^\dagger \alpha_k. \tag{3.28}$$

Here μ stands for the chemical potential, $\hat{N}$ is the particle number operator, E_k is the quasiparticle energy and E_0 is the ground state energy.

Now let us consider a system of N particles at finite temperatures in thermal equilibrium. Its grand potential Ω is determined as

$$\Omega = \mathcal{E} - TS - \mu N, \tag{3.29}$$

where $\mathcal{E}$ is the total energy and S is the system entropy. At the constant temperature T and the chemical potential μ the equilibrium state of mechanically isolated system minimizes the grand potential

$$\delta\Omega = 0. \tag{3.30}$$

This variation is realized by

$$\frac{\delta\Omega}{\delta\mathcal{D}} = 0, \tag{3.31}$$

where the density operator $\mathcal{D}$ has the property

$$\mathrm{Tr}\mathcal{D} = 1. \tag{3.32}$$

The trace in (3.32) assumes the summation over all states with any number of particles or quasiparticles. The density operator, which satisfy both (3.32) and (3.31) has the form

$$\mathcal{D} = Z^{-1}e^{-\beta(H-\mu\hat{N})}, \tag{3.33}$$

where Z denotes the grand partition function

$$Z = \mathrm{Tr}[e^{-\beta(H-\mu\hat{N})}] \tag{3.34}$$

and $\beta = 1/kT$. In finite temperature Bogoliubov theory the Hamiltonian H in (3.33) and (3.34) is replaced with the HFB Hamiltonian (3.28). As it was derived in [Go81] the HFB density operator is

$$\mathcal{D}_{HFB} = \prod_k [n_k\alpha_k^\dagger\alpha_k + (1-n_k)\alpha_k^\dagger\alpha_k], \tag{3.35}$$

where n_k stands for the quasiparticle occupation number of k-th orbit. This is determined as the expectation value of the quasiparticle number operator $\mathcal{N}_k = \alpha_k^\dagger\alpha_k$

$$n_k = \langle\mathcal{N}_k\rangle = \mathrm{Tr}(\mathcal{D}_{HFB}\,\mathcal{N}_k) = \frac{1}{e^{\beta E_k}+1}. \tag{3.36}$$

The Hartree-Fock Hamiltonian $\mathcal{H}$ has the same form as in zero temperature case

$$\mathcal{H} = \mathcal{T} - \mu + \Gamma. \tag{3.37}$$

The HF potential and the pair potential are defined by

$$\Gamma_{ij} = \sum_{kl}\langle ik|V|jl\rangle\rho_{lk}, \tag{3.38}$$

$$\Delta_{ij} = \frac{1}{2} \sum_{kl} \langle ij|V|kl\rangle \tau_{kl}. \tag{3.39}$$

Here the particle densities are derived from the inverse Bogoliubov transformation

$$\rho = U^T n U^* + V^\dagger (1-n) V, \qquad \tau = U^T n V^* + V^\dagger (1-n) U. \tag{3.40}$$

The total energy, entropy and particle number are evaluated in HFB approximation

$$E = \text{Tr}[(\mathcal{T} + \frac{1}{2}\Gamma)\rho + \frac{1}{2}\Delta\tau^\dagger], \tag{3.41}$$

$$S = -\sum_\alpha [n_\alpha \ln(n_\alpha) + (1-n_\alpha)\ln(1-n_\alpha)], \tag{3.42}$$

$$N = \text{Tr}\rho. \tag{3.43}$$

By using these expressions, one can derive the finite temperature HFB (FT-HFB) equations from the variation (3.30)

$$\begin{pmatrix} \mathcal{H} & \Delta \\ -\Delta^* & -\mathcal{H}^* \end{pmatrix} \begin{pmatrix} U_\alpha \\ V_\alpha \end{pmatrix} = E_\alpha \begin{pmatrix} U_\alpha \\ V_\alpha \end{pmatrix}. \tag{3.44}$$

These equations have the same form as zero temperature HFB equations [RS80]. The difference consists in quasiparticle occupation (3.36), so that the densities ρ and τ at $T \neq 0$ differ from those obtained at $T = 0$.

The finite temperature BCS limit of FT-HFB theory can be obtained if the time-reversal symmetry together with a monopole pairing force are considered. In this case the FT-HFB equations (3.44) become diagonal and yield the well-known FT-BCS equations. Thus the gap equation can be written as

$$\Delta_\alpha = -\frac{1}{2} \sum_{k'>0} \langle k\bar{k}|\bar{V}|k'\bar{k}'\rangle (1-2n_{k'}) \frac{\Delta_{k'}}{2E_{k'}}, \tag{3.45}$$

where $|\bar{k}\rangle$ denotes the time-reversed state of $|k\rangle$. The quasiparticle energy E_k and coefficients u_k, v_k are the same as in the BCS theory, and obey

$$u_k v_k = \frac{\Delta_k}{2E_k}. \tag{3.46}$$

From equations (3.45) and (3.46) the normal and anomalous occupation factors of the Hartree-Fock single-particle states can be obtained from

$$\eta_k = (1-2n_k)v_k^2 + n_k, \tag{3.47}$$

$$\zeta_k = (1-2n_k)u_k v_k. \tag{3.48}$$

Finally, both η_k and ζ_k are used instead of (3.21). This allows us to consider pairing effects with finite temperatures in the Hartree-Fock calculations.

Chapter 4

Structure of Pasta Phase

In this Chapter the region of existence of the pasta phase in the crust of neutron stars is investigated. Also we pay a special attention to the comparison of the inhomogeneous density distribution with the homogeneous matter and the temperature stability of the inhomogeneous structures. All pasta objects resulted from the Skyrme Hartree-Fock calculations in cubic WS cell are considered. Later we focus on the internal structure of the droplet phase derived within the spherical WS cell. It allows us to study the single-particle levels similar to the standard nuclear shell model and investigate the dynamical response function of such droplet.

4.1 Microscopical Structure of Pasta Phase

To investigate the nuclear matter under conditions existing in the crust of neutron stars we perform Skyrme Hartree-Fock calculations for the charge neutral nuclear matter within the WS cell approximation as described in the Chapter 2. The matter consists of protons, neutrons and electrons which exist in β-equilibrium, i.e. their chemical potentials satisfy the relation

$$\mu_n = \mu_p + \mu_e. \tag{4.1}$$

The density distributions of protons and neutrons in the inner crust of neutron stars are determined by the interplay of the Coulomb force and the surface tension, as it was predicted in early 1980's by Ravenhall et al. [RPW83]. At the low density $\rho \sim 0.1\rho_0$ the nuclear matter is formed of spherical nuclei, since in this way the
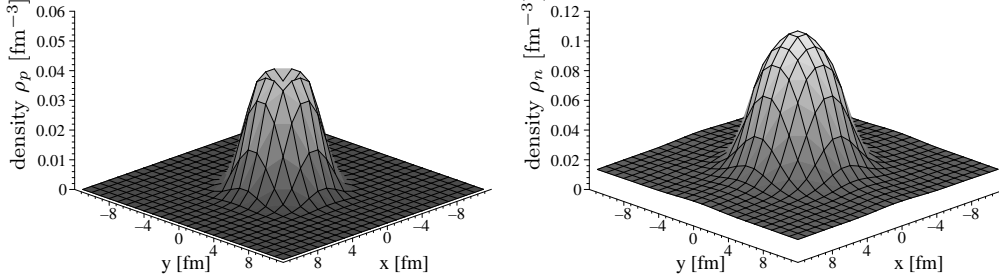
Figure 4.1: Density distribution of protons (left panel) and neutrons (right panel) resulting from Skyrme HF + BCS calculation at an average density of $\rho = 0.0166$ fm^{-3} (droplet).

surface and Coulomb energies are minimized. With increasing density, however, the density distributions may become very deformed, thus cylindrical and planar geometries can occur.

At the density $\rho = 0.0166$ fm^{-3} the solution of the Hartree-Fock equations with SLy4 potential yields the spherically symmetric density distribution of nucleons, which is often called the droplet phase (see Fig.4.1). As we will see later, the proton fraction in the droplet phase is about 4%, therefore all protons are bound[1], and their density distribution is localized at the center of the WS cell similar to the finite nuclei. Neutrons, in their turn, also form a quasinucleus at the center of the cell, however on periphery their distribution is nonvanishing and uniform, and is determined by the dripped neutrons. Due to the periodicity of the boundary conditions the crust can be considered as a lattice of quasinuclei embedded in the sea of electrons and dripped neutrons.

Increasing the global density of the matter the distributions of protons and neutrons become deformed. At the density $\rho = 0.0625$ fm^{-3} the protons and neutrons density profiles in x, y-plane are symmetric and localized at the center of the cell (see left panels of Fig.4.2 and Fig.4.3). However in x, z-plane these distributions are asymmetric (see right panels of Fig.4.2 and Fig.4.3), so that the density is a constant along z-axis. This density profile can be identified with a cylinder or rod oriented along z-axis. At the global density $\rho = 0.775$ fm^{-3} the central density distributions

---

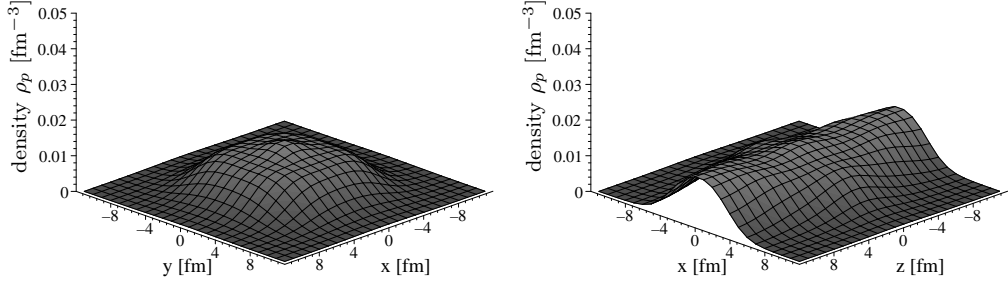[1]The β-equilibrium condition must be fulfilled.

Figure 4.2: Proton density distribution for Skyrme HF + BCS calculation at an average density of $\rho = 0.0625 \, \mathrm{fm}^{-3}$ (rod).
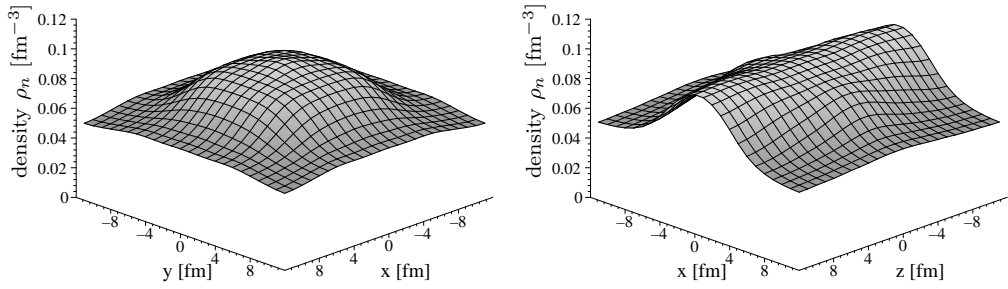

Figure 4.3: Neutron density distribution for Skyrme HF + BCS calculation at an average density of $\rho = 0.0625 \, \mathrm{fm}^{-3}$ (rod).
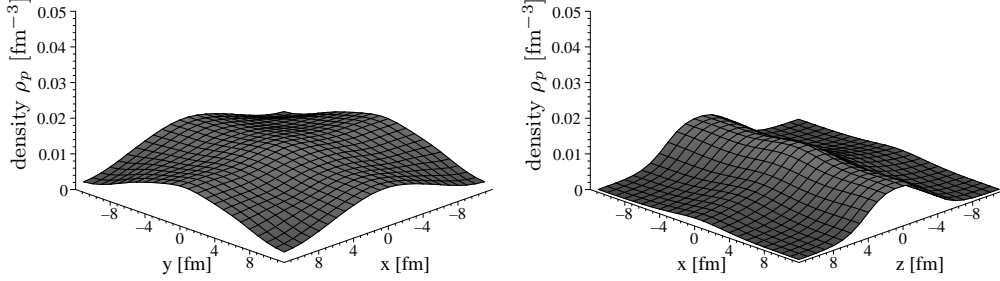
Figure 4.4: Proton density distribution for Skyrme HF + BCS calculation at an average density of $\rho = 0.0775$ fm^{-3} (slab).

of nucleons in x, y-plane become almost flat. They are shown on the left panels of Fig.4.4 and Fig.4.5 for protons and neutrons, respectively. In x, z-plane the density profiles are constant in x-direction but crosses the z-axis (right panels Fig.4.4 and Fig.4.5). This quasinucleus looks like a slab. In the following we will refer to the cylindrical and slab quasinuclei as rod and slab phases, respectively. In the literature they are also known as "spaghetti" and "lasagna". Increasing the density up to $0.6\rho_0$ we can observe the dissociation of neutrons: they drip out of nuclei, thus the transition to the homogeneous matter occurs. As we can see, the pasta phase[2] exists in a thin layer of the crust and connects the inner crust, where the nuclear matter consists of the spherical nuclei embedded in the electron sea with the outer core, characterized by the homogeneous nuclear matter distribution, which appear at about the half of the saturation density ρ_0.

Up to now the zero temperature case was discussed. To investigate the pasta phase at $T \neq 0$ we performed the Skyrme Hartree-Fock calculations using the FT-BCS scheme of the occupation, as described in the Chapter 3. If the temperature of matter rises, the pasta phase structures become smooth and at some critical temperature they disappear, so that the homogeneous density distribution is observed. For SLy4 potential the critical temperature was found to be about 5 MeV and 10 MeV for slab and rod structures, respectively, while the droplet structure disappears at the temperature higher than 15 MeV. Thus the spherically symmetric droplet phase will play the main role in different simulations involving a wide range of temperatures.

---

[2]Under "pasta" we will assume the droplet, rod and slab phases.
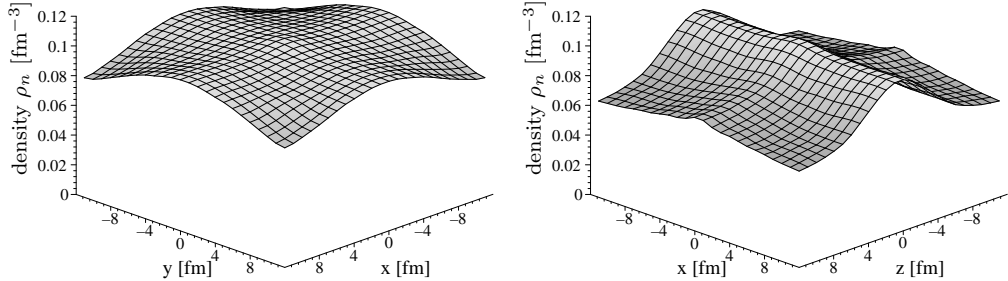
Figure 4.5: Neutron density distribution for Skyrme HF + BCS calculation at an average density of $\rho = 0.0775$ fm^{-3} (slab).

On the phase diagram "temperature-density" Fig.4.6 we demonstrate schematically the region of existence of the pasta phase, derived from the Skyrme Hartree-Fock calculations, and the transition to the homogeneous matter with the increase of density and temperature.

Now let us concentrate on the study of the inner structure of pasta objects, and for simplicity we will restrict to the case of spherically symmetric droplet phase. This reduces the computational time and allows to investigate the dynamical response function by using the standard methods of nuclear physics.

Assuming the spherical symmetry the single-particle (s.p.) wave functions (WF's) are expended in a complete basis set of orthogonal states defined within a spherical box of radius R

$$\Psi(\boldsymbol{r}) = \sum_{i=1}^{\infty} c_{ilj}\varphi_{iljm}(\boldsymbol{r}) \approx \sum_{i=1}^{N} c_{ilj}\varphi_{iljm}(\boldsymbol{r}), \qquad (4.2)$$

where c_{ilj} are expansion coefficients and $\varphi_{iljm}(\boldsymbol{r}) = \langle \boldsymbol{r}|\alpha\rangle$ are the WF of the orthonormal basis. The number of basis states N has to be chosen to guarantee that the results are not affected by this limitation. The orthonormal set of basis functions, which are regular at the center of the box is given by

$$\varphi_{iljm}(\boldsymbol{r}) = \langle \boldsymbol{r} \ |iljm\rangle = \mathcal{R}_{il}(r)\mathcal{Y}_{ljm}(\theta,\varphi), \qquad (4.3)$$

where $\mathcal{Y}_{ljm}(\theta,\varphi)$ represents the spherical harmonics including the spin degrees of freedom by coupling the orbital angular momentum l with the spin to a single-particle angular momentum j. The radial WF's $\mathcal{R}_{il}$ are given by the spherical
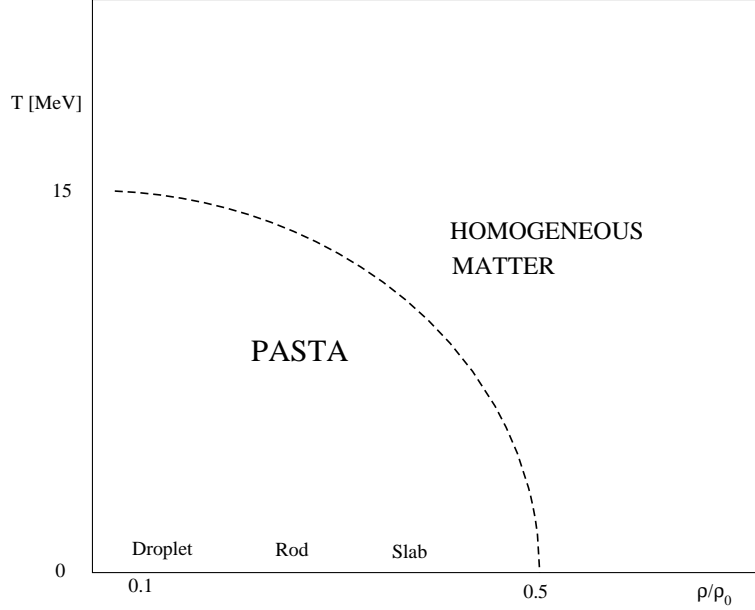
Figure 4.6: Phase diagram of inhomogeneous structures in nuclear matter derived from HF calculations with SLy4 potential.

Bessel functions for the discrete momenta k_i [MMM04],

$$\mathcal{R}_{il}(r) = N_{il} j_l(k_i r), \tag{4.4}$$

which fulfill the Dirichlet boundary conditions

$$N_{il} j_l(k_i R) = 0, \tag{4.5}$$

where the normalization constant is

$$N_{il} = \begin{cases} \frac{\sqrt{2}}{\sqrt{R^3} j_{l-1}(k_i R)}, & l > 0 \\ \frac{i\pi\sqrt{2}}{\sqrt{R^3}}, & l = 0, \end{cases} \tag{4.6}$$

and it ensures the basis functions are orthogonal and normalized within the box. The use of the Dirichlet boundary conditions for all s.p. WF's leads to the suppression of the local density at the border of the cell. There exists an alternative choice for the radial wave functions, where the radial derivative of the WF vanishes at the border of the cell (Von Neuman boundary conditions)

$$\tilde{\mathcal{R}}_{il}(r) = \tilde{N}_{il} j_l(\tilde{k}_i r), \ \frac{\partial \tilde{\mathcal{R}}_{il}(R)}{\partial r} = 0. \tag{4.7}$$
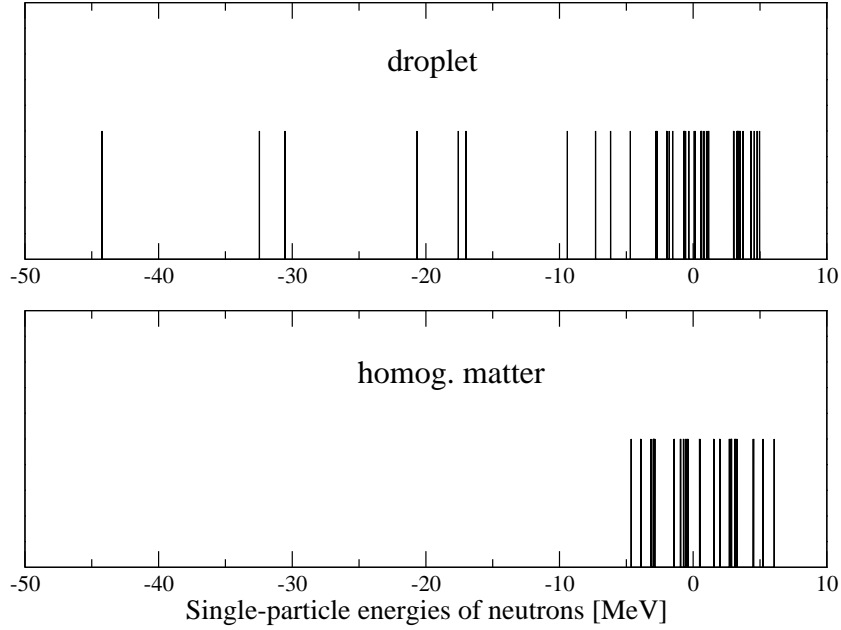
Figure 4.7: Neutron single-particle structure of droplet (top) and homogeneous matter (bottom) at the same global density.

This determines a new set of momenta $\tilde{k}_i$ and normalization constants $\tilde{N}_{il}$. To get a smooth transition of density profile from one WS cell to another one Bonche and Vautherin [BV81] suggested using a mixed basis by employing the Dirichlet boundary conditions (4.5) for the states with even orbital momentum l, and Von Neuman boundary conditions (4.7) for the states with odd l[3]

$$\int_0^R d\boldsymbol{r}\ \varphi_{iljm}^*(\boldsymbol{r})\varphi_{i'l'j'm'}(\boldsymbol{r}) = \delta_{ii'}\delta_{ll'}\delta_{jj'}\delta_{mm'}. \tag{4.8}$$

Many authors investigating the inner crust of NS consider, for simplicity, the homogeneous matter distribution and in such a way neglect the region where the pasta phase occurs. Therefore we should pay a special attention for the comparison of the pasta phase (inhomogeneous matter) with the homogeneous matter at the same global density.

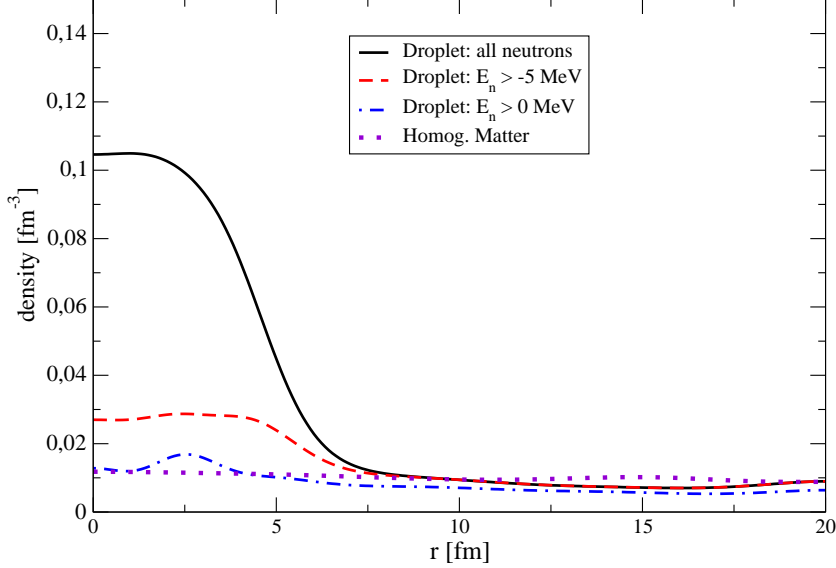
[3]See also discussions in [MMM04].

Figure 4.8: Neutron density distribution in droplet (solid) and homogeneous matter (dotted).

For the comparison of the homogeneous and inhomogeneous density distributions we take the configuration with $Z = 14$, $N = 320$ in the cell with radius of R = 20 fm and the average global density $\rho = 0.0094$ fm^{-3}.

On the top of Fig.4.7 the energies of occupied single-particle neutron levels in droplet are shown. The deepest occupied state occurs at the energy $E_n^{1s_{1/2}} = -44$ MeV. One can also observe a big amount of dripped ($E_n > 0$) neutrons: about 60% of the total number of neutrons. On the bottom of Fig.4.7 the single-particle spectrum of neutrons in homogeneous matter is displayed. Evidently, in the case of the homogeneous density distribution neutrons are delocalized and weakly bound. About 10% of neutrons in the droplet (from the left) are deeply bound ($E_n < -5$ MeV) and they have no "partners" in homogeneous matter, since all neutrons of homogeneous matter are distributed over a narrow energy interval from -5 MeV to 7 MeV. Further, under the deeply bound neutrons, we will assume all neutrons of the inhomogeneous matter phase (droplet) with the energy, which is less than the deepest occupied level of neutrons in homogeneous matter at the same global density. The role of these neutrons in formation of the inhomogeneous density distribution becomes obvious

if we compare the neutron density profiles of the droplet and homogeneous matter on Fig.4.8. First of all, one can notice that the density distribution of homogeneous matter slightly fluctuates over the average value $\rho = 0.0094$ fm^{-3}. Such fluctuations cannot be avoided if one represents the infinite matter in the box of the finite volume. The nature of these fluctuations lies in the spurious shell effects due to the discretized energy spectrum of the free neutrons [MMM04]. Coming back to the inhomogeneous density distribution one can see that the core of the droplet is formed mainly by the deeply bound neutrons ($E_n < -5$ MeV), while the dripped neutrons contribute mainly to the "tail" of the density distribution. So, as we expected, the use of the mixed (Dirichlet-Von Neuman) boundary conditions gives a smooth non-vanishing density at the border of the cell. In the next Section the connection of the internal droplet structure with the dynamical response is investigated.

4.2 Dynamical Response of Pasta Phase

The nuclear response function to an external probe with the momentum transfer q and the energy transfer ω, is proportional to the imaginary part of the polarization propagator

$$S(q,\omega) = -\frac{1}{\pi} Im\Pi(q,\omega), \qquad (4.9)$$

where

$$\Pi(q,\omega) = \sum_{n \neq 0} \langle \psi_0 | \hat{O}_\alpha(q) | \psi_n \rangle \langle \psi_n | \hat{O}_\alpha^\dagger(q) | \psi_0 \rangle \qquad (4.10)$$

$$\times \left[\frac{1}{\hbar\omega - (E_n - E_0) + i\eta} - \frac{1}{\hbar\omega + (E_n - E_0) - i\eta} \right], \qquad (4.11)$$

where $\{|\psi_n\rangle\}$ is a complete set of the nuclear eigenstates with the energy E_n, $\hat{O}_\alpha(q)$ is the vertex operator in the second quantization formalism, and α labels the spin-isospin channel. In the following we will deal with the scalar-isoscalar channel, where $\hat{O}(q) = e^{i\boldsymbol{qr}}$. The response function $S(q,\omega)$ demonstrates the available phase space for the absorption of an excitation phonon with a given q and ω.

In the mean-field model $S(q,\omega)$ can be written through the particle-hole (*ph*) po-

larization propagator as

$$S(q, \omega) = -\frac{1}{\pi} Im \sum_J \Pi^J(q, \omega), \qquad (4.12)$$

$$\Pi^J(q, \omega) = \sum_{ph} A^{JJ0}(q)[\frac{1}{\hbar\omega - (E_n - E_0) + i\eta} \qquad (4.13)$$

$$-\frac{1}{\hbar\omega + (E_n - E_0) - i\eta}]A^{JJ0 \, *}(q), \qquad (4.14)$$

where $p(h)$ labels a complete set of particle (hole) quantum numbers and

$$A^{Jl\sigma}(q) = \langle j_p j_h; J | l\sigma; J \rangle (-i)^{l+1} \sqrt{(2l_p + 1)(2l_h + 1)} \qquad (4.15)$$

$$\times \int_0^\infty dr r^2 \mathcal{R}_p(r) j_l(qr) \mathcal{R}_h(r) \begin{pmatrix} l_p & l_h & l \\ 0 & 0 & 0 \end{pmatrix}. \qquad (4.16)$$

Here $\langle j_p j_h; J | l\sigma; J \rangle$ stands for the standard LS-jj coupling coefficient, $\mathcal{R}_{p(h)}(r)$ is the radial wave function of particle (hole) state with the energy $E_{p(h)}$. The response function calculated from the discrete set of the final states within the WS cell approximation consists of a collection of the delta function peaks localized at the energies $E_n = E_0$[4]. Replacing the energy conserving δ-function by the Lorentz representation with a finite width γ

$$\delta(x) \rightarrow \frac{1}{\pi} \frac{\gamma/2}{(x - \gamma)^2 + \gamma^2/4} \qquad (4.17)$$

one can get $S(q, \omega)$ as a smooth function of ω. We used the value $\gamma = 0.5$ MeV for the Lorentz width to reproduce the response of the free Fermi gas (Appendix A) with the best accuracy.

In Fig.4.9 the response functions of neutrons in the droplet for the different values of the momentum transfer q are shown. At $q = 0.2$ fm^{-1} the main contribution to the response is due to the weakly bound neutrons at low excitations energy of about 3 MeV. The nature of this peak is easy to understand considering the radial integral in (4.15). At small q the main overlap is between the radial wave functions, which lie very close to the Fermi surface, i.e., the respective excitation energies are few MeV. With increasing momentum transfer q up to 0.5 fm^{-1} increases proportionally the

---

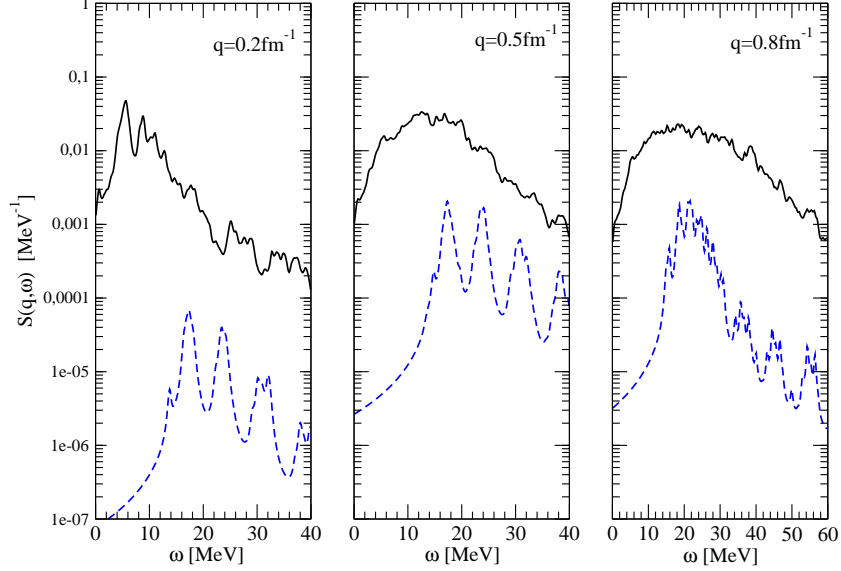[4]The finite size of the system will quantize the energy spectrum of the unbound single-particle states.

Figure 4.9: Response function of droplet (black solid). Contribution of deeply bound neutrons (blue dashed). The global density $\rho = 0.0094$ fm^{-3}.

transition probability from the deeper occupied states to the states above the Fermi level. The maximum is thus shifted to the higher excitations energies. A smearing in the overlap integral (4.15) leads to the respective smearing of the response function over the wider range of ω. This effect becomes more significant at higher momenta.

Since one of the goals of this Chapter is to investigate the role of the deeply bound neutrons in the formation of the response function of the nuclear matter, we separated their contribution from the total result at different momentum transfers. It is shown as the blue dashed curve on Fig.4.9. At the low momentum transfer the response function of neutrons with the energy $E_n < -5$ MeV appears at high excitation energies and is one order less amplitude than the total result at the same excitation energy. The growth of the momentum q increases the role of the quasi-nucleus since the overlap between the deeply bound initial and high-oscillating final wave functions becomes larger. Nevertheless the absolute contribution of the deeply bound neutrons to the total sum rule hardly exceeds few percent.

This situation is changed significantly if one considers lower densities, where the difference between the homogeneous and inhomogeneous matter increases. Investi-
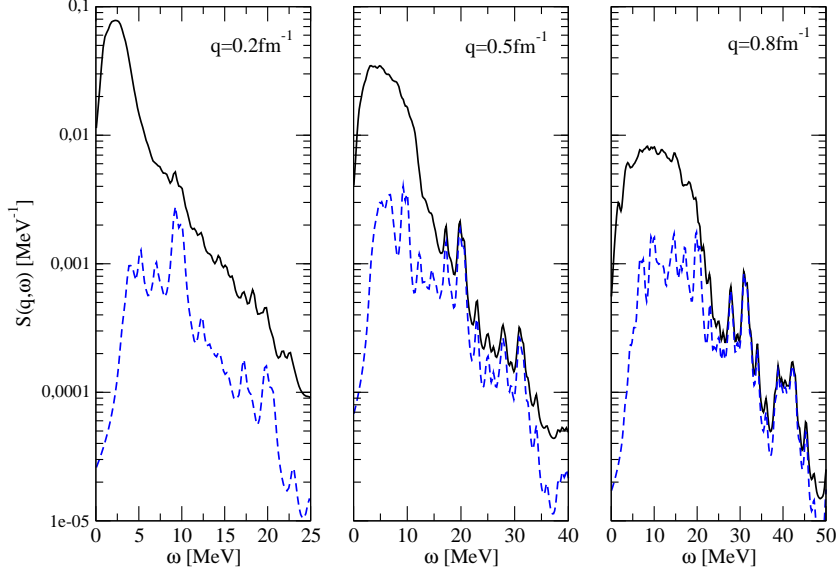
Figure 4.10: Response of droplet (black solid). Contribution of deeply bound neutrons (blue dashed). The global density $\rho = 0.0023$ fm^{-3}.

gating this case we consider the nuclear matter with the global density $\rho = 0.0023$ fm^{-3} in β-equilibrium. On the one hand, the proton fraction of the droplet in this case exceeds 6% and the neutron potential well becomes deeper. On the other hand, the proton fraction of the homogeneous matter is less than 0.2% and neutrons become less bound and the first occupied neutron level appears at -0.7 MeV. Therefore the number of the deeply bound neutrons in droplet increases, and proportionally increases their role in the response function.

In Fig.4.10 the response of the inhomogeneous β-stable nuclear matter is shown. The contribution of neutrons with the energy less than -0.7 MeV is substantial and rises with the transferred momentum. Starting from $q = 0.5$ fm^{-1} these neutrons dominate in the formation of the response function at high energies.

Thus we conclude that the deeply bound neutrons play the main role in the formation of the inhomogeneous density distributions, although their contribution to the response function is quite small, and does not exceed few percent in terms of the energy weighted sum rules.

Chapter 5

Neutrino Mean Free Path in the Crust

In this Chapter we formulate an approach to calculate the neutrino mean free path (NMFP) in nuclear system, which is described in Skyrme Hartree-Fock as well as in the relativistic mean field model with inclusion of pairing correlations. We pay special attention to the details of neutrino propagation in the presence of pasta phase, taking into account all its geometrical shapes: spherical droplets, cylindrical rods and planar slabs. Therefore we will use the results of the self-consistent HF calculations with SLy4 potential within the cubic WS cell, considered in Chapter 4. To describe the charge neutral matter containing protons, neutrons and electrons in β-equilibrium we consider a box of a typical size about 20 fm. Pairing correlations were included in terms of the BCS approximation by assuming a density-dependent zero-range pairing force as described in Chapter 3.

5.1 The Skyrme Hartree-Fock Model

We perform the self-consistent HF calculations with inclusion of pairing in a periodic lattice of WS cells of cubic shapes. The symmetry of such WS cell not only allows the formation of triaxial structures but also includes rod- and slab-like structures and provide a natural transition to homogeneous matter [G07].

At the density 0.0166 fm^{-3}, we observe the spherical droplet phase, while density distributions identified with rods and slabs appear at 0.0625 fm^{-3} and 0.0775 fm^{-3},

respectively. Thus we fix three values of density, whose profiles possess a clear spatial distribution and can be identified with the known pasta structures from other calculations [MH02]. Increasing density from 0.0166 fm^{-3} to 0.0775 fm^{-3}, one obtains a variety of different intermediate density profiles which smoothly connect three representatives: droplet $\rightarrow$ rod $\rightarrow$ slab.

As mentioned above, the Hartree-Fock calculations were performed within the WS cell approximation, assuming that the inner crust is divided into independent cubic cells, and the wave functions of dripped, unbound neutrons satisfy the periodic boundary conditions. However, from the standard model of neutron stars [BBP71], it is known that the inner crust is a perfect crystal and therefore the band theory of solids should be applied for the unbound neutrons. In this case the energy spectrum of unbound neutrons will be formed of "bands" in momentum space, thus containing more information than in the WS cell approximation. However, as it has been shown in recent investigations by Chamel et al. [CN^{+}08], the differences between the full band theory and WS approximation are expected to be essential when the processes under considerations involve energy transfer, which is comparable with the level spacing induced by discretization. In our calculation such level spacing in the energy spectrum of unbound neutrons does not exceed 200 keV; therefore, we suppose that the WS approximation is a good starting point for the calculation of NMFP with energies of the incoming neutrinos $10 \leq E_\nu \leq 100$ MeV. To check the accuracy of our method we also perform the plane wave test, which is considered in the next Section.

The single-particle energies and wave functions for protons and neutrons resulted from the Hartree-Fock calculations were used to evaluate the NMFP by using the method outlined in the following Section.

5.2 Mean Free Path in Nonrelativistic Model

In Appendix A we show how one can derive the NMFP of a free Fermi gas from the cross section of neutrino in charged current (CC) and neutral current (NC) processes. Following this idea we extract the mean free path in nuclear matter from the cross section of neutrinos on quasi nuclear structures inside the WS cell.

The matrix element for the neutrino-nucleus interactions $\nu + n \rightarrow \nu + n$

$(\nu + n \rightarrow p + e^-)$ is given by

$$M = \frac{G_F C}{\sqrt{2}} J_\mu j^\mu, \tag{5.1}$$

where

$$J_\mu = i\bar{u}_{n(p)}(V\gamma_\mu + A\gamma_\mu\gamma_5)u_n, \tag{5.2}$$

$$j^\mu = -i\bar{u}_\nu\gamma^\mu(1 - \gamma_5)u_{\nu(e)} \tag{5.3}$$

are hadronic and leptonic currents, respectively. The parameters A, V must be replaced by the respective values of coupling constants and C stands for the Cabbibo factor in the charged-current reaction [SL]. The total cross section can be written as

$$\sigma = \sum_f p_{\nu(e)} E_{\nu(e)} \frac{1}{2} \int\limits_{-1}^{1} d(\cos\vartheta)\overline{|M|}^{\,2}, \tag{5.4}$$

$$\overline{|M|}^{\,2} = \frac{G_F^2 C^2}{\pi} \left[V^2(1 + \cos\vartheta)|M_1|^2 + A^2(1 - \frac{1}{3}\cos\vartheta)|M_2|^2 \right], \tag{5.5}$$

$$M_1 = \langle\varphi_4|e^{i\boldsymbol{q}\boldsymbol{r}}|\varphi_2\rangle, \quad M_2 = \langle\varphi_4|\boldsymbol{\sigma}e^{i\boldsymbol{q}\boldsymbol{r}}|\varphi_2\rangle, \tag{5.6}$$

where within this non-relativistic approach we neglect the lower components in Dirac spinors $u \simeq \binom{\varphi}{0}$. In the charged current reaction, the influence of the Coulomb field on the outgoing electron can be taken into account by multiplying the cross section by the Fermi function $F(Z_f, E_e)$ [EG70]. For this reaction, M_1 and M_2 stand for the Fermi and Gamow-Teller matrix elements, respectively. The integration is performed over the spatial angle ϑ between the momenta of incoming and the outgoing leptons. The single-particle wave functions $\varphi(\boldsymbol{r})$ and single-particle energies ε_f (ε_i) are obtained from the solution of the HF equations. Note that these single-particle energies enter (5.4) as the energy for the outgoing lepton is defined as

$$E_{\nu(e)} = E_\nu^{in} + \varepsilon_i - \varepsilon_f,$$

where E_ν^{in} is the energy of the incoming neutrino.

The formalism described so far is appropriate for the neutrino-nucleus interaction. With some extensions it may also be used to evaluate the interaction of neutrinos with the quasi-nuclear structures in the crust of neutron stars. Unlike spherical nuclei and the case of the droplet phase, the cross section of neutrino on rods and slabs, generally speaking, depends on the spatial orientation of momentum transfer $\boldsymbol{q}$

in (5.6), since the density distributions of rod and slab phases are nonspherical, as it is shown on Figs.4.2-4.5. The precise averaging over all possible mutual orientations of vectors $\boldsymbol{q}$ and $\boldsymbol{r}$ requires additional numerical efforts. Thus, in order to reduce this effort, we considered three particular cases, with the vector $\boldsymbol{q}$ along the direction of the x, y and z-axis. Doing so, we determine the averaged cross section as

$$\sigma = \frac{1}{3}(\sigma_x + \sigma_y + \sigma_z), \tag{5.7}$$

where $\sigma_{x(y,z)}$ represents the cross section calculated for the momentum transfer along $x(y,z)$-axis.

In contrast to a finite nucleus, the WS cell of the inhomogeneous nuclear matter contains a large number of unbound neutrons, which give nonzero contribution to the total cross section. Thus, the cross section consists of two parts: the cross section due to the interaction with the nucleons bound in the quasi-nuclear structure and the cross section due to the interaction with unbound neutrons. Therefore, one can consider (5.4) as a cross section of neutrinos with all nucleons in a given volume V_{cell} of a WS cell. The reverse NMFP can then be written as

$$\frac{1}{\lambda} = \frac{\sigma}{V_{cell}}. \tag{5.8}$$

Another important distinction of the pasta structures in the crust of neutron stars from the finite, isolated nuclei consists in the existence of the electron sea in the volume of the WS cell. Therefore, the nonzero chemical potential of electrons must be taken into account in the evaluation of charged current reactions by a blocking of final states for electrons with energies below the respective Fermi energy μ_e.

To test the accuracy of our approach we perform a numerical check in the absence of the nucleon-nucleon interaction. Thus all particles are free and can be described by plane waves. The NMFP in this case can be determined analytically from the response function $S(q,\omega)$, as described in Appendix A. On Fig.5.1 we compare the NMFP derived from the WS cell with the analytical result in CC reaction for two values of matter density: 0.01fm^{-3} (upper curve) and 0.02fm^{-3} (lower curve). A small deviation is caused by the discretization of the continuum energy spectrum. The single-particle WF's derived from the HF calculations within the cubic WS cell are determined with the meshsize 1 fm [GM07], and the deviation in the calculated energy spectrum may achieve 10%.
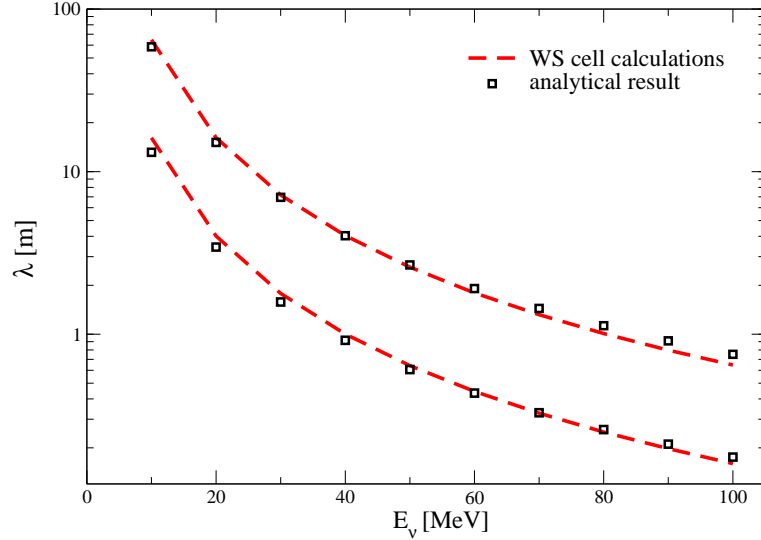
Figure 5.1: Neutrino mean free path of free Fermi gas. Results of WS cell calculations (dashed lines) are compared with analytical result (dots) from Appendix A. The upper curve corresponds the density $\rho = 0.01$ fm^{-3}, and the lower curve for $\rho = 0.02$ fm^{-3}.

The Hartree-Fock calculations are performed at the temperature $T = 1$ MeV. This temperature is relatively low to connect our calculations of the mean free path with a certain astrophysical scenario, e.g., the cooling of NS. However, the main goal of our work is to investigate the difference of NMFPs in the pasta and homogeneous matter due to the different spatial density distributions. This difference will be largest at low temperature as at higher temperatures the inhomogeneous mass distributions tend to disappear. Therefore, the low temperature considered here determines the maximal effect of the spatial density distribution on the mean free path. For higher temperatures this influence becomes weaker and vanishes at the melting temperature, which is around $T = 15$ MeV.

Comparing the spectra of single-particle energies obtained for the homogeneous and inhomogeneous solutions, one observes that the single-particle energies for the localized states in inhomogeneous matter show more negative energies than the lowest single-particle states for the homogeneous approach. This effect was already discussed in Chapter 4. In the β-equilibrium, all proton states are localized and
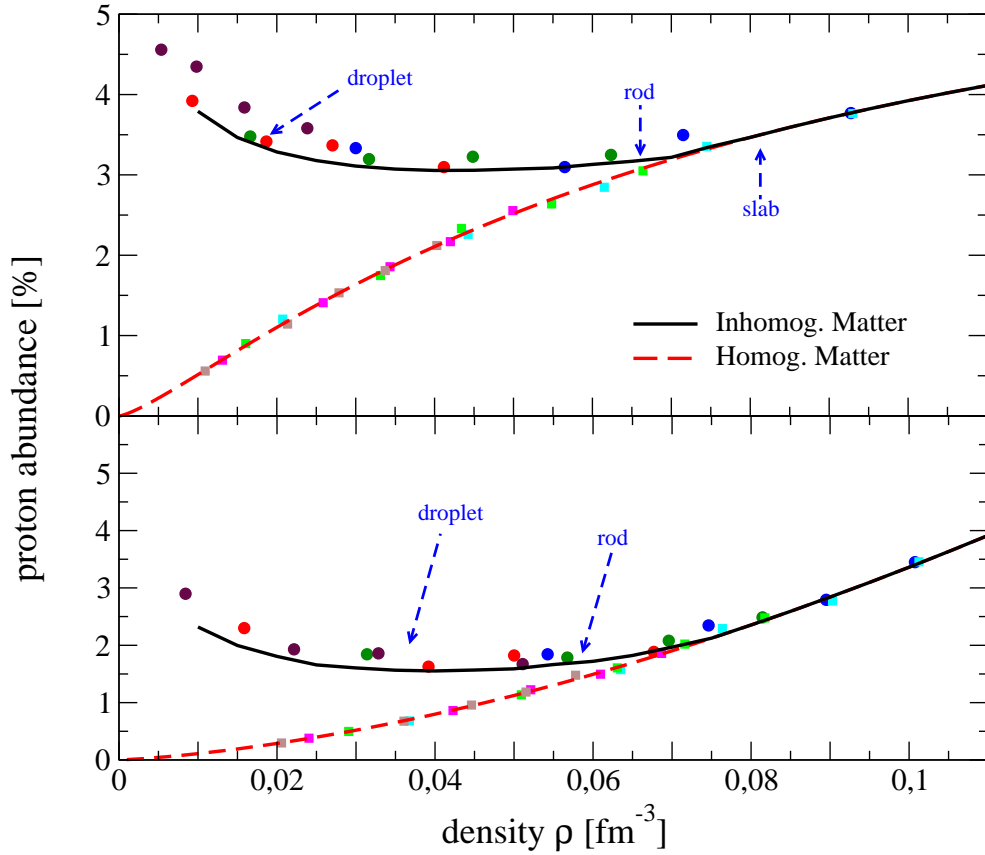
Figure 5.2: Proton abundance in the case of uniform matter (dashed line) and pasta phase (solid line). The symbols refer to specific calculations, whereas the lines have been added to guide the eye. The results for Skyrme-Hartree-Fock calculations are shown in the upper panel and the relativistic mean-field results in the lower one. The dashed arrows indicate typical densities leading to pasta structures of droplet, rod and slab shape.

therefore tend to have more attractive single-particle energies in the inhomogeneous as compared to the homogeneous density calculation. The variational calculations allowing for pasta structure yield larger proton fractions than obtained for the β-equilibrium of homogeneous matter at the same global density.

This can be seen from inspecting Fig.5.2. The upper panel of this figure contains results of the proton abundances for baryonic matter in β-equilibrium that resulted from non-relativistic Skyrme Hartree-Fock calculations. The proton abundance of homogeneous matter is a monotonically increasing function of total density and it reaches the value of 4% at the density of 0.1 fm^{-3}. Allowing for inhomogeneous matter distribution, one obtains a significant increase of the proton fraction at densities below 0.03 fm^{-3}, while in the density region from 0.03 to 0.08 fm^{-3} its value is almost constant around 3.2%. The lower panel of Fig.5.2 displays the corresponding results derived from the relativistic mean field approach. This relativistic approach seems to provide a smaller symmetry energy at these low densities, which leads to smaller proton abundances in the inhomogeneous as well as the homogeneous solution.

In Fig.5.3 we intend to demonstrate the dependence of the neutrino cross section for the charge current reaction on the spatial orientation of the momentum transfer $\boldsymbol{q}$. This is displayed in terms of the corresponding neutrino mean free path, which has been calculated according to (5.8) from σ_x (solid line) and σ_z (dashed line), respectively. Note that due to our choice of the coordinate system, the results for σ_y are identical to those for σ_x for the rod as well as the slab structures.

For the density ρ of 0.0625 fm^{-3}, which leads to a rod structure, we obtain results for the NMFP ranging from 20 km for neutrinos with an energy of 10 MeV down to 30 cm for neutrinos with an energy of 100 MeV. For low-energy neutrinos, the NMFP for reactions with a momentum transfer parallel to the x-axis is larger by a factor of 2 as compared to a momentum transfer parallel to the z-axis, a difference which disappears for neutrinos with larger energies. This factor of 2 is non-negligible but small on the scale of variations for the NMFP as a function of the neutrino energy. Therefore, the simple averaging procedure of Eq.(5.7) seems to be adequate.

Similar results are obtained for the slab configuration as can be seen from the lower panel of Fig.5.3. Note that the results for the NMFP are considerably smaller at low neutrino energies (by a factor of 10) and even at neutrino energies as large as 100 MeV smaller by a factor 2, although the ratio of the inverse densities is only
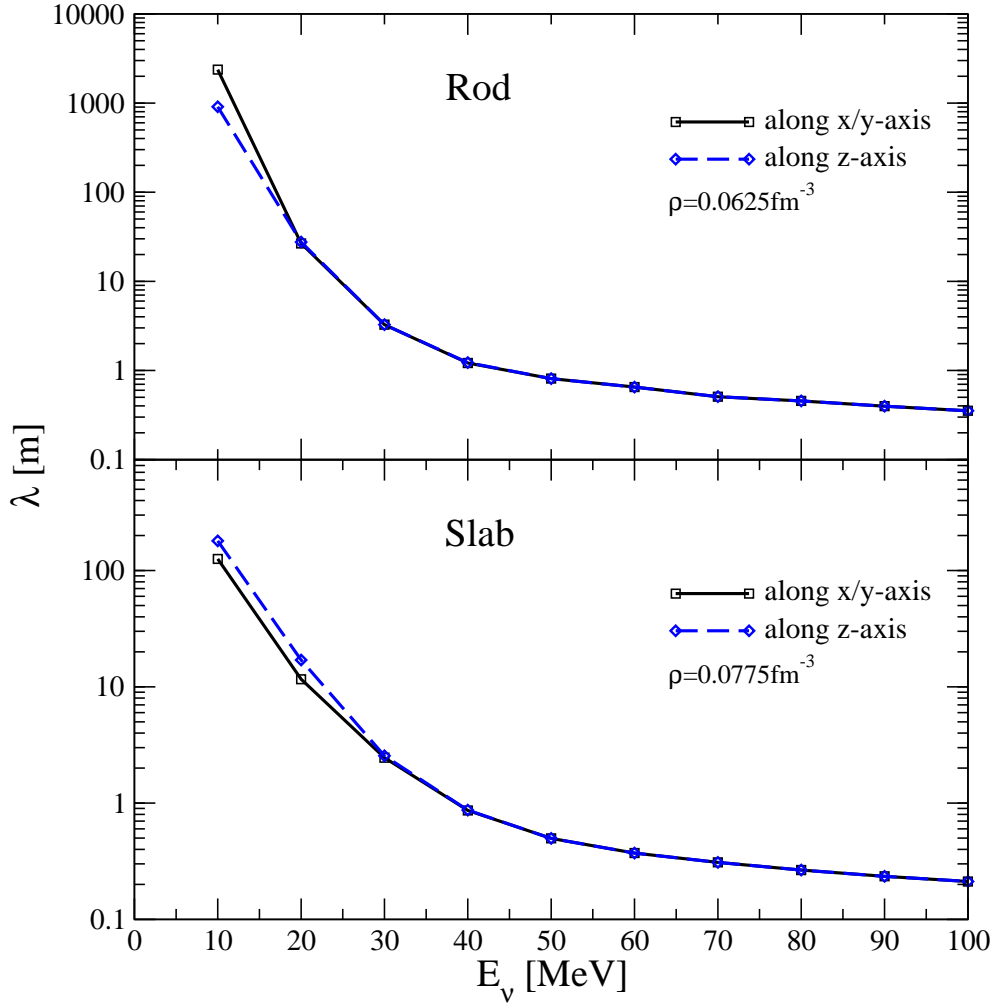
Figure 5.3: The neutrino mean free path (NMFP) calculated for the charged current reaction in case of rod and slab configurations demonstrate the dependence of the result on spatial orientation of the momentum transfer $\boldsymbol{q}$. For these calculations we have employed results of the Skyrme HF approach and ignored the blocking of final electron states.

about 1.2.

The NMFP calculated in CC (left panel) and NC (middle panel) reactions for homogeneous and inhomogeneous matter distributions are shown in Fig.5.4. First, let us compare the NMFP of homogeneous matter for both types of reactions. The main influence on NMFPs results from the available phase space for each reaction. In fact, the proton fraction of homogeneous matter does not exceed 1% for the densities considered here. Thus we have to consider a much larger blocking effect for the neutrons in the final states NC reactions than for the protons in the CC reactions. Therefore, the cross section of CC absorption is larger than in NC scattering, and consequently, the mean free path is shorter, as it is shown by the red dashed lines in Fig.5.4. Due to the small proton abundances in homogeneous matter, the Pauli blocking factor of final electron states affects the result for the CC reaction only at very small neutrino energies $E_\nu < 10$ MeV.

Fig.5.4 also presents results for the NMFP of inhomogeneous matter for both types of currents (left and middle panels). First of all, we should emphasize the larger influence of electron blocking factor on CC current reaction in the droplet phase. This is due to the larger proton abundances in the β-equilibrium of the inhomogeneous matter. At a neutrino energy around $E_\nu \simeq 10$MeV, the mean free path of CC processes is longer in comparison with NC scattering, because in this region the Pauli blocking of electrons in CC reaction dominates over the differences in phase spaces of the baryonic states. If the energy of incoming neutrino E_ν rises, the Pauli blocking drops exponentially and the ratio of the cross sections for CC and NC reactions is determined by the available phase space for the baryonic states as discussed above for the homogeneous matter calculation. This means that the NMFP of absorption due to CC becomes shorter than the respective result in NC scattering. At higher densities, where rods and slabs appear, the influence of Pauli blocking of electrons is partially compensated by the effects of the baryonic phase space. Therefore, the NMFP of CC reaction remains shorter in comparison with NC reaction for all neutrinos with $10 \leq E_\nu \leq 100$.

The same features are also observed in the comparison of NMFP due to the different currents for the models of inhomogeneous baryonic matter, which are based on the relativistic mean field calculations displayed in Fig.5.6.

The cross section for neutrino scattering in homogeneous matter increases with the
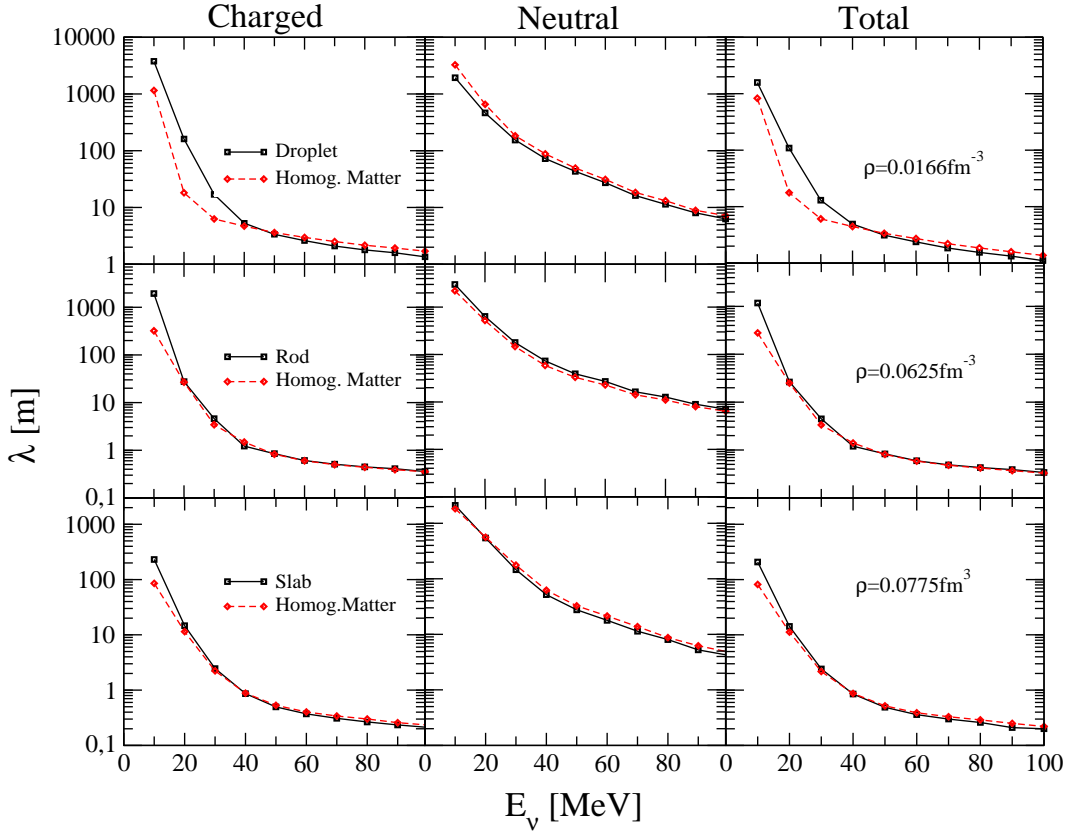
Figure 5.4: Skyrme-Hartree-Fock calculations of NMFP for pasta phases (solid curves) and the respective results for homogeneous matter at the same global density (dashed curves). The results for the charged current reaction are shown in the left column, the neutral current NMFP in the middle, and the total NMFP is shown in the right panel.

baryonic density in a non-linear way (see the discussion above). Therefore, one may expect that the mean free path in the inhomogeneous matter is shorter than the corresponding one for homogeneous of the same global density, since the scattering on the quasi-nuclear structures shall enhance the respective cross section. Nevertheless, the NMFP obtained for the charged current reaction, shown in the left column of Fig.5.4, demonstrates the opposite behaviour, specially at low densities, where the droplet phase occurs. The NMFP obtained from absorption in inhomogeneous matter is longer than the respective result derived from homogeneous matter calculations.

To explain this effect the difference in proton fractions of homogeneous and inho-

mogeneous matter discussed in the beginning of this Section is to be considered. At a typical density of 0.0165 fm^{-3} where the droplet phase occurs, the proton abundance in inhomogeneous matter is significantly larger than the respective value obtained in the homogeneous matter. This difference in the proton fractions has two effects. First, the homogeneous matter contains less protons in comparison with the inhomogeneous one. Consequently, the number of unoccupied final proton states is larger and more transitions, contributing to the total cross section, are possible. Second, the chemical potential of electrons compensating the charge of the protons in matter is lower in case of homogeneous matter and the respective Pauli blocking factor for the produced electrons is lower than those obtained for the inhomogeneous matter. This effect again modifies the cross section considerably at low E_ν. With the increase of energy of incoming neutrinos, the Pauli blocking of electrons rapidly drops and more transitions become possible, so that the differences between homogeneous and inhomogeneous matter distributions are getting less significant and the respective NMFPs become closer one to another. At higher densities of matter, where the rod and slab phases occur, the difference in proton abundances are less important; therefore, the resulted mean free paths are very similar and the effect of inhomogeneous structure becomes negligible.

At the end we should note that at neutrino energies less than 10 MeV, the NMFPs of homogeneous and inhomogeneous matter distributions calculated in CC reaction significantly exceed the typical neutron star radius. Therefore, one can conclude that the charged current reaction is kinematically suppressed [Bo81].

The results of neutral current reaction are shown on the middle panel of Fig.5.4. It is obvious that the appearance of pasta phase in this case has no important influence on neutrino propagation, since this type of reaction does not depend on Pauli blocking of neutrino in final state (no trapped neutrinos). The only small difference in NMFPs of homogeneous matter and droplet phase may be explained by different values of matrix elements in (5.6), since the single-particle wave functions of bound neutrons in droplet significantly differ from wave functions of homogeneous matter. However, even this small effect becomes negligible if the global density increases the density profiles become smoother and transition to the homogeneous phase approaches.

The total NMFP, which combines both reactions, is shown on the right panel. It can be seen that the total mean free path is slightly shorter than the mean free path
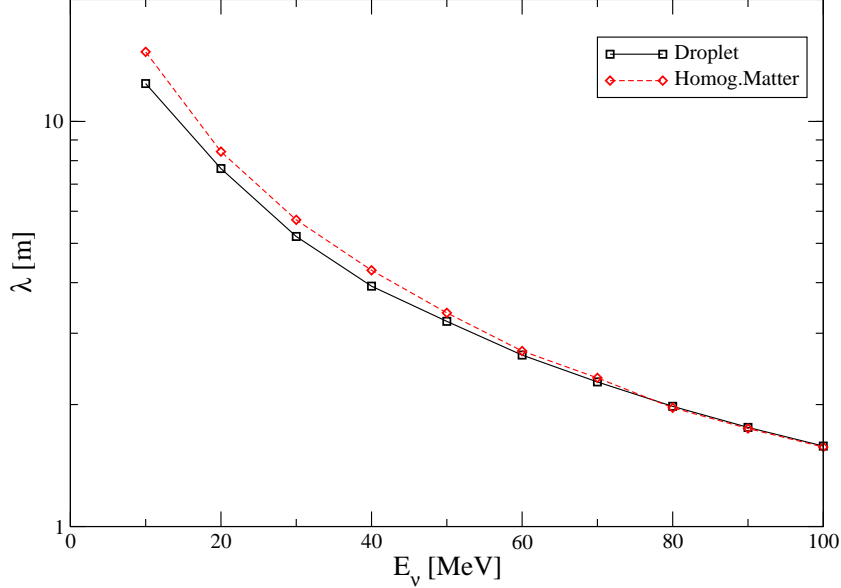
Figure 5.5: Skyrme-Hartree-Fock calculations of NMFP for droplet phase (solid curve) and the respective results for homogeneous matter (dashed curve) at the same global density ρ =0.0166fm^{-3}. The effects of electron blocking factor and β-equilibrium were ignored.

in charged current reaction. Therefore, we conclude that this reaction is dominant in the total neutrino response of the system.

Up to now we considered the nuclear matter in β-equilibrium and found that the main role in NMFP of charged current reaction is played by the electron blocking factor and the difference in phase spaces, caused by different proton numbers in the pasta phase and homogeneous matter at the same global density. Therefore, all effects due to different spatial distribution were hidden. To investigate the influence of density distributions on NMFP the calculations in homogeneous and inhomogeneous matter with the same proton fraction can be performed. For comparison we choose the non-relativistic droplet phase and homogeneous matter at the same density with fixed proton fraction 3.5%, ignoring the electron blocking factor. The results are shown in Fig.5.5. The mean free path is shorter for inhomogeneous density distributions; however, the difference between two curves is only about 20% at the neutrino energy E_ν =10 MeV. Since the core of droplet phase, localed at the

center of WS cell originated from the deeply bound states[1], its contribution becomes less significant with the increase of energy E_ν. In fact, when energy and momentum transfers rise, the contribution of deeply bound states becomes less important and in contrast the contribution of transitions between weakly bound and free states of neutrons and protons increases.

5.3   The Relativistic Mean-Field Model

To test the sensitivity of the results on the underlying nuclear model and the choice of the NN interaction, we also investigated the NMFP in the inhomogeneous nuclear matter evaluated within a relativistic mean-field (Hartree) approximation by using a model of density-dependent meson-nucleon coupling constants. The parameterization of these constants has been fitted to reproduce the properties of the nucleon self-energy evaluated in Dirac-Brueckner-Hartree-Fock (DBHF) calculations of asymmetric nuclear matter but has also been adjusted to provide a good description for bulk properties of finite nuclei [Kl$^+$06, VFF07, SM01, HKL01]. The density-dependent relativistic mean-field (DDRMF) approach has also been used to describe the properties of inhomogeneous nuclear matter in the crust of neutron stars [GV$^+$08].

The density-dependent relativistic mean-field approach is an effective field theory of interacting mesons and nucleons. Following the usual notation, we consider scalar (σ, δ) and vector mesons (ω, ρ), which with respect to the isospin correspond to isoscalar (σ, ω) and isovector (δ, ρ), respectively. The Lagrangian density consists of three parts: the free baryon Lagrangian density $\mathcal{L}_B$, the free meson Lagrangian density $\mathcal{L}_M$ and the interaction Lagrangian density $\mathcal{L}_{\text{int}}$:

$$\mathcal{L} = \mathcal{L}_B + \mathcal{L}_M + \mathcal{L}_{\text{int}}, \tag{5.9}$$

---

[1]See the discussion concerning the deeply bound neutrons in the previous Chapter.

κ	J^P	I	m [MeV]	a_κ	b_κ	c_κ	d_κ
σ	0^+	0	550	7.7868	2.58637	2.32431	3.11504
ω	1^-	0	782.6	9.73684	2.26377	7.05897	-
δ	0^+	1	983	2.68849	6.7193	0.503759	0.403927
ρ	1^-	1	769	4.56919	5.45085	1.20926	-

Table 5.1: Parameter set from DBHF by van Dalen et al. [VFF07] for the density dependent relativistic mean field approach.

which take the explicit form

$$\mathcal{L}_B = \bar{\Psi}(\,i\gamma_\mu\partial^\mu - M)\Psi,$$

$$\mathcal{L}_M = \tfrac{1}{2} \sum_{\iota=\sigma,\delta} \left(\partial_\mu\Phi_\iota\partial^\mu\Phi_\iota - m_\iota^2\Phi_\iota^2 \right)$$

$$- \tfrac{1}{2} \sum_{\kappa=\omega,\rho,\gamma} \left(\tfrac{1}{2}F_{(\kappa)\mu\nu}\,F_{(\kappa)}^{\mu\nu} - m_\kappa^2 A_{(\kappa)\mu}A_{(\kappa)}^\mu \right),$$

$$\mathcal{L}_{\text{int}} = - g_\sigma\bar{\Psi}\Phi_\sigma\Psi - g_\delta\bar{\Psi}\boldsymbol{\tau}\boldsymbol{\Phi}_\delta\Psi$$

$$- g_\omega\bar{\Psi}\gamma_\mu A_{(\omega)}^\mu\Psi - g_\rho\bar{\Psi}\boldsymbol{\tau}\gamma_\mu\boldsymbol{A}_{(\rho)}^\mu\Psi$$

$$- e\bar{\Psi}\gamma_\mu\tfrac{1}{2}(1+\tau_3)A_{(\gamma)}^\mu\Psi,$$

$$(5.10)$$

with the field strength tensor $F_{(\kappa)\mu\nu} = \partial_\mu A_{(\kappa)\nu} - \partial_\nu A_{(\kappa)\mu}$ for the vector mesons. In the above Lagrangian density, the nucleon field consisting of Dirac-spinors in isospin space is denoted by Ψ and the nucleon rest mass by $M = 938.9$ MeV. The scalar meson fields are Φ_σ and $\boldsymbol{\Phi}_\delta$, the vector meson fields $A_{(\omega)}$ and $\boldsymbol{A}_{(\rho)}$. Bold symbols denote vectors in the isospin space acting between the two species of nucleons. The mesons have rest masses m_κ for each meson κ and couple to the nucleons with the strength of the coupling constants g_κ, which depend on a density of the nucleon field Ψ. This density dependence of the coupling constants was parametrized by

$$g_\kappa(\rho_B) = a_\kappa + \left[b_\kappa + d_\kappa x^3 \right] \exp(-c_\kappa x), \qquad (5.11)$$

where $x = \rho_B/\rho_0$ and $\rho_0 = 0.16$ fm^{-3} is the saturation density of symmetric nuclear matter. The values obtained for the fit of the coupling functions are summarized in Table 5.1.

Applying the variational principle to the Lagrangian we obtain a Dirac equation for the nucleons and Klein-Gordon and Proca equations for the meson fields. Due to

density-dependent vertices, the variation principle changes to

$$\frac{\delta \mathcal{L}}{\delta \bar{\Psi}} = \frac{\partial \mathcal{L}}{\partial \bar{\Psi}} + \frac{\partial \mathcal{L}}{\partial \rho} \frac{\delta \rho}{\delta \bar{\Psi}}, \tag{5.12}$$

where the second expression creates the so-called rearrangement contribution Σ_R to the self-energies of the nucleon field. These rearrangement contributions contribute only to the zero component of the vector self-energy. Including these additional contributions, we denote the Dirac equation for the nucleonic single-particle wave function ψ_α in the Hartree approximation

$$\big(\boldsymbol{\alpha}\boldsymbol{p} + (\Sigma_0 + \Sigma_R) + \beta(M + \Sigma_S)\big)\,\psi_\alpha = \epsilon_\alpha\,\psi_\alpha, \tag{5.13}$$

where the self-energy contributions read

$$\Sigma_S = g_\sigma \Phi_\sigma + g_\delta \Phi_\delta \tau_3,$$
$$\Sigma_0 = g_\omega A_0^{(\omega)} + g_\rho A_0^{(\rho)} \tau_3 + e \frac{1}{2}(1 - \tau_3) A_0^{(\gamma)}, \tag{5.14}$$

and the rearrangement self-energy contribution Σ_R is obtained by

$$\Sigma_R = \Big(\frac{\partial g_\sigma}{\partial \rho}\Phi_\sigma \rho^s + \frac{\partial g_\delta}{\partial \rho}\boldsymbol{\Phi}_\delta \rho_3^s + \frac{\partial g_\omega}{\partial \rho}\gamma_\mu A_0^{(\omega)}\rho + \frac{\partial g_\rho}{\partial \rho}\boldsymbol{A}_0^{(\rho)}\rho_3\Big). \tag{5.15}$$

The various densities are obtained from the nucleon single-particle wave functions in the "no-sea" approximation as

$$
\begin{aligned}
\rho^s(\boldsymbol{x}) &= \sum_\alpha \eta_\alpha\, \bar{\psi}_\alpha(\boldsymbol{x})\psi_\alpha(\boldsymbol{x}) \\
\rho_3^s(\boldsymbol{x}) &= \sum_\alpha \eta_\alpha\, \bar{\psi}_\alpha(\boldsymbol{x})\tau_3\psi_\alpha(\boldsymbol{x}) \\
\rho(\boldsymbol{x}) &= \sum_\alpha \eta_\alpha\, \bar{\psi}_\alpha(\boldsymbol{x})\gamma_0\psi_\alpha(\boldsymbol{x}) \\
\rho_3(\boldsymbol{x}) &= \sum_\alpha \eta_\alpha\, \bar{\psi}_\alpha(\boldsymbol{x})\gamma_0\tau_3\psi_\alpha(\boldsymbol{x}) \\
\rho^{(em)}(\boldsymbol{x}) &= \sum_\alpha \eta_\alpha\, \bar{\psi}_\alpha(\boldsymbol{x})\tfrac{1}{2}(1 - \tau_3)\psi_\alpha(\boldsymbol{x})\ \ [-\rho_e(\boldsymbol{x})].
\end{aligned} \tag{5.16}
$$

where ρ^s is the scalar density, ρ the baryon density, ρ_3^s the scalar isovector density, ρ_3 the vector isovector density, and $\rho^{(em)}$ the charge density. The occupation factors η_α have to be determined from the desired scheme of occupation.

Neglecting retardation effects, the Klein-Gordon equations reduce to inhomogeneous Helmholtz equations with source terms

$$
\begin{aligned}
\left(-\Delta + m_\sigma^2\right)\Phi_\sigma &= -g_\sigma\,\rho^s \\
\left(-\Delta + m_\delta^2\right)\Phi_\delta &= -g_\delta\,\rho_3^s \\
\left(-\Delta + m_\omega^2\right)A_0^{(\omega)} &= g_\omega\,\rho \\
\left(-\Delta + m_\rho^2\right)A_0^{(\rho)} &= g_\rho\,\rho_3 \\
-\Delta\,A_0^{(\gamma)} &= e\,\rho^{(em)},
\end{aligned}
\tag{5.17}
$$

from which the self-energy contributions (5.14) are obtained. The Dirac equation for the nucleons (5.13), the evaluation of the resulting densities (5.16), these meson field equations (5.17) and the calculation of the resulting self-energy contributions (5.14) form a set of equations, which have to be solved in a self-consistent way.

For the description of nuclear matter in a Wigner-Seitz cell, the Dirac equation (5.13) and the meson field equations (5.17) are solved in spatial representation. The numerical procedure to solve the Dirac equation in the cubic box is the same as that for the non-relativistic Skyrme Hartree-Fock approach described above. Pairing correlations are included in terms of the BCS approximation assuming a density-dependent zero-range pairing force [MMM04].

The resulting single-particle energies and spinors were used in the calculation of NMFP as described in the next Section.

5.4 Mean Free Path in Relativistic Model

First, let us consider the charged current reaction. Here we will exploit the most general form for the nucleonic current, which is allowed due to the Lorentz, parity and isospin invariances [SL]:

$$
J_\mu^{CC} = i\bar\psi_p[F_1^v(q^2)\gamma_\mu + F_2^v(q^2)\sigma_{\mu\nu}q_\nu + F_A(q^2)\gamma_5\gamma_\mu - iF_p(q^2)\gamma_5 q_\mu]\psi_n,
\tag{5.18}
$$

where F_1^v and F_2^v are isovector electromagnetic formfactors, F_A is the axial-vector formfactor, F_p is the induced pseudoscalar formfactor. Following the common practice, we ignore the contribution of the second-class currents. The leptonic current has the same structure as in (5.3). Analogously to (5.1) and (5.5), the averaged

squared matrix element for the charged current reaction can be written in the form

$$
\begin{aligned}
\overline{|M|}^{\,2} \;=\; & \frac{G_F^2 C^2}{2} [\; |\mathcal{M}_1|^2 (1 - \frac{p_l}{3E_l}\cos\vartheta) + |\mathcal{M}_2|^2 (1 + \frac{p_l}{E_l}\cos\vartheta) \qquad (5.19) \\
& + |\mathcal{M}_3|^2 (p_l^2 + E_\nu^2 - 2p_l E_\nu \cos\vartheta - \frac{p_l^3}{3E_l}\cos\vartheta - \frac{p_l}{3E_l}E_\nu^2\cos\vartheta + \frac{2p_l^2}{3E_l}E_\nu) \\
& + |\mathcal{M}_4|^2 \frac{p_l}{E_l} ((p_l^2 + E_\nu^2)\cos\vartheta - 2E_l E_\nu \cos\vartheta + p_l E_l + \frac{E_l}{p_l}E_\nu^2 - 2p_l E_\nu)],
\end{aligned}
$$

where

$$
\begin{aligned}
\mathcal{M}_1 \;=\;& F_1 \bar{\psi}_p \boldsymbol{\gamma} \psi_n + F_A \bar{\psi}_p \gamma_5 \boldsymbol{\gamma} \psi_n, \\
\mathcal{M}_2 \;=\;& F_1 \bar{\psi}_p \gamma_0 \psi_n + F_A \bar{\psi}_p \gamma_5 \gamma_0 \psi_n - i F_p \bar{\psi}_p \gamma_5 q_0 \psi_n, \\
\mathcal{M}_3 \;=\;& F_2 \bar{\psi}_p \boldsymbol{\Sigma} \psi_n, \\
\mathcal{M}_4 \;=\;& F_p \bar{\psi}_p \gamma_5 \psi_n,
\end{aligned}
$$

and

$$
\boldsymbol{\Sigma} = \begin{pmatrix} \boldsymbol{\sigma} & 0 \\ 0 & \boldsymbol{\sigma} \end{pmatrix}.
$$

Dirac spinors ψ and the respective single-particle energies are obtained from the solution of the Dirac equation [GV+08].

The hadronic part of the neutral current involves additionally isoscalar electromagnetic formfactors F_1^s and F_2^s, so that

$$
\begin{aligned}
J_\mu^{NC} \;=\;& \frac{i}{2}\bar{\psi}_n [F_A(q^2)\gamma_5\gamma_\mu - iF_p(q^2)\gamma_5 q_\mu \qquad\qquad (5.20) \\
& + (1 - 2\sin^2\theta_W)(F_1^v(q^2)\gamma_\mu + F_2^v(q^2)\sigma_{\mu\nu}q_\nu) \\
& - 2sin^2\theta_W (F_1^s(q^2)\gamma_\mu + F_2^s(q^2)\sigma_{\mu\nu}q_\nu)]\psi_n,
\end{aligned}
$$

where θ_W is the Weinberg angle. The respective matrix element for this reaction looks like

$$
\begin{aligned}
\overline{|M|}^{\,2} = \quad & \frac{G_F^2}{8}[\; |\mathcal{N}_1|^2 (1 - \tfrac{1}{3}\cos\vartheta) + |\mathcal{N}_2|^2 (1 + \cos\vartheta) \qquad (5.21) \\
& + |\mathcal{N}_3|^2 (E_\nu'^2 + E_\nu^2 - 2E_\nu E_\nu' \cos\vartheta - \tfrac{1}{3}E_\nu'^2\cos\vartheta - \tfrac{1}{3}E_\nu^2\cos\vartheta + \tfrac{2}{3}E_\nu E_\nu'^2) \\
& + |\mathcal{N}_4|^2 (E_\nu - E_\nu')^2 (1 + \cos\vartheta)],
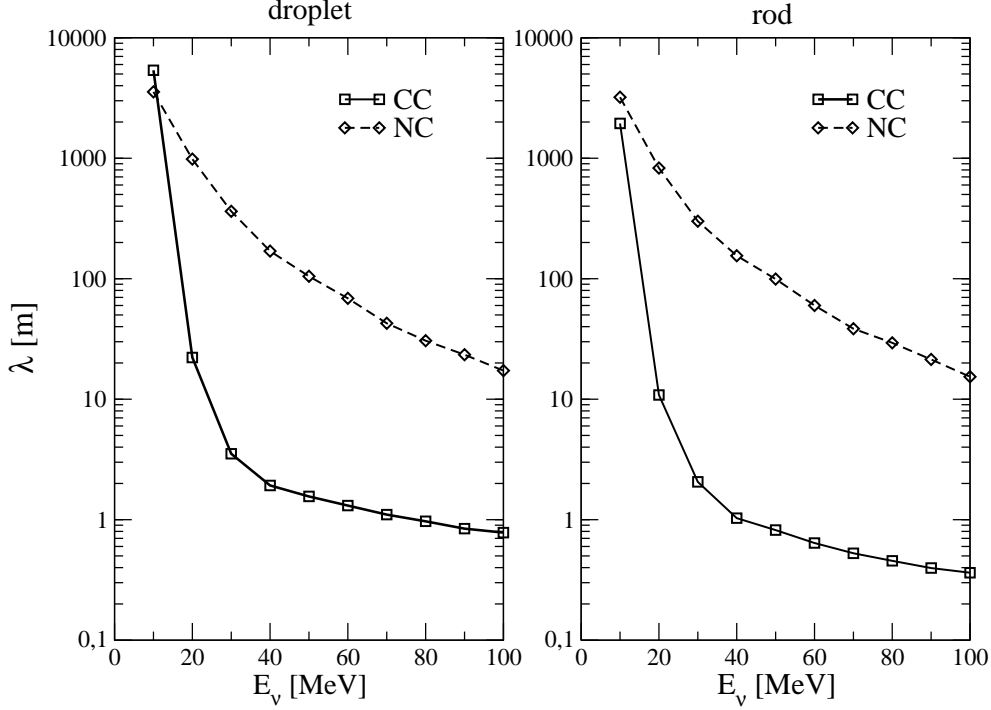\end{aligned}
$$

Figure 5.6: Results of NMFP due to NC (dashed lines) and CC (solid lines) reactions. The description of the inhomogeneous baryonic matter distributions results from the density dependent relativistic mean-field calculations. As examples we present results for the droplet phase displayed in the left panel at a density of 0.034 fm^{-3} and for the rod phase (right panel) at 0.055 fm^{-3}.

where

$$
\begin{aligned}
\mathcal{N}_1 &= ((1 - 2\sin^2\theta_W)F_1^v - 2\sin^2\theta_W F_1^s)\bar{\psi}_n\boldsymbol{\gamma}\psi_n + F_A\bar{\psi}_n\gamma_5\boldsymbol{\gamma}\psi_n, \\
\mathcal{N}_2 &= -F_A\bar{\psi}_n\gamma_5\gamma_0\psi_n - ((1 - 2\sin^2\theta_W)F_1^v - 2\sin^2\theta_W F_1^s)\bar{\psi}_n\psi_n + iF_P\bar{\psi}_n\gamma_5\psi_n, \\
\mathcal{N}_3 &= ((1 - 2\sin^2\theta_W)F_2^v - 2\sin^2\theta_W F_2^s)\bar{\psi}_n\boldsymbol{\Sigma}\psi_n, \\
\mathcal{N}_4 &= F_p\bar{\psi}_n\gamma_5\psi_n.
\end{aligned}
$$

Substituting (5.19) and (5.21) in (5.4), one obtains the mean free path of neutrinos in relativistic mean-field model for charged and neutral current reactions, respectively. A comparison of NMFPs of charged and neutral currents in case of pasta phase based on a relativistic mean-field model in a WS cell is displayed in Fig.5.6. It is worth

mentioning that within the relativistic model we could not find any formation of slab structures. Therefore, only results for droplet and rod structures are shown. Also the global density at which the droplet phase occurs in the relativistic mean-field model is two times larger than the respective density in the nonrelativistic model. The difference between proton fractions of homogeneous matter and pasta phase is not so significant. In fact, the values of proton abundance around $\rho = 0.02$ fm^{-3}, displayed in the lower panel of Fig.5.2, are about 40% smaller than the corresponding values obtained in the Skyrme model (the upper panel). Therefore, we omit the comparison between NMFPs of homogeneous and inhomogeneous matter; however, we compare the mean free paths of pasta phase for both types of reactions. One can see that at $E_\nu < 20$MeV, the behavior of CC curves is determined by the Pauli blocking, while at higher energies the result becomes sensitive to the structure of phase space available for the reactions. Both charged and neutral current mean free paths decrease if the global density of matter rises.

Summarizing we conclude that the NMFP is determined by three different factors. The first of them – the Pauli blocking effect of final electrons in CC reaction – plays the most important role at low neutrino energy and drops exponentially if the energy increases. The second factor is the difference in baryonic phase spaces of different reactions. The phase space of CC absorption is larger than in NC scattering, because the Fermi energy of final (proton) states is considerably lower than the neutron Fermi energy. The last factor, related to a significant difference of the spatial density distributions, leads to the reduction of the NMFP in inhomogeneous matter; however, it plays a smaller role in comparison with other effects.

Chapter 6

Low-momentum NN Interaction

Many approaches have been developed to predict the properties of nuclear matter under extreme conditions. Some of them are based on the phenomenological models which successfully describe the ground state properties of stable nuclei. Along this line the non-relativistic density-dependent Skyrme model has been constructed [Sk59], [VB72], [NV72], [SP07]. There exist more than 87 different Skyrme parameterizations, adjusted to fit the bulk properties of finite nuclei and nuclear matter. However only 27 of them give the satisfactory neutron star models [SM$^+$03]. This emphasizes a large sensitivity of the effective theories on the phenomenological input they are based on. The relativistic mean-field (RMF) approaches use the effective interaction represented by a Lagrangian density, dependent on a set of the coupling constants (sometimes density-dependent [GV$^+$08]), which is fitted to the saturation properties of nuclear matter and ground state of finite nuclei [Gl00]. However the validity of this approach in the high density regime raises doubts, since the meson fields used in RMF theory may be not that reliable in the density region $1\rho_0 \leq \rho \leq 5\rho_0$ [AP$^+$98].

The nuclear matter calculations based on the realistic models of NN interaction allow us to test the predictions of phenomenological models. In this Chapter we outline a method, allowing to incorporate the realistic NN interaction in many-body Hartree-Fock calculations.
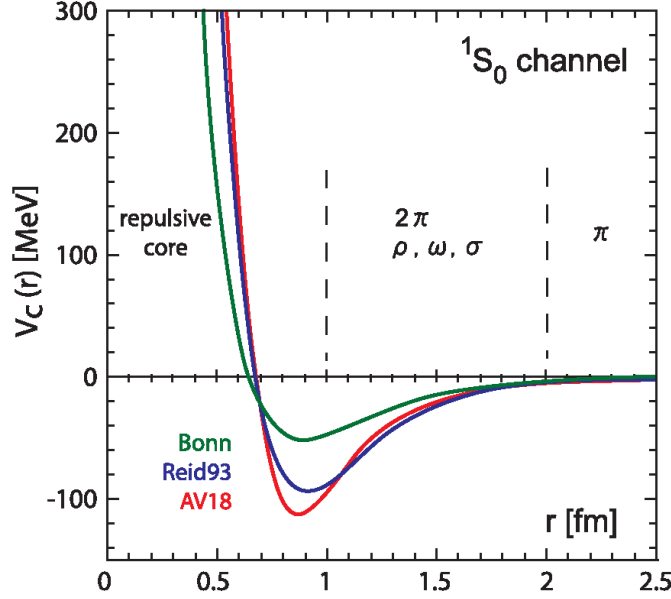
Figure 6.1: The $^1S_0$ channel of various realistic forces in the coordinate representation. Taken from Ref. [AHI08].

6.1 Historical Overview

The theoretical description of finite nuclei and nuclear matter applying a microscopic theory is a major challenge of nuclear physics. It is assumed that the NN interaction is based on the available free-space data, *viz.*, the elastic nucleon-nucleon and neutron-deuteron scattering phase shifts. Then the theoretical predictions can be obtained from the many-body calculations, developed for strongly interacting systems.

At low densities and energies the nucleons are mostly treated as non-relativistic point-like fermions. A proper derivation of the nucleon-nucleon interaction from the first principles remains obscure, since the fundamental theory of strong interaction, QCD, is non-perturbative in the energy regime characteristic for the low-energy nuclear physics. Therefore the many-body calculations are commonly based on the phenomenological meson-exchange models for the two-nucleon force[1]. The three- (or even four-) body forces must be introduced to enhance the capability of such models and to obtain accurate results for few-body systems.

---

[1]In the literature such a NN interaction is often referred to as "residual" QCD strong interaction.

As is well known, there are several high precision models of the nucleon-nucleon interaction V_{NN}, which we will refer to as the "realistic" interactions. In these models the long-range part of interaction, corresponding to the inter-nucleon distances of the order 2 fm$\sim 1/m_\pi$, is described by the model-independent one-pion exchange (OPE) [Yu35]. However the intermediate-range attraction $\sim 1/(2m_\pi)$ and the short-range repulsion are treated by using different phenomenological form factors. In Fig.6.1 some of the realistic forces are shown in the coordinate representation. One can see that these models, being significantly different at short distances, possess however the same long-range parts. In the following we outline the most popular realistic interactions:

• The Bonn potentials [MHE87] use the multiple one-boson exchange interactions and the two-pion exchange potential calculated in perturbation theory. The two-pion exchange is then approximated by an energy-independent σ-meson exchange term. At short distances the potential is regularized by the form factors. The CD-Bonn potential [MSS96], [Mac01] considers in addition the non-local contributions from the covariant amplitudes.

• The local Argonne potential consists of the one-pion exchange regularized at short distances, and a phenomenological parametrization at short and intermediate distances [WS$^+$95]. Starting from the distance $r \sim 0.5$ fm the core is controlled by the Woods-Saxon functions.

• The Nijmegen potentials [SK$^+$94] are based on the multiple one-boson exchange. The parameters of interaction depend on the partial waves. The exponential form factors regularize the potential at very short distances.

• The Paris potential includes the two-pion exchange using the dispersion-theory [LL$^+$80]. The local potential is described by several static Yukawa functions. The ω-meson exchange is included as a part of the three-pion exchange. The potential accounts for the repulsive core at distances about 0.8 fm. At very short distances an energy-dependent soft core is used.

Recently a great progress was achieved in deriving the low-energy NN interactions within the framework of the Effective Field Theory (EFT) [ORK94], [KSW98], [Pa$^+$98], [EGM00], [BB$^+$]. EFT is constructed below the chiral symmetry breaking scale $\Lambda_\chi \sim 1$GeV, where the appropriate degrees of freedom for nuclear systems are nucleons and pions. The other degrees of freedom such as higher mass mesons,
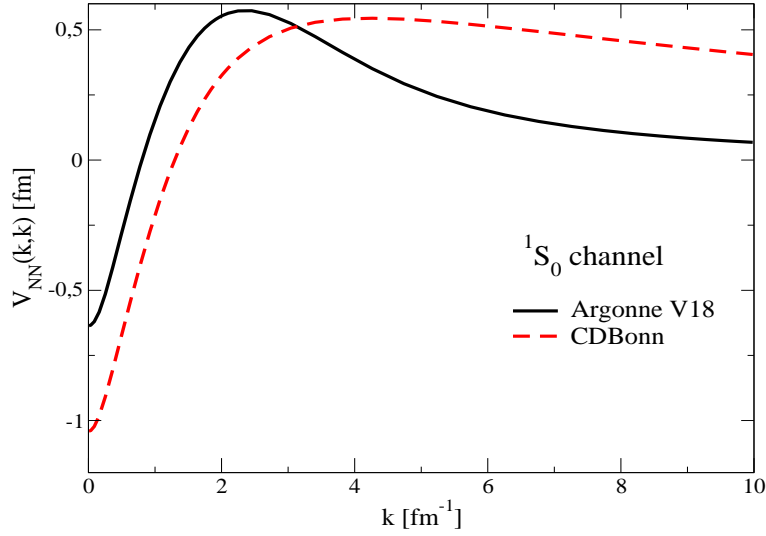
Figure 6.2: The diagonal matrix elements of the high precision potentials V_{NN} versus the relative momentum in $^1S_0$ partial wave channel.

nucleon resonances, antinucleons or other baryons are not relevant for low-energy physics and may be considered as to be integrated out of the theory. The pion-nucleon Lagrangian, constrained by the symmetries of QCD, contains all possible interactions consistent with the chiral symmetry. Along this line one obtains the chiral symmetric EFT, which is used to construct either perturbative or non-perturbative controlled approximations for the low-energy nuclear systems. The EFT thus provides a model-independent description of the two-body systems. However, the high precision description of NN scattering data provided by realistic models is at present not achieved by the rigorous EFT potentials.

• By using the EFT the Idaho potential was developed [EM01]. Unlike the rigorous EFT this potential is model-dependent, since it contains several terms, which must be omitted in the power-counting scheme. However they allow a better description of the scattering phase shifts.

All mentioned potentials are tuned to fit about 3000 data which constitute the database for NN scattering below the pion threshold $E_{lab} \simeq 350$MeV [2]. This energy corresponds to a cutoff parameter in momentum space $\Lambda_{data} \simeq 2$ fm^{-1}. Unfortu-

---

[2]Following Ref. [SK$^+$93] it is the uppermost energy for which the data would be included in NN database because of the pion-production threshold. At higher energies the NN collisions are no longer elastic.

nately the experimental data is not sufficient to resolve the short-range behaviour of the forces. Therefore the strong model-dependence of the high precision potentials is observed in the momentum-space matrix elements (see Fig.6.2), in spite of their common successful description of low-energy experimental data[3]. This leads to the conclusion that the low-energy physics is not sensitive to the parameterization of the short-range (high-momentum) part of NN interaction. This argument plays an important role in the theory of low-momentum effective NN interaction, the so-called $V_{\text{low-k}}$, discussed in this Chapter.

Apart from the unwanted model-dependence, the short-range repulsion prevents the use of realistic potentials in the lowest order many-body calculations based on the standard Hartree-Fock mean-field theory. This problem can be overcome by the Brueckner-Hartree-Fock approximation [Br54], [BL55], in which the model space is restricted to one Slater determinant and the initial realistic interaction gives the scattering G-matrix through the solution of the Bethe-Goldstone equation [Go57]. In this case the G-matrix may be interpreted as a kind of effective NN interaction. However, from a formal point of view, G-matrix is not the effective interaction, because it is energy-dependent and usually non-Hermitian (the G-matrix is Hermitian only for a constant starting energy) and it has no decoupling property between the model space and its complement [S82], [SO94].

Another promising way of solving the short-range problem consists in decoupling of the initial Hilbert space on two model spaces, by introducing the cutoff momentum Λ. In such a way one can separate the predictions of correlations at low and medium momenta, which are constrained by the NN scattering data below the pion threshold, from the high momentum components, which may strongly depend on the underlying model of the realistic interaction. After that the contribution of the high-momentum components (above Λ) can be integrated out. The effective interaction $V_{\text{low-k}}$, constructed in such a way, does not have momentum components larger than the cutoff. Thus it is considerably softer than the initial high-precision potential, and can be used in the standard Hartree-Fock calculations. Also it was found that for a cutoff parameter $\Lambda \simeq 2$ fm^{-1} the $V_{\text{low-k}}$ interaction becomes independent on the underlying realistic interaction (compare Fig.6.2 and Fig.6.3).

---

[3]The model dependence of high-momentum components may lead to an uncertainty in predictions of nuclear matter properties under extreme conditions we are interested in.
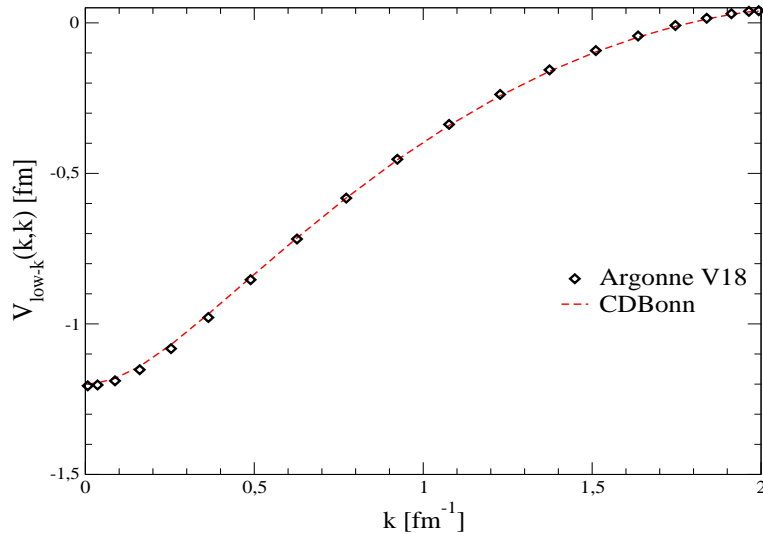
Figure 6.3: The diagonal matrix element of $V_{\text{low-k}}$ potential generated from Argonne V18 and CDBonn potentials in $^1S_0$ channel. One can observe that in momentum space both realistic interactions give the same $V_{\text{low-k}}$ force at the cutoff $\Lambda \simeq 2$ fm^{-1}.

There are two equivalent methods to construct the effective low-momentum interaction. One of them is based on the renormalization group (RG) treatment [BS+01], [BK+01], [BK+02], while the alternative method was proposed by Suzuki [S82] and Okamoto [SO94] on the basis of the unitary-model-operator-approach referred to shortly as UMOA, which is a natural extension of the model-space method by Lee-Suzuki [LS80], [SL80] and Okubo [O54]. The equivalence of the model-space methods to the RG equation is obvious, since both of them preserve the half-on-shell (HOS) T-matrix, the bound state poles, and the P-space projection of low-energy eigenstates [4]. Below we will briefly outline both methods.

6.2 The Renormalization Group Approach

The renormalization group approach to the nucleon-nucleon interaction was proposed by Bogner *et al.* [BK00]. It removes the short-distance model dependence of the bare potentials preserving their high accuracy in describing the nucleon-nucleon scattering data and deuteron binding energy. The fundamental principle of an up

---

[4]The equivalence of model space techniques and the renormalization group approach for a separable potential are considered in [BK00]. See also [BF+08].

to date effective theory is that low-momentum physics is not sensitive to the details of high-momentum one. Therefore an effective theory replacing the short-distance dynamics by effective interactions and preserving the low-momentum symmetries can be constructed.

Let us consider a quantum system with interaction V_{bare}. This contains the long-range part V_L, which is determined mainly by OPE potential and the short-range part V_H, which is poorly understood. In this case the total interaction can be separated as

$$V_{\text{bare}} = V_L + V_H. \tag{6.1}$$

The full Hamiltonian of the system can be written

$$H = H_0 + V_L + V_H, \tag{6.2}$$

where the operator H_0 denotes the one-body part of the two-body system and contains the kinetic energy of the interacting particles. The cutoff Λ can be imposed on the intermediate state energies and momenta. This cutoff decouples the low-energy states, which are important in low-energy physics, from the high-energy states. The potential V_H cannot be simply neglected since it has an effect on the low-momentum part and must be included as a correction term. These correction terms are determined by demanding that an effective Hamiltonian $H_{\text{low-k}}$ reproduces all the low-energy spectra and amplitudes in the low-momentum space (below the cutoff).

An arbitrary amplitude can be written in perturbation theory as

$$\langle f|\mathcal{A}|i\rangle = \langle f|V_{\text{bare}}|i\rangle + \sum_{n=0}^{\infty} \frac{\langle f|V_{\text{bare}}|n\rangle\langle n|V_{\text{bare}}|i\rangle}{E_i - E_n} + \mathcal{O}(V_{\text{bare}}^3), \tag{6.3}$$

where the summation runs over both the low- and high-energy states of the full Hilbert space. Now the bare potential V_{bare} is replaced by $V_{\text{low-k}}$. In this case the sum does not run anymore to infinity but over the low-momentum space up to the cutoff Λ. $V_{\text{low-k}}$ is defined introducing a correction term δV_{ct} instead of the high-momentum potential V_H

$$V_{\text{low-k}} = V_L + \delta V_{ct}. \tag{6.4}$$

This correction term can be well approximated by contact interactions since the cutoff Λ results in short distance propagation of about $1/\Lambda$. The general form of

δV_{ct} should contain all local contact operators consistent with the symmetries of the high-momentum potential. Using $V_{\text{low-k}}$ one obtains the schematic equation for the amplitudes

$$\langle f|\mathcal{A}|i\rangle = \langle f|V_{\text{low-k}}|i\rangle + \sum_{n=0}^{\Lambda} \frac{\langle f|V_{\text{low-k}}|n\rangle\langle n|V_{\text{low-k}}|i\rangle}{E_i - E_n} + \mathcal{O}(V_{\text{low-k}}^3). \qquad (6.5)$$

The requirement that $V_{\text{low-k}}$ should be independent from the cutoff Λ and reproduce the same phase shifts as the bare potential leads to a renormalization group equation

$$\frac{d}{d\Lambda}\langle f|\mathcal{A}|i\rangle = 0 \;\longrightarrow\; \frac{d}{d\Lambda}V_{\text{low-k}} = \beta([V_{\text{low-k}}], \Lambda), \qquad (6.6)$$

where the flow of the renormalization group β depends on the low-momentum potential and the cutoff. The process of solving this equation is called "integrating out" or decimating the high-energy degrees of freedom. The details of high-momentum physics relevant for the low-momentum interaction are filtered out. The power counting scheme of EFT is a useful tool to truncate the correction terms δV_{ct} and fit the couplings to the low-energy data [BK+03].

To derive the RG equation explicitly one starts from the Lippmann-Schwinger (LS) equation for the off-shell matrix

$$T = V_{NN} + V_{NN}G_0 T \qquad (6.7)$$

or in the partial-wave notation

$$T(k', k; \omega) = V_{NN}(k', k) + \frac{2}{\pi}\mathcal{P}\int_0^\infty V_{NN}(k', p)\frac{p^2 dp}{\omega - p^2}T(p, k; \omega), \qquad (6.8)$$

where under V_{NN} a realistic potential is assumed, k and k' are the relative momentum of incoming and outgoing nucleons respectively, and T is the T-matrix. The next step is to replace the "bare" LS equation (6.8) by the cutoff one, which incorporates $V_{\text{low-k}}$ interaction instead of the "bare" V_{NN}. However, there is no such energy-independent potential that satisfies the resulted equation for the fully off-shell T-matrix [Ha08]. In this situation the modified Lippmann-Schwinger equation may be determined only for HOS T-matrix

$$T_{\text{low-k}}(k', k; k^2) = V_{\text{low-k}}(k', k) + \frac{2}{\pi}\mathcal{P}\int_0^\Lambda V_{\text{low-k}}(k', p)\frac{p^2 dp}{k^2 - p^2}T_{\text{low-k}}(p, k; k^2), \quad (6.9)$$

where Λ is the cutoff. The rigorous mathematical bridge between the standard LS equation (6.8) and the last equation(6.9), which determines $V_{\text{low-k}}$, is not trivial and can be provided by introducing the so-called $\hat{Q}$-box within the Kuo-Lee-Ratcliff (KLR) folded diagram theory [KLR71] [5]. From the condition

$$\frac{d}{d\Lambda} T_{\text{low-k}}(k', k; k^2) = 0 \tag{6.10}$$

we obtain the RG equation for $V_{\text{low-k}}$

$$\frac{d}{d\Lambda} V_{\text{low-k}}(k', k) = \frac{2}{\pi} \frac{V_{\text{low-k}}(k', \Lambda) T(\Lambda, k; \Lambda^2)}{1 - (k/\Lambda)^2}. \tag{6.11}$$

By construction, the low-momentum HOS T-matrix of the initial interaction is preserved by $V_{\text{low-k}}$ interaction obtained from the solution of differential RG equation (6.11)

$$T(k', k; k^2) = T_{\text{low-k}}(k', k; k^2); \text{ for } k', k \leq \Lambda. \tag{6.12}$$

The main result of the renormalization is that up to a cutoff of about $\Lambda \approx 2.1$ fm^{-1} the effective interaction $V_{\text{low-k}}$ remains independent on the input model. In Fig.6.4 this is shown by a collapse of two different realistic forces in $^1S_0$ channel after the renormalization. This allows us to say, that $V_{\text{low-k}}$ is unique and, as it reproduces by construction the experimental phase shifts and the deuteron binding energy as accurate as the high precision models, it can also be regarded as a *realistic* low-momentum interaction. There is no need anymore to make assumptions on the short-range part of interaction. The renormalization filters out the short distance details of the input potential and preserves the high-momentum correlations which contribute to low-momentum observables. Therefore the low-momentum potential $V_{\text{low-k}}$ is softer as usual many-body potentials and it is easier to apply it to many-body calculations because no Brueckner ladder resummation or short-range correlation methods are needed.

An alternative method to define an effective Hamiltonian for a model space is based on a unitary transformation of the initial Hamiltonian. Such approach was suggested by Lee and Suzuki ([LS80]), and leads to the energy-independent, hermitian effective interaction.
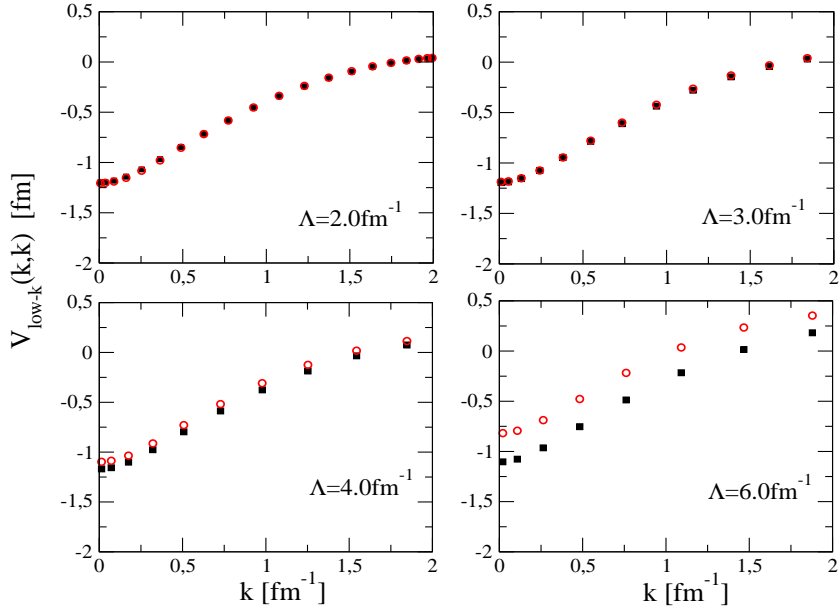
---

[5]For details see [Ha08].

Figure 6.4: The $^1S_0$ channel of $V_{\text{low-k}}(k,k)$ potential generated from Argonne V18 (circules) and CDBonn (squares) potentials for different values of the cutoff Λ.

6.3 The Model Space Technique

The decoupling of the full Hilber space on two model spaces, which incorporate the low- and medium-momenta, and its complement with the high-momentum components was proposed by Suzuki and Okamoto on the basis of the unitary-model-operator-approach referred to shortly as UMOA. The UMOA was first formulated by Providencia and Shakin [PS64], and followed by several authors [S82], [SO94]. Later these authors developed new principles for determining the unitary transformation by applying the effective-interaction theory of the Hermitian form. The new version of UMOA enables us to use the Hermitian, energy-independent and decoupled effective interaction instead of the G-matrix. UMOA has also been used to calculate the ground state properties of finite nuclei [SO94], [KSO97], [FOS04], [RP$^+$06].

The effective NN interaction is defined in a low-momentum subspace of the Hilbert space, the so-called P-space. This subspace is determined by the projection operator $\hat{P}$. The complement (Q-space) of P-space is uniquely identified by the projection operator $\hat{Q}$. For simplicity we will omit the "hat" notation for operators $\hat{O} \to O$.

The projection operators P and Q satisfy the usual relations as

$$P + Q = 1, \tag{6.13}$$

$$P^2 = P, \ Q^2 = Q, \tag{6.14}$$

$$PQ = QP = 0, \tag{6.15}$$

thus the transformed Hamiltonian does not couple the P- and Q-spaces.

In the UMOA the resulting Hamiltonian can be evaluated by using of a cluster expansion of unitary transformed Hamiltonian. The cluster expansion technique yields the effective interaction terms between two, three and more particles, even if one considers a realistic interaction with two-body terms only [6]. In the previous study of the finite nuclei the contribution of the three-body clusters was investigated. It was found that the three-body clusters do not have a significant contribution and therefore one can neglect the three-body terms for simplicity.

Here we determine an effective two-body interaction and consider only two-body systems. The effective interaction of Hermitian type is written as

$$V_{\text{eff}} = U^{-1}(h_0 + v_{12})U - h_0, \tag{6.16}$$

where v_{12} is the bare two-body NN interaction and U is an operator, which determines this transformation. The one-body term h_0 contains the kinetic energy t_i. However if we consider an effective interaction between two nucleons in the medium of nuclear matter the single-particle potential u_i must be added

$$h_0 = t_1 + u_1 + t_2 + u_2. \tag{6.17}$$

Following [S82] one can define the operator U as

$$U = (1 + \omega - \omega^\dagger)(1 + \omega\omega^\dagger + \omega^\dagger\omega)^{-1/2}, \tag{6.18}$$

where ω is defined as an operator satisfying the conditions

$$\omega = Q\omega P, \tag{6.19}$$

$$P\omega P = Q\omega Q = P\omega Q = 0. \tag{6.20}$$

The operator ω is active only when a P-space is multiplied from the r.h.s. or a Q-space states from the l.h.s. This leads to the property $\omega^2 = \omega^{\dagger\,2} = \omega^3 = \cdots = 0$.

---

[6] A very simple schematic illustration to this statement is given in [FN+97].
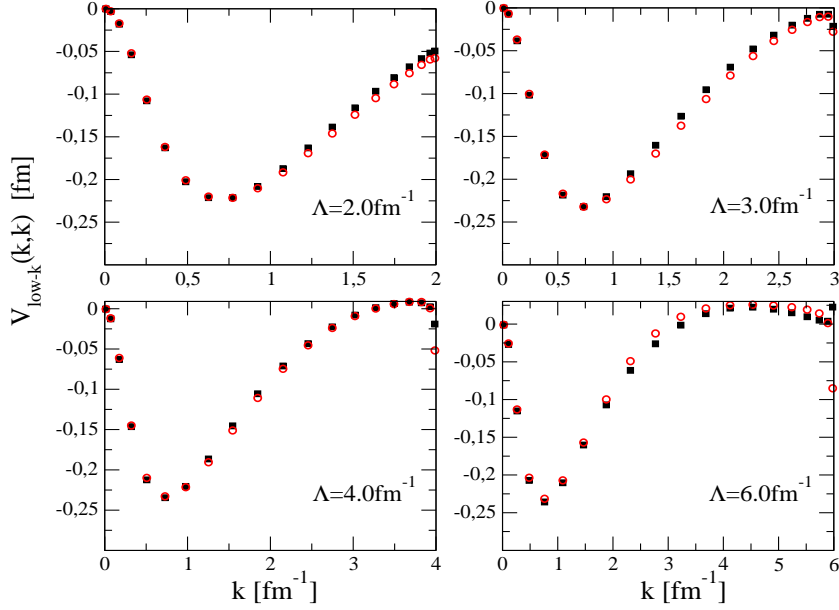
Figure 6.5: The $^3S_1$-$^3D_1$ channel of $V_{\text{low-k}}(k,k)$ potential generated from Argonne V18 (circles) and CDBonn (squares) potentials for different values of the cutoff Λ.

Historically the operator ω was introduced to construct the non-Hermitian effective interaction within the Rayleigh-Schrödinger perturbation theory. Following the original paper by Suzuki [S82] the operator U can be written as

$$U = \exp\{G\}, \tag{6.21}$$

where G fulfills the relation $G^\dagger = -G$. The connection between G and ω can be proved to be

$$G = arctahn(\omega - \omega^\dagger) = \sum_{n=0}^\infty \frac{(\omega - \omega^\dagger)^{2n+1}}{2n+1}. \tag{6.22}$$

In this case the operator U is related with ω as

$$U = \exp\{arctahn(\omega - \omega^\dagger)\} = (1 + \omega - \omega^\dagger)(1 + \omega\omega^\dagger + \omega^\dagger\omega)^{-1/2}. \tag{6.23}$$

Thus we recover (6.18). Operators $\omega^\dagger\omega$ and $\omega\omega^\dagger$ are active only in the P-space and in the Q-space, respectively. This expression for U (6.18) agrees with the block form obtained by Okubo [O54]

$$U = \begin{pmatrix} P(1 + \omega^\dagger\omega)^{-1/2}P & -P\omega^\dagger(1 + \omega\omega^\dagger)^{-1/2}Q \\ Q\omega^\dagger(1 + \omega^\dagger\omega)^{-1/2}P & Q(1 + \omega\omega^\dagger)^{-1/2}Q \end{pmatrix}.$$

Now to determine the effective interaction (6.16) one needs the matrix element of ω. First, one starts solving exactly the two-body eigenvalue equation

$$(h_0 + v_{12})|\Phi_k\rangle = E_k|\Phi_k\rangle, \tag{6.24}$$

where $|\Phi_k\rangle$ is the eigenvector. Now the matrix elements of ω in the basis of $|p\rangle$ $(|q\rangle)$ states in the $P(Q)$-space are determined from

$$\langle q|\omega|p'\rangle = \sum_{p=1}^{N_p}\langle q|Q|\Phi_p\rangle\langle\tilde{\varphi}_p|p'\rangle, \tag{6.25}$$

where N_p stands for the dimension of the P-space, and $\langle\tilde{\varphi}_p|$ is the biorthogonal state of $|\phi_k\rangle = P|\Phi_k\rangle$ satisfying

$$\sum_p\langle\tilde{\varphi}_k|p\rangle\langle p|\varphi_{k'}\rangle = \delta_{kk'}, \tag{6.26}$$

$$\sum_k\langle p'|\tilde{\varphi}_k\rangle\langle\varphi_k|p\rangle = \delta_{pp'}. \tag{6.27}$$

The Eq.(6.25) determines those N_p, which have the largest overlap with the P-space. Now, to obtain the matrix elements of U, we solve the eigenvalue equation for $\omega^\dagger\omega$ in the P-space

$$\omega^\dagger\omega|\chi_p\rangle = \mu_p^2|\chi_p\rangle. \tag{6.28}$$

The solution of this eigenvalue problem gives a new ket vector $|\nu_p\rangle$

$$|\nu_p\rangle = \frac{1}{\mu_p}\omega|\chi_p\rangle, \tag{6.29}$$

which is due to the relation $\omega = Q\omega P$ can be written as

$$\langle q|\nu_p\rangle = \frac{1}{\mu_p}\sum_{p'}\langle q|\omega|p'\rangle\langle p'|\chi_p\rangle. \tag{6.30}$$

Now, with the help of Eqs.(6.28)-(6.30) we obtain the matrix elements for unitary transformation operator U

$$\langle p''|U|p'\rangle = \langle p''|(1 + \omega^\dagger\omega)^{-1/2}|p'\rangle \tag{6.31}$$

$$= \sum_{p=1}^{N_p}(1 + \mu_p^2)^{-1/2}\langle p''|\chi_p\rangle\langle\chi_p|p'\rangle, \tag{6.32}$$

$$\langle q|U|p'\rangle \ = \ \langle q|(1+\omega^\dagger\omega)^{-1/2}|p'\rangle \tag{6.33}$$

$$= \ \sum_{p=1}^{N_p}(1+\mu_p^2)^{-1/2}\mu_p\langle q|\nu_p\rangle\langle\chi_p|p'\rangle, \tag{6.34}$$

$$\langle p'|U|q\rangle \ = \ -\langle p'|\omega^\dagger(1+\omega\omega^\dagger)^{-1/2}|q\rangle \tag{6.35}$$

$$= \ -\sum_{p=1}^{N_p}(1+\mu_p^2)^{-1/2}\mu_p\langle p'|\chi_p\rangle\langle\nu_p|q\rangle, \tag{6.36}$$

$$\langle q'|U|q\rangle \ = \ \langle q'|(1+\omega\omega^\dagger)^{-1/2}|q\rangle \tag{6.37}$$

$$= \ \sum_{p=1}^{N_p}\{(1+\mu_p^2)^{-1/2}-1\}\langle q'|\nu_p\rangle\langle\nu_p|q\rangle + \delta_{q,q'}. \tag{6.38}$$

This matrix element of U can then be used to determine the matrix elements of the effective interaction $V_{\rm eff}$ in P-space, where $V_{\rm eff}$ is nothing else but $V_{\rm low\text{-}k}$ [BDM06, FOS04].

In Fig.6.4 we demonstrate the evolution of $^1S_0$ channel[7] of $V_{\rm low\text{-}k}$ produced for CD-Bonn and Argonne V18 potentials at different values of Λ. One can see that the model independence of $V_{\rm low\text{-}k}$ is reached at the cutoff around $\Lambda \simeq 3.0$ fm^{-1}. This value of the cutoff lies below the masses of ω and ρ mesons, and therefore the resulted low-momentum interaction is not sensitive to the details of the short-range core.

The origin of the tensor interaction of $V_{\rm low\text{-}k}$ can be investigated in the coupled channel $^3S_1$-$^3D_1$. The evolution of this channel with increasing cutoff Λ is shown in Fig.6.5. It can be seen that for the relative momenta below $k \leq 0.7$ fm^{-1} both realistic potentials are identical. Since the momentum $k \simeq 0.7$ fm^{-1} corresponds to the pion mass m_π we can conclude that the underlying realistic forces have the same one-pion-exchange part, as mentioned already above. The high-momentum part ($k > 0.7$ fm^{-1}) of the matrix element is sensitive to the choice of Λ.

Note that this separation into low- and high-momentum components is only for two nucleons in the vacuum. Employing the resulting interaction in a many-body calculations is essentially based on the assumption that this separation is not affected

---

[7]Here the nuclear spectroscopical notation $^{2S+1}L_J$ is used, where S is the total spin of the NN system, J denotes its total angular-momentum, and L denotes its orbital angular momentum.

by the medium of other nucleons. If the same scheme would be applied, e.g., to a basis of three-nucleon states the resulting low-momentum Hamiltonian will contain terms, which have to be treated as an effective three-body interaction.

6.4 $V_{\text{low-k}}$ Hartree-Fock Calculations

The $V_{\text{low-k}}$ interaction can be produced by using either the RG treatment or the model space technique. Both approaches are equivalent and lead to the same energy-independent potential. In practice, however, most calculations with $V_{\text{low-k}}$ are based on the model space method rather than the differential equations of the RG because the latter are numerically more robust [BF+08]. In the following we will consider $V_{\text{low-k}}$ produced after UMOA.

Since $V_{\text{low-k}}$ does not contain the strong short-range components it can be used in the Hartree-Fock calculations. Performing such calculations[8] for the symmetric nuclear matter one obtains a binding energy increasing with density in a monotonic way [BDM06, GV+09, KM+03]. It is shown on Fig.6.6 by solid line. This absence of the saturation is one of the main problems in calculations employing $V_{\text{low-k}}$. This problem cannot be cured by the inclusion of correlations beyond the HF approximation, e.g., by means of Brueckner-Hartree-Fock (BHF) approximation [BDM06]. Therefore one can argue that the low-momentum interaction does not reproduce the saturation as it misses the quenching of the short-range correlations in the nuclear medium. Here we should stress, that in fact the BHF calculations lead to the saturation of symmetric nuclear matter, however such results are not able to reproduce the empirical saturation point [MP00, CC+70]. The correct saturation can be achieved if one includes a three-body force [LLZ00], or by considering the relativistic effects, viz., the change of the nucleon Dirac spinors in the medium [VFF04, VFF07, BM84, MMB90]. Recent relativistic calculations by van Dalen and Müther demonstrate that saturation in the symmetric nuclear matter can be achieved within the $V_{\text{low-k}}$ approach by inclusion of relativistic effects in dressing the Dirac spinors, used to evaluate the underlying realistic interaction [VDM09]. In

---

[8]Calculations of the bulk properties of infinite homogeneous matter require only the diagonal part of matrix element $V_{\text{low-k}}(k,k)$ (see, e.g., [HT70]). Study of the single-particle spectrum is possible within the WS cell approximation.
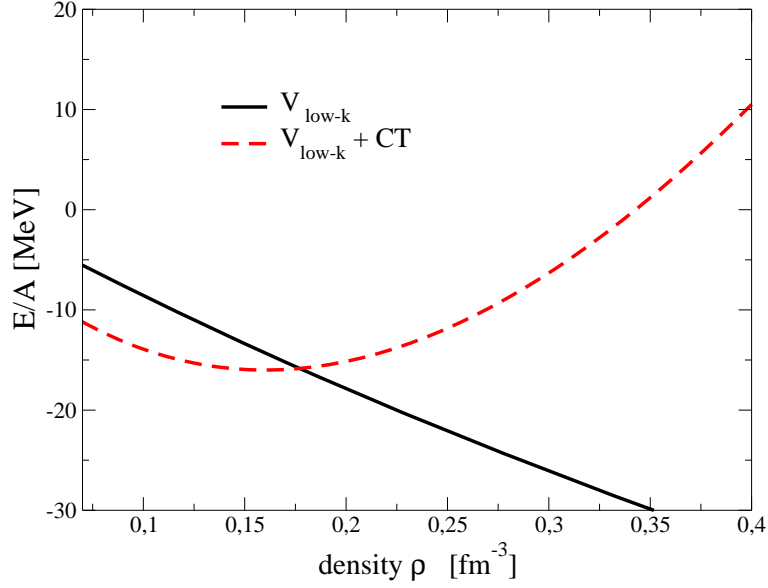
Figure 6.6: Comparison of binding energy per nucleon of symmetric nuclear matter. Results of Hartree-Fock calculations with $V_{\text{low-k}}$ (solid) and $V_{\text{low-k}}$ plus contact term (dashed).

nonrelativistic calculations it corresponds to the inclusion of a density-dependent two-body interaction [GV$^+$09] or an effective three-body force [BS$^+$05]. Therefore we supplement the low-momentum interaction by a simple contact interaction (CT), which takes into account three-body correlations and was chosen due to conventional Skyrme parameterization

$$\Delta\nu = \Delta\nu_0 + \Delta\nu_3, \qquad (6.39)$$

with

$$\Delta\nu_0 = \frac{1}{4}t_0[(2+x_0)\rho^2 - (2x_0+1)(\rho_n^2 + \rho_p^2)] \qquad (6.40)$$

and

$$\Delta\nu_3 = \frac{1}{24}t_3\rho^\alpha[(2+x_3)\rho^2 - (2x_3+1)(\rho_n^2 + \rho_p^2)], \qquad (6.41)$$

where ρ_p and ρ_n refer to the local densities for protons and neutrons while the matter density is denoted as $\rho = \rho_n + \rho_p$. The parameters of the contact interaction are t_0, x_0, t_3, x_3 and α. As described below we have chosen a fixed value of $\alpha = 0.5$ and $x_0 = 0.0$ and fitted t_0, t_3 and x_3 in such a way that Hartree-Fock calculations using $V_{\text{low-k}}$ plus contact term of Eq.(6.39) yield the empirical saturation point for symmetric nuclear matter with a binding energy E/A = -16.0 MeV at the density ρ_0
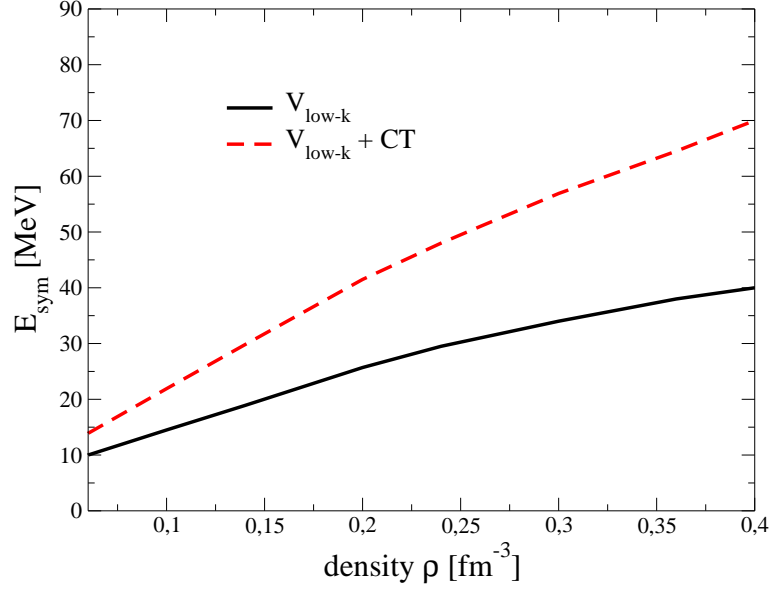
Figure 6.7: The symmetry energy as a function of baryon density. The Hartree-Fock calculations with $V_{\text{low-k}}$ (solid) and $V_{\text{low-k}}$ plus contact term (dashed).

$= 0.16$ fm^{-3} (see dashed line on Fig.6.6). We should notice that only the isoscalar part of the contact term (6.39) can be fixed with the help of the symmetric nuclear matter. The isovector part can be adjusted by inspecting the symmetry energy. On Fig.6.7 the symmetry energy as a function of density is shown. The calculations with $V_{\text{low-k}}$ gives only $E_{sym} = 21$ MeV at the saturation density, thus only about two-thirds of the experimental value. This can be explained by the softness of $V_{\text{low-k}}$. We choose $\alpha = 0.5$ and $x_0 = 0.0$ and the remaining three parameters are fixed in order to reproduce the symmetry energy as well as the saturation point. These parameters are summarized in Table 6.1.

After the contact interaction has been adjusted to reproduce the saturation of symmetric nuclear matter, one can proceed investigating the bulk properties of finite nuclei. The Hartree-Fock calculations must be performed in the WS cell approximation, thus the whole space is restricted to a spherical cell. Within the HF approximation the interaction model $V_{\text{low-k}}$ leads to a single-particle Hamiltonian for protons and neutrons ($\tau = n, p$) of the form

$$H_\tau = H^{kin} + H_\tau^{V_{\text{low-k}}} + \Delta H_\tau^{ct} + H_\tau^{Coul}\delta_{\tau p}, \qquad (6.42)$$

where H^{kin} is the kinetic part, ΔH^{ct} originates from the contact interaction of

Eq.(6.39). This part is given by

$$\Delta H_\tau^{ct} = \frac{t_0}{2}[(2+x_0)\rho - (1+2x_0)\rho_\tau] + \frac{t_3}{24}[(2+x_3)(2+\alpha)\rho^{1+\alpha} \qquad (6.43)$$
$$- (2x_3+1)\{2\rho^\alpha\rho_\tau + \alpha\rho^{\alpha-1}(\rho_n^2 + \rho_p^2)\}]. \qquad (6.44)$$

The Coulomb contribution for protons

$$H^{Coul} = U_{dir}^{Coul} + U_{exch}^{Coul}, \qquad (6.45)$$

where the direct term is

$$U_{dir}^{Coul} = 4\pi e^2 \begin{cases} \int dr' r'^2 \rho_p(r')/r, & r' \leq r \\ \int dr' r' \rho_p(r'), & r' \geq r, \end{cases} \qquad (6.46)$$

and the exchange term can be written as

$$U_{exch}^{Coul} = -e^2 \left(\frac{3}{\pi}\right)^{1/3} \rho_p^{1/3}. \qquad (6.47)$$

Since the effective interaction $V_{\text{low-k}}$ is nonlocal and defined in terms of matrix elements in momentum space the Hartree-Fock calculations has to be performed in a Hilbert space using an appropriate basis $|\alpha\rangle, |\beta\rangle \ldots$. The HF Hamiltonian is then expressed in terms of the matrix elements between these basis states $\langle\alpha|H_{HF}|\beta\rangle$ and the single-particle states $|\Psi_n\rangle$ are defined in terms of the expansion coefficients in this basis

$$|\Psi_n\rangle = \sum_\alpha |\alpha\rangle\langle\alpha|\Psi_n\rangle = \sum_\alpha c_{n\alpha}|\alpha\rangle. \qquad (6.48)$$

The part of the HF Hamiltonian originating from $V_{\text{low-k}}$ can be expressed in terms of two-body matrix elements by

$$\langle\alpha|H_{\text{low-k}}|\beta\rangle = \sum_{\gamma,\delta}\langle\alpha\gamma|V_{\text{low-k}}|\beta\delta\rangle\rho_{\gamma\delta}, \qquad (6.49)$$

where $\rho_{\gamma\delta}$ is the single-particle density matrix. As the next step one has to choose an orthogonal basis system. The matrix element $\langle\alpha\gamma|V_{\text{low-k}}|\beta\delta\rangle$ is easy to calculate within the harmonic oscillator (HO) basis. First, one calculates the oscillator matrix element using the momentum representation of the relative basis. After that this matrix element must be transformed from the two-body center-of-mass system to the laboratory system by using the well-known Talmi-Moshinsky brackets [Mo59,

Interaction	t_0 [MeV fm^3]	t_3 [MeV fm$^{3+3\alpha}$]	x_3
CT	-584.1	8330.7	-0.5

Table 6.1: Parameters of the contact interaction defined in Eq.(6.39).

Interaction	^{16}O	^{40}Ca	^{48}Ca	^{60}Ca	^{208}Pb
	E/A [MeV]				
$V_{\text{low-k}}$+CT	-7.91	-8.57	-8.42	-7.75	-7.76
Experiment	-7.98	-8.55	-8.67	–	-7.87
	r_{ch} [fm]				
$V_{\text{low-k}}$+CT	2.79	3.50	3.54	3.68	5.51
Experiment	2.74	3.48	3.47	–	5.50

Table 6.2: The binding energy per nucleon and rms charge radii of finite nuclei derived from Hartree-Fock calculations with $V_{\text{low-k}}$+CT interaction. The center-of-mass correction to the binding energy was performed after variation (see Eq.(2.35)). The charge radii were found from the charge density (6.51). Experimental data taken from Refs. [Br98, AW93, Ch$^+$96, Fr$^+$95].

Ta52, Ta93]. The HO basis is used successfully in calculations of the bulk properties of deeply bound nuclei. The validity of this basis in description of weakly bound wave functions of nucleons is rather questionable. Such weakly bound nucleons exist in exotic nuclei close to the dripline, as well as in pasta structures, which appear in the inner crust of neutron stars. The asymptotic behavior of weakly bound wave functions can be very good approximated by an exponential, but not the Gaussian typical for HO basis. Therefore it was suggested that the nucleon wave functions should be expanded in terms of plane waves (4.4). In the PW basis the calculation of $V_{\text{low-k}}$ matrix elements in the relative basis is trivial, however the transformation from the relative to the laboratory coordinate frames is much less convenient, since it involves the evaluation of the vector brackets [KKR79, BM89].

The calculations with the PW basis are sensitive to the radius of the cell R_{WS}. For small radii the resolution of the radial momenta k_{il} (see Eq.(4.4)) may be insufficient. For larger cells, however, one needs a larger number of basis function in order to

cover the relevant range of momenta. It was found that the optimal choice is a radius of WS cell, which is about 5 times larger than the nuclear radius. So we used $R_{WS} = 15$ fm for nuclei from ^{16}O to ^{60}Ca, while $R_{WS} = 40$ fm for nucleus ^{208}Pb.

In Table 6.2 the energy per nucleon of finite nuclei is shown. The $V_{\text{low-k}}$ interaction is supported with the contact interaction, which is adjusted to the properties of nuclear matter. This interaction model gives a good agreement for binding energies and charge radii of finite nuclei in comparison with the experimental data. The nuclear charge radius can be found from

$$r_C = \sqrt{\langle r^2 \rangle} = \frac{\int d^3 r\, r^2 \rho_C(\mathbf{r})}{\int d^3 r \rho(\mathbf{r})}, \qquad (6.50)$$

where the charge density is calculated from the proton density ρ_p

$$\rho_C(\mathbf{r}) = \int d^3 r' f_p(\mathbf{r} - \mathbf{r}') \rho_p(\mathbf{r}'). \qquad (6.51)$$

Here the proton form factor $f_p(\mathbf{r} - \mathbf{r}')$ is taken as a Gaussian [BM$^+$87, VB72]

$$f_p(\mathbf{s}) = \frac{1}{r_0^3 \pi^{3/2}} e^{-\frac{\mathbf{s}^2}{r_0^2}}, \qquad (6.52)$$

with $r_0 = \sqrt{2/3}\langle r_p \rangle_{rms}$ and the root-mean-square charge radius of the proton taken as its free value $\langle r_p \rangle_{rms} = 0.8$ fm. The radii calculated in such a way are slightly larger than the experimental values due to a small global underbinding of nuclei. This reflects a very strong correlation between binding energies and charge radii of nuclei known for many years [CC$^+$70].

To investigate the single-particle structure of nuclei in details we show the single-particle energies[9] of ^{16}O in the Table 6.3. The deviation from the experimental values is on average about 10%. Although a large deviation in $1s_{1/2}$ level between the calculated value -37.162 MeV and experimental -47.0 MeV one should bear in mind that this level has a large experimental uncertainty.

All the results discussed above indicate that $V_{\text{low-k}}$ interaction, being constructed to describe the low-energy scattering data, may be successfully used in many-body calculations of finite nuclei and homogeneous nuclear matter. This universality of $V_{\text{low-k}}$ is a great advantage over those phenomenological models of NN interaction fitted to the bulk properties of nuclei and nuclear matter itself. So we can conclude

---

[9] The principal quantum number n is counted from 1, not from 0: $n = 1, 2, 3 \ldots$

Level	Neutrons		Protons	
	$V_{\text{low-k}}$+CT	Exp.	$V_{\text{low-k}}$+CT	Exp.
$1s_{1/2}$	-37.162	-47.00	-33.601	-44$\pm$ 7
$1p_{3/2}$	-20.006	-21.839	-16.632	-18.451
$1p_{1/2}$	-16.484	-15.663	-13.155	-12.127
$1d_{5/2}$	-3.739	-4.144	-0.690	-0.601
$2s_{1/2}$	-1.566	-3.273	0.839	-0.106
$1d_{3/2}$	0.339	0.941	1.886	4.399

Table 6.3: Single-particle energy levels of ^{16}O derived from Hartree-Fock calculations with $V_{\text{low-k}}$+CT interaction.

that the predictive power of $V_{\text{low-k}}$, which is so necessary in the astrophysical landscape due to the lack of experimental data, is rather plausible. In the nearest future $V_{\text{low-k}}$ will be used in calculations of the inhomogeneous nuclear matter, which exists in the crust of neutron stars. In this case the matter must be considered within the WS cell approximation (see Chapter 4). Therefore we would like to demonstrate a simple test for this approximation in $V_{\text{low-k}}$ Hartree-Fock calculations. With this aim the binding energy of the homogeneous, symmetric nuclear matter is calculated within the plane wave approximation (see Fig.6.6) as well as in the cell with Dirichlet boundary conditions. The influence of the shell effects on the kinetic energy is excluded, so that only the potential energy per nucleon is considered. The solid line in Fig.6.8 corresponds to the plane wave calculations, while energies resulting from the cell calculations are shown by various symbols.

The systematic discrepancy between the infinite matter and calculations in the WS cell of different radii is observed. This discrepancy cannot be explained by a small size of the cell, since upon varying the radius from $R_{WS} = 6$ fm to $R_{WS} = 10$ fm all points remain on the same line. Let us therefore suppose that the problem is hidden in the transition from the infinite matter to its representation within the isolated cell. This transition leads to the discretization of the energy spectrum of nucleon. Thus all particles occupy levels, which are characterized by the radial momenta k_{li} (see Eq.(4.4)). Therefore one can identify the momentum k_{li} of the last fully occupied level with the Fermi momentum k_F. It turns out that k_F defined in

Figure 6.8: Potential energy per nucleon of symmetric nuclear matter. Infinite matter (solid line) versus WS cell approximation (symbols). The Fermi momentum is determined as $k_F = (3\pi^2\rho/2)^{1/3}$.
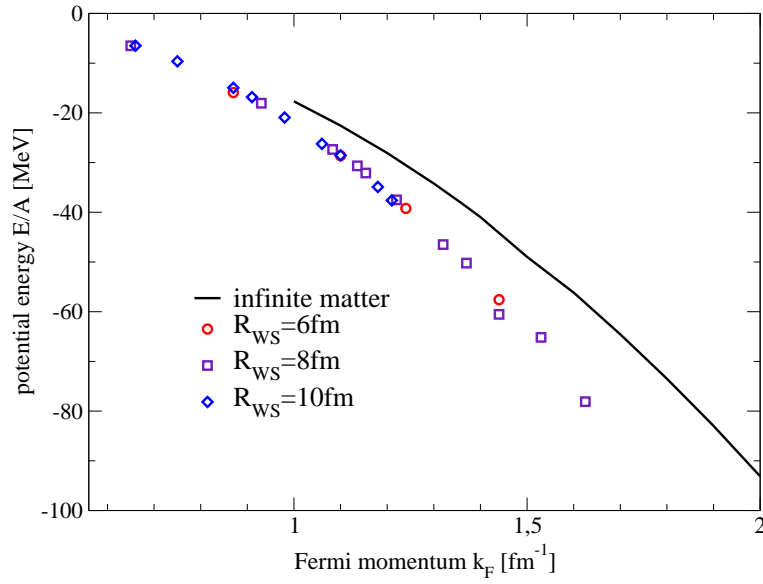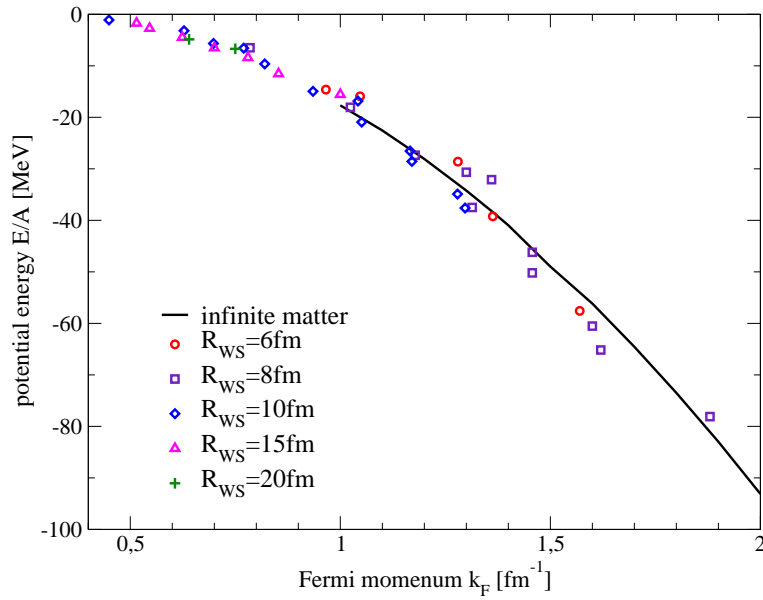

Figure 6.9: Potential energy per nucleon of symmetric nuclear matter. Infinite matter (solid line) versus WS cell approximation (symbols). The Fermi momentum is determined from the radial momenta k_{li}.

such a way does not coincide with the Fermi momentum derived from the relation $k_F = (3\pi^2 \rho/2)^{1/3}$, which is shown on the ordinate axis of Fig.6.8. There occurs an uncertainty in definition of the Fermi momentum due to the discretized representation of the continuous energy spectrum. To check whether k_F is connected to the wave vector k_{li} or the average density of nucleons $\rho = (N + Z)/V_{cell}$ the potential energy as a function of $k_F = k_{li}$ was computed. The respective results are shown in Fig.6.9. In spite of larger shell model oscillations the WS cell approximation gives results which are closer to the predictions of infinite matter. Therefore we may conclude that k_F determined as the radial momentum of the highest occupied orbit is the correct assumption. It leads to a new definition of the density, which instead of $\rho = (N + Z)/V_{cell}$ should be calculated from the Fermi momentum $\rho = 2k_F^3/(3\pi^2)$. One should keep in mind this difference by calculating the inhomogeneous nuclear matter.

Jumping ahead, we would like to notice, that all $V_{\text{low-k}}$ Hartree-Fock calculations within the WS cell remain very time consuming in comparison with the standard Skyrme Hartree-Fock scheme, mainly due to the nonlocality of $V_{\text{low-k}}$. One can solve this problem by construction of a separable form of $V_{\text{low-k}}$, as explained in the next Section.

6.5 Separable Form of $V_{\text{low-k}}$

In the previous Section we considered the realistic low-momentum interaction $V_{\text{low-k}}$ and its application in many-body calculations of finite nuclei and nuclear matter. Here the separability of low-momentum interaction is investigated by using the diagonalization of $V_{\text{low-k}}$ matrix in momentum space for each partial wave channel. This allows finding a low rank separable form of $V_{\text{low-k}}$, which simplifies the Hartree-Fock calculations.

Originally $V_{\text{low-k}}$ is nonlocal and defined in terms of matrix elements in a basis of NN states labeled by the relative momentum for pairs of nucleons. Thus for each partial wave channel there exists a matrix, which represents $V_{\text{low-k}}(k, k')$ on a mesh of N discretized relative momenta k and k' in the range $0 \leq k, k' \leq \Lambda$. Since this matrix is real and symmetric with respect to k, k' one can diagonalize it, so that it can be
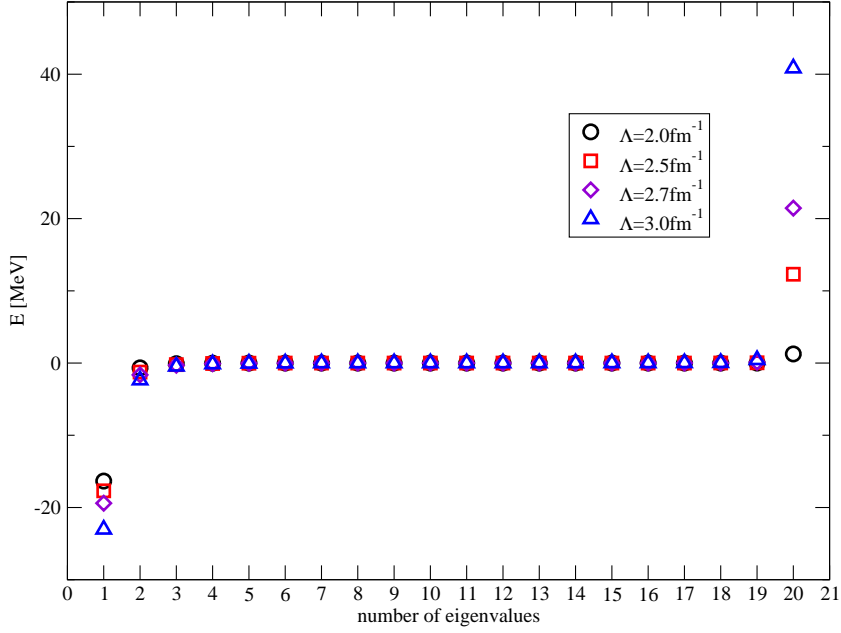
Figure 6.10: Top: Nonzero eigenvalues a_i of $^1S_0$ channel. Bottom: Nonzero eigenvalues a_i of $^3S_1$-$^3D_1$ channel.

written as a sum of N real eigenvalues multiplied with the respective eigenvectors

$$V_{\text{low-k}}(k, k') = \sum_{i=1}^{N} a_i f_i^*(k) f_i(k'),$$ (6.53)

where N is the number of mesh-points and the dimension of $V_{\text{low-k}}$ matrix. The eigenvectors $f_i(k)$ satisfy the orthogonality relation

$$\frac{2}{\pi} \int_0^{\Lambda} dk k^2 f_i(k) f_j(k) = \delta_{ij}.$$ (6.54)

In the following we will omit the symbol of complex conjugation because all eigenvectors are real. The last equality (6.53) is nothing else but the general definition of a separable potential of the rank N. If the rank of the separable potential equals to the dimension of the matrix $V_{\text{low-k}}(k, k')$ the whole information is exactly restored from the eigenvalues a_i and eigenvectors f_i. As we will see later, some of eigenvalues a_i can be zero or negligibly small so that one can reduce the rank of separable interaction taking into account only the n eigenvalues with the largest absolute values. It leads to a new approximated separable interaction $V_{\text{low-k}}^{[n]}(k, k')$

$$V_{\text{low-k}}(k, k') \simeq V_{\text{low-k}}^{[n]}(k, k') = \sum_{i=1}^{n} a_i f_i(k) f_i(k'), \qquad (n \leq N).$$ (6.55)
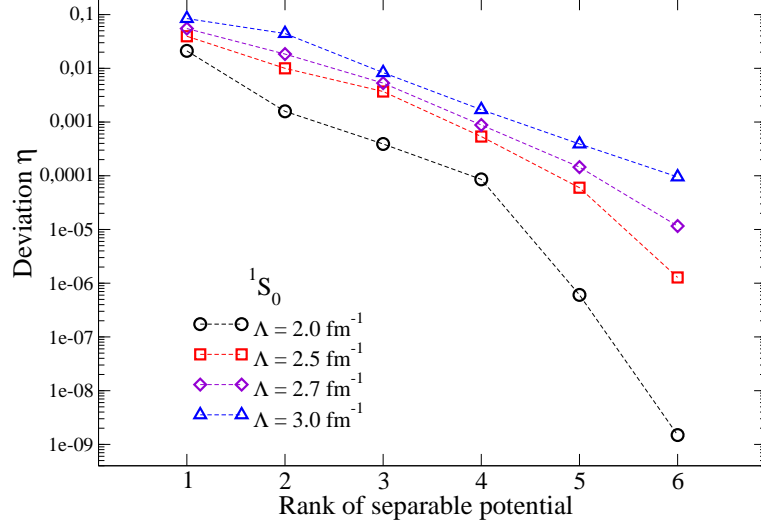
Figure 6.11: Squared deviation of the separable $V^{[n]}_{\text{low-k}}(k, k')$ from the original $V_{\text{low-k}}(k, k')$ in $^1S_0$ channel for different values of the cutoff parameter Λ.

The low-rank separable representation of NN interaction leads to significant simplifications in many-body calculations.

In the following we discuss the results for symmetric nuclear matter as well as finite nuclei obtained from HF calculations. These calculations are performed in the model space, which is defined by a cutoff parameter Λ in the two-body scattering equation, employing the corresponding low-momentum interaction $V_{\text{low-k}}$, derived from the CDBonn [MSS96] interaction using the technique described in the previous Section. The NN interaction has been restricted to partial waves with total angular momentum $J \leq 6$.

We start our discussion with the comparison of the eigenvalues a_i obtained from diagonalization of 20×20 matrix of $V_{\text{low-k}}(k, k')$ in $^1S_0$ channel. The resulted nonzero eigenvalues are shown on the top of Fig.6.10 for different values of Λ. As it was discussed above, $V_{\text{low-k}}$ interaction becomes model independent at $\Lambda = 2$ fm^{-1}. At this value of the cutoff parameter Λ the diagonalization procedure yields only 11 nonzero eigenvalues, in other words, $V_{\text{low-k}}$ interaction in $^1S_0$ channel is a separable interaction of the 11th rank or, following (6.53), one can write

$$V^{[11]}_{\text{low-k}}(k, k') = V_{\text{low-k}}(k, k'). \tag{6.56}$$

The nonzero eigenvalues are essentially independent on N, the dimension of the

matrix representing $V_{\text{low-k}}$. Going further one can notice, that many of the nonzero eigenvalues are nevertheless very small, and only some of them, e.g., at $i = 1, 2, 20$ carry the main part of the information about the interaction model. This gives rise to a substantial lowering of the rank of separable potential, as it was shown in Eq.(6.55). With the increase of the cutoff Λ the absolute values of the eigenvalues increase as well and as a consequence the rank n of the separable form $V_{\text{low-k}}^{[n]}$ defined in (6.55) has to be increased to achieve a reasonable accuracy. Increasing Λ more information about the short-range components of the underlying bare interaction is included, which requires a larger rank in the separable representation of the interaction.

In case of the coupled channels, like ${}^3S_1$-${}^3D_1$ channel, the dimension N of the $V_{\text{low-k}}$ matrix is twice as large if one keeps the number of mesh-points in each channel the same as for the uncoupled partial waves. It turns out that also the number of nonzero eigenvalues increases as shown in the lower panel of Fig.6.10. It is obvious that the rank of the separable potential should be higher than for ${}^1S_0$ channel. It is a general feature that coupled channels require higher rank separable interaction than the uncoupled ones [HP84]. Also one observes pairs of positive and negative eigenvalues which have about the same absolute value. This picture remains for higher values of Λ. As we will see later, this symmetry between positive and negative eigenvalues will play a crucial role in convergence of the separable form $V_{\text{low-k}}^{[n]}$ to the initial $V_{\text{low-k}}$ with increase of rank.

In order to determine a minimal rank for a reliable separable approximation in each channel we calculate the square deviation η of the separable form $V_{\text{low-k}}^{[n]}$ from the original potential $V_{\text{low-k}}$ for each rank n

$$\eta = \sum_{k,k'} \left| V_{\text{low-k}}(k,k') - V_{\text{low-k}}^{[n]}(k,k') \right|^2 / \sum_{k,k'} \left| V_{\text{low-k}}(k,k') \right|^2. \qquad (6.57)$$

In case of the ${}^1S_0$ channel this deviation is shown in Fig.6.11. At $\Lambda = 2$ fm^{-1} one observes a fast convergence to zero deviation already at the rank $n = 2$. A very similar behavior is also observed for the other uncoupled channels. This indicates, that the separable potential of the second rank $V_{\text{low-k}}^{[2]}$ approximates with a high accuracy all uncoupled channels of the original $V_{\text{low-k}}$. The growth of the cutoff monotonically increases the rank of the separable potential. At $\Lambda = 3$ fm^{-1} one may expect a good accuracy starting from $n = 5$.

In Fig.6.12 we display the deviation η for ${}^3S_1$-${}^3D_1$ channel. First, at low n the
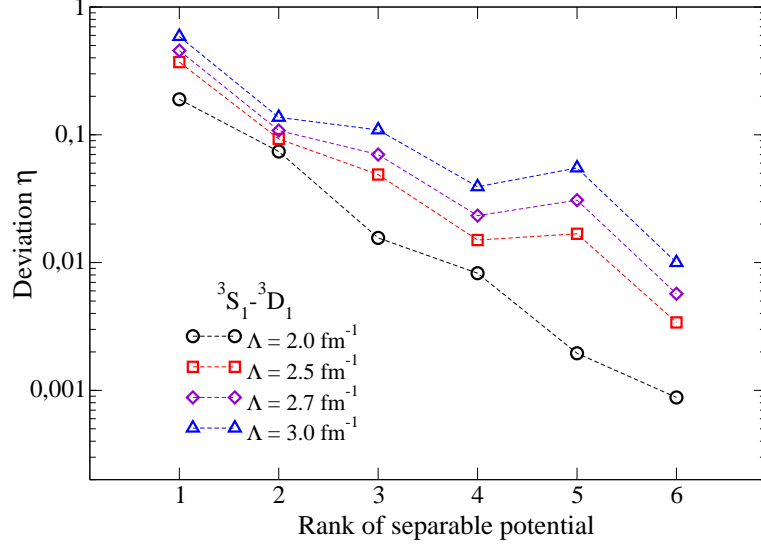
Figure 6.12: Squared deviation of the separable $V_{\text{low-k}}^{[n]}(k,k')$ from the original $V_{\text{low-k}}(k,k')$ in $^3S_1$-$^3D_1$ channel for different values of the cutoff parameter Λ.

absolute value of the deviation is one order of magnitude higher than for uncoupled $^1S_0$ channel. Increasing the rank one observes a non-monotonic, oscillating decrease of η, specially for high Λ. As we have seen, the diagonalization of the channel $^3S_1$-$^3D_1$ yields both positive and negative eigenvalues, which are symmetrically distributed over i. So that they form "pairs" with very similar absolute values. Assuming the odd rank we take into account either uncompensated positive or negative eigenvalue. This eigenvalue will be compensated in the next (even) rank, and the accuracy will be significantly improved.

The deviation η for other channels at $\Lambda = 2$ fm^{-1} is shown in Figs.6.13, 6.14. In the following we choose the second rank approximation for the uncoupled channels ($n = 2$) and the third rank for the coupled one ($n = 3$). Below, the respective separable version of $V_{\text{low-k}}$ will be referred to as $V_{\text{low-k}}^{[2,3]}$.

Now let us turn to the binding energy of symmetric nuclear matter, displayed in Fig.6.15. The HF calculations using $V_{\text{low-k}}^{[2,3]}$ (dashed line) yields essentially the same result as the one employing the original $V_{\text{low-k}}$ interaction (solid curve). The deviation does not exceed 1% at the saturation density ρ_0 and 1.7% at the density $2\rho_0$. We also compared the binding energy of pure neutron matter for both potentials and found that the discrepancy is less than 1% for the same range of densities.

Figure 6.13: Squared deviation of the separable $V_{\text{low-k}}^{[n]}(k, k')$ from the original $V_{\text{low-k}}(k, k')$ for various uncoupled channels at $\Lambda = 2$ fm^{-1}.
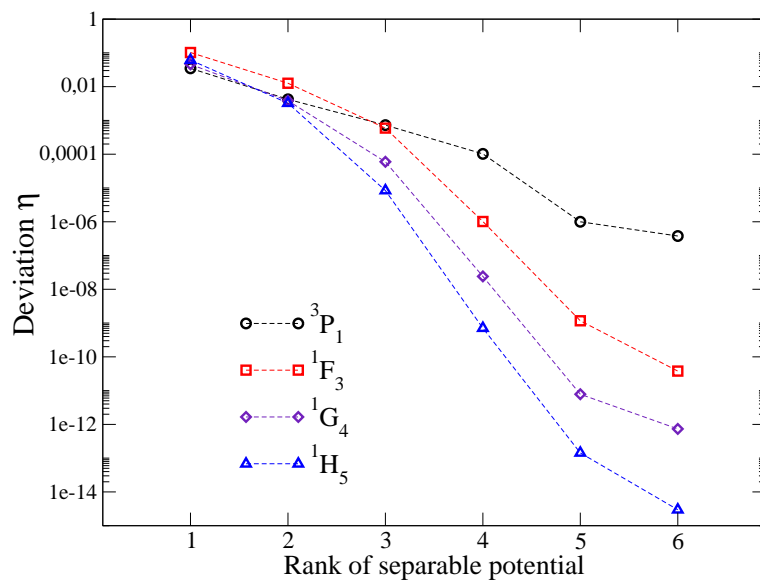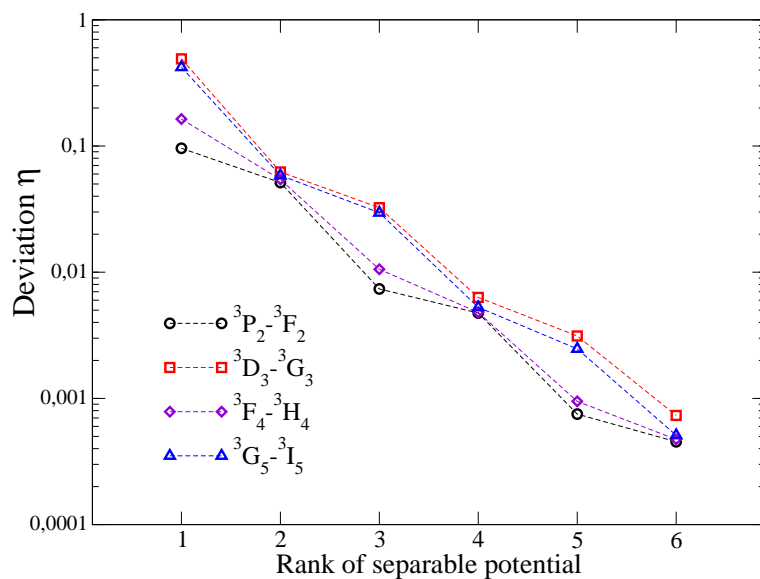

Figure 6.14: Squared deviation of the separable $V_{\text{low-k}}^{[n]}(k, k')$ from the original $V_{\text{low-k}}(k, k')$ for various coupled channels at $\Lambda = 2$ fm^{-1}.
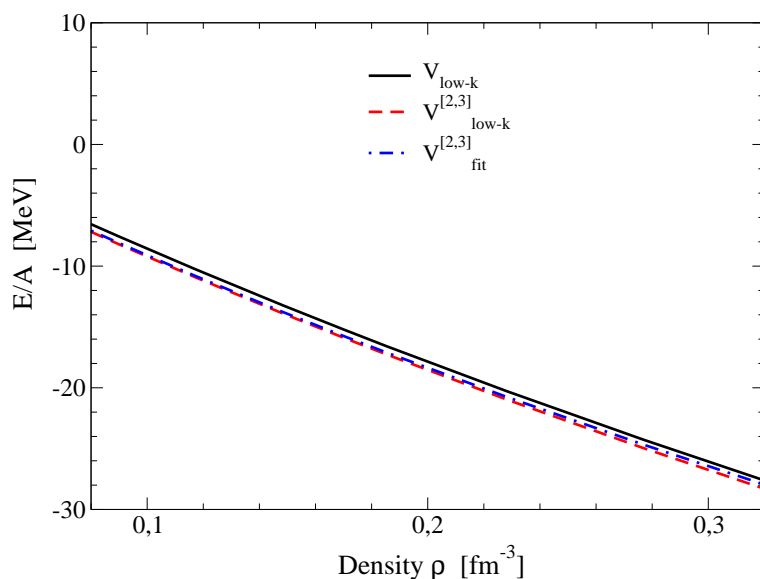
Figure 6.15: Energy per nucleon of symmetric nuclear matter as a function of the density. Results of $V_{\text{low-k}}$ interaction (solid line) compared with the separable form $V_{\text{low-k}}^{[2,3]}$ (dashed line) and the respective fitted form $V_{\text{fit}}^{[2,3]}$ (dashed-dotted line).

However, neither of the 2 calculations yields a saturation point, i.e. a minimum in the energy versus density plot, as it has been observed before [KM+03, BS+05]. This absence of the saturation is one of the main problems in calculations of nuclear matter employing $V_{\text{low-k}}$. It cannot be cured by the inclusion of correlations beyond the HF approximation, e.g., by means of the BHF approximation [BDM06]. Recent relativistic calculations by van Dalen and Müther demonstrate that saturation can be achieved within the $V_{\text{low-k}}$ approach by inclusion of relativistic effects in dressing the Dirac spinors which are used to evaluate the underlying realistic interaction [VDM09].

All the results obtained so far indicate that $V_{\text{low-k}}^{[2,3]}$ is an accurate low-rank separable representation of $V_{\text{low-k}}$ interaction. However, in order to make it accessible to other users, it should be parameterized in a simple form. Here we suggest the fitting function for all $f_i(k)$ in all channels

$$f_i(k) = \alpha_i + (\beta_i \exp\left(\gamma_i k^{\delta_i}\right) + \mu_i) \sin(k\sigma_i + \lambda_i), \qquad (6.58)$$

which contains 7 parameters for each partial wave channel and each $f_i(k)$. In Appendix B, we summarized all parameters of the separable fitted form for coupled

Interaction	t_0 [MeV fm^3]	t_3 [MeV fm$^{3+3\alpha}$]	x_3
CT	-584.1	8330.7	-0.5
CT1	-548.0	7890.13	-0.5
CT2	-565.467	8180.0	-0.5

Table 6.4: Parameters of the contact interaction defined in Eq.(6.39). The set CT was produced for $V_{\text{low-k}}$ [VGM09], while CT1 and CT2 supply $V_{\text{fit}}^{[2,3]}$.

Interaction	ρ_0 [fm^{-3}]	E/A(ρ_0) [MeV]	K [MeV]
$V_{\text{low-k}}$+CT	0.16	-16.0	258
$V_{\text{fit}}^{[2,3]}$+CT1	0.16	-16.1	241.9
$V_{\text{fit}}^{[2,3]}$+CT2	0.156	-16.0	240.5

Table 6.5: Bulk properties of symmetric nuclear matter derived from $V_{\text{low-k}}$ and its separable representation. They are supplemented by the respective contact interaction.

and uncoupled channels. By using the values from both tables shown there one can reproduce the fitted version of $V_{\text{low-k}}^{[2,3]}$ for a given partial wave channel. In the following we will identify the respective separable fitted potential as $V_{\text{fit}}^{[2,3]}$.

In order to check the accuracy of our fit we perform HF calculations of nuclear matter employing $V_{\text{fit}}^{[2,3]}$. The respective binding energy as a function of the density of symmetric nuclear matter are displayed on Fig.6.15 by a dashed-dotted line. One observes that at up to saturation density $\rho_0 \simeq 0.16$ fm^{-3} the fitted potential $V_{\text{fit}}^{[2,3]}$ reproduces the results of $V_{\text{low-k}}^{[2,3]}$ (dashed), while at higher densities it becomes slightly less bound and lies closer to the original $V_{\text{low-k}}$ (solid). Thus the deviation of the fitted separable potential $V_{\text{fit}}^{[2,3]}$ from $V_{\text{low-k}}$ does not exceed 1% of binding energy. Not going into details we mention that the deviation rises mainly from $^3S_1$-$^3D_1$ and $^3P_2$-$^3F_2$ coupled channels.

As we have already seen form Fig.6.15 $V_{\text{low-k}}$ interaction as well as its separable form $V_{\text{fit}}^{[2,3]}$ does not describe the empirical saturation point. To achieve the saturation in nuclear matter one has to add three-body interaction terms or a density-dependent two-nucleon interaction. Therefore we support the low-momentum interaction by a
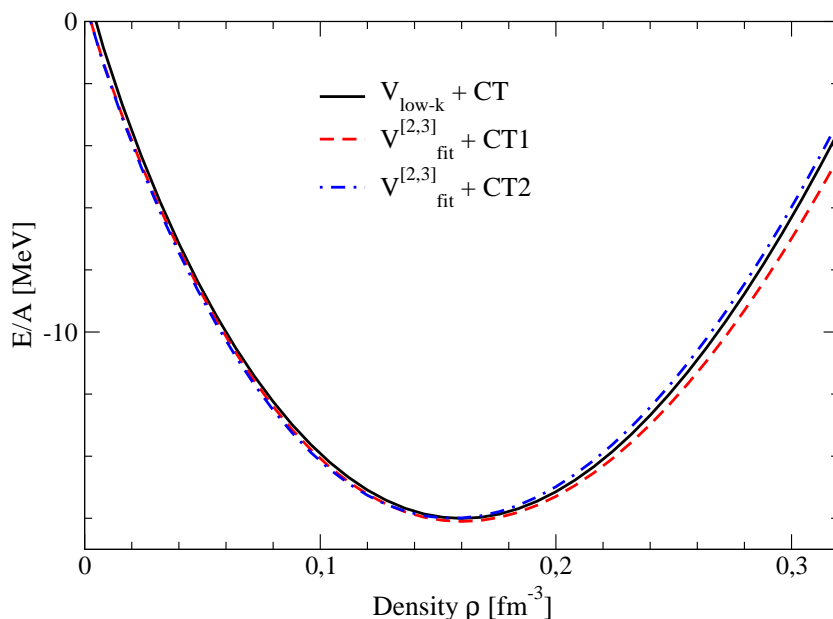
Figure 6.16: Energy per nucleon of symmetric nuclear matter as a function of the density. Results of $V_{\text{low-k}}$ + CT interaction (solid line) compared with the fitted separable form $V_{\text{fit}}^{[2,3]}$ + CT1 (dashed line) and $V_{\text{fit}}^{[2,3]}$ + CT2 (dashed-dotted line).

simple contact interaction (6.39). Following [GV+09] we label by CT the contact interaction produced for $V_{\text{low-k}}$, and the respective interaction model by $V_{\text{low-k}}$+CT. For the fitted potential $V_{\text{fit}}^{[2,3]}$ we suggest two possible parameterizations: CT1 and CT2. Their parameters and properties of nuclear matter are shown in Tables 6.4 and 6.5, respectively.

The interaction $V_{\text{fit}}^{[2,3]}$ + CT1 gives the binding energy per nucleon of symmetric nuclear matter E/A=-16.1 MeV at the density $\rho_0 = 0.16\,\text{fm}^{-3}$. The HF calculations of nuclear matter (see Fig.6.16) for $V_{\text{fit}}^{[2,3]}$ + CT1 give results (dashed line) very similar to the non-separable initial interaction $V_{\text{low-k}}$ + CT (solid line). However, in the calculation of finite nuclei we observe a deviation of about 0.12MeV in the binding energy of light nuclei, like ^{16}O (see Table 6.6). The picture can be improved if we assume, that the saturation density is not defined exactly and allow for a small deviation. Along this line the second parameterization CT2 was produced. The interaction $V_{\text{fit}}^{[2,3]}$ + CT2 gives E/A=-16.0 MeV at the density $\rho_0 = 0.156\,\text{fm}^{-3}$. This corresponds to a small shift of the saturation point with respect to the initial $V_{\text{low-k}}$ interaction (see Fig.6.16). It allows to improve the accuracy in the binding

Interaction	^{16}O	^{40}Ca	^{48}Ca	^{60}Ca	^{208}Pb
	E/A [MeV]				
$V_{\text{low-k}}$+CT	-7.91	-8.57	-8.42	-7.75	-7.76
$V_{\text{fit}}^{[2,3]}$+CT1	-7.79	-8.56	-8.35	-7.78	-7.76
$V_{\text{fit}}^{[2,3]}$+CT2	-7.84	-8.58	-8.37	-7.79	-7.76
Experiment	-7.98	-8.55	-8.67	–	-7.87
	r_{ch} [fm]				
$V_{\text{low-k}}$+CT	2.79	3.50	3.54	3.68	5.51
$V_{\text{fit}}^{[2,3]}$+CT1	2.81	3.51	3.55	3.68	5.52
$V_{\text{fit}}^{[2,3]}$+CT2	2.82	3.53	3.58	3.71	5.56
Experiment	2.74	3.48	3.47	–	5.50

Table 6.6: The binding energy per nucleon and rms charge radii of finite nuclei. Experimental data taken from Refs. [Br98, AW93, Ch+96, Fr+95].

energies of finite nuclei: one can notice that the contact interaction CT2 leads to a better description than CT1. However, comparing the rms charge radii of nuclei in Table 6.6, we see that due to the shift in saturation density the interaction $V_{\text{fit}}^{[2,3]}$ + CT2 yields larger radii than the interaction $V_{\text{fit}}^{[2,3]}$ + CT1.

For all models considered here the compressibility modulus at saturation density is in the range $240.5 \leq K \leq 258$ MeV. This means that the respective equations of state (EoSs) displayed in Fig.6.16 are rather soft, at least at densities up to about two times saturation density. Such a prediction of a soft EoS is in agreement with data extracted from heavy ion reactions. For example, heavy ion data for transverse flow [St+04] or from kaon production [St+01] support the picture of a soft EoS in symmetric nuclear matter.

The simple separable form of $V_{\text{low-k}}$ constructed here can significantly simplify the Hartree-Fock calculations. In the nearest future this permits us to make one step further in our study, towards the investigation of inhomogeneous nuclear matter and its exotic shapes, which merge under extreme pressure, density, and temperature in the inner crust of neutron stars.

Chapter 7

Summary and Outlook

The properties of nuclear matter under extreme conditions is one of the most important ingredient for the study of compact objects in modern astrophysics. The knowledge of the EoS is of high relevance for the treatment of the astrophysical phenomena such as neutron stars or supernovae core collapse. Recently a significant progress in understanding of the nature of compact stars was achieved by using the standard methods of the many-body nuclear physics.

In early eighties the existence of the inhomogeneous nuclear matter, which is also known as the pasta phase, in supernovae and in the crust of neutron stars was predicted in the Thomas-Fermi calculations. This opened a new era in the application of the many-body technique to the astrophysical environment. It is expected that the existence of the pasta phase will play a crucial role in neutrino transport properties, which are an essential ingredient in the description of the gravitational collapse of supernovae and the cooling of young neutron stars. In spite of the significant achievements in numerical simulations there still exist, however, plenty of questions of fundamental interest: How does the pasta phase influence the neutrino opacity? What is the proton fraction in the crust of neutron stars? What is the range of temperatures and densities over which the pasta phase exits? How strong is the model dependence in the nuclear matter calculations? Some of these questions were covered in the present work.

In the first part of this Thesis the properties of the inhomogeneous nuclear matter and their influence on the neutrino propagation have been investigated. The structure of the charge neutral baryonic matter, containing protons, neutrons and

electrons is considered performing the Skyrme Hartree-Fock calculations with the inclusion of pairing correlations and finite temperatures in a periodic lattice of WS cells of cubic shapes. This allows to observe a smooth transition from the neutron rich nuclei embedded in neutron sea, which exist in the outer crust, to the homogeneous matter, which appears at higher densities. The symmetries of the WS cell allow the existence of the non-spherical quasinuclear structures, like cylindrical rods and planar slabs. Forming such shapes the energy is reduced compared to the homogeneous matter distribution. The result of the Hartree-Fock calculations at the finite temperatures is that all pasta structures disappear at the temperature about 15 MeV. This critical temperature was found to be in agreement with relativistic calculations by other groups. Thus, these effects of the pasta phase become relevant after a young and hot neutron star is cooled down to this temperature.

The Skyrme Hartree-Fock calculations within the WS cell approximation provide us with the information about the pasta phase structure on a single-particle level. The resulting single-particle energies and wave functions of nucleons can be used as a solid starting point for further studies of the neutrino-pasta interaction and neutrino opacity. In this Thesis the neutrino mean free path is extracted from the total cross section of neutrinos on the volume of WS cell. The cross section, in its turn, is derived from the Fermi and Gamow-Teller transition matrix elements for the charged current absorption and neutral current scattering reactions. Due to the absence of the spherical symmetry the mean free path has been averaged over the spatial orientations. It was found that the existence of the pasta phase inside the crust affects the NMFP mainly through the charged current reaction. The variational calculations for pasta structure yield larger proton fractions, in comparison with the homogeneous matter at the same global density. Consequently the WS cell with the inhomogeneous matter distribution contains a larger number of electrons. This reduces the number of possible transitions in the charged current reaction, since the blocking effect for the final electrons should be taken into account. It leads to a longer mean free path in the inhomogeneous nuclear matter in comparison to the homogeneous one. The described mechanism emphasizes the role of the proton fraction in neutrino propagation. It was also found that the effect of inhomogeneous density distributions is less pronounced for the neutral current reaction.

The model dependence of the results has been tested by imploying relativistic mean-

field calculations as an alternative. Within the relativistic model with the density-dependent coupling constants only two pasta structures have been observed: spherical droplets and cylindrical rods. The proton fraction of the inhomogeneous matter was found to be closer to the homogeneous matter predictions, so that its influence in the charged current reaction becomes less significant as in the non-relativistic Skyrme model.

The phenomenological models, being adjusted to the experimental data on finite nuclei and empirical saturation point of nuclear matter possess rather a limited predictive power in determination of the EoS at high densities. Therefore the nuclear structure calculations should be performed with the realistic forces constructed to describe the experimental scattering data. In this connection, the realistic low-momentum interaction $V_{\text{low-k}}$ is discussed in details in the second part of the Thesis. This low-momentum potential is constructed from the realistic models of NN interaction, by introducing a cutoff Λ in momentum space, and integrating out the high-momentum components of the initial interaction. It was found that with the cutoff in the range of $\Lambda = 2 \text{ fm}^{-1}$ $V_{\text{low-k}}$ becomes model independent, and reproduces the deuteron binding energy, low-energy phase shifts, and half-on-shell T matrix with the same accuracy as the initial realistic interaction. The absence of strong short-range components in $V_{\text{low-k}}$ allows to involve this potential in the standard Hartree-Fock calculations.

The $V_{\text{low-k}}$ Hartree-Fock calculations demonstrate a monotonic increase of binding energy of symmetric nuclear matter as a function of the nucleonic density, thus the empirical saturation point cannot be reproduced. Therefore $V_{\text{low-k}}$ interaction was supplemented by a simple density-dependent contact term (CT), which accounts for the three-body correlations. The parameters of the contact term are adjusted to the saturation point and compressibility of the nuclear matter. Finally, the Hartree-Fock calculations with the interaction model $V_{\text{low-k}} + \text{CT}$ allow to describe the bulk properties of nuclear matter as well as the bulk properties and the single-particle structure of finite nuclei fairly well.

$V_{\text{low-k}}$ is nonlocal and therefore is represented in terms of a matrix elements in momentum space for each partial wave channel. This nonlocality increases the computational time in the self-consistent Hartree-Fock calculations, so that it prevents the use of $V_{\text{low-k}}$ in calculations of the EoS in the crust for a wide range of densities.

This situation can significantly be improved if a separable form of $V_{\text{low-k}}$ is found. The separability of $V_{\text{low-k}}$ has been investigated by using the diagonalization of matrix in the momentum space for each partial wave channel. It was found that at $\Lambda = 2$ fm^{-1} the low-momentum interaction can be accurately approximated by a low-rank separable interaction. The later can be used in the Hartree-Fock calculations of the nuclear matter as well as the finite nuclei. This separable form of $V_{\text{low-k}}$ is parameterized in a simple way to make it accessible for various nuclear structure calculations.

In the nearest future $V_{\text{low-k}}$ potential will be used in calculations of the pasta phase. Furthermore, by using the separable version of $V_{\text{low-k}}$ the detailed investigation of the equation of state with inclusion of the inhomogeneous nuclear matter can be performed. This will allow to test the predictions of the phenomenological models. In parallel, one can explore the transformation of $V_{\text{low-k}}$ from the momentum to the coordinate space by using the Fourier-Bessel transform. Starting with a separable interaction in k-space one obtains a separable interaction in r-representation. The latter can be used in construction of a new type of the phenomenological models.

Appendix A

In this Appendix we consider the calculation of the NMFP in noninteracting nuclear matter for charged current reaction $\nu + n \rightarrow e^- + p$. The matrix element of this reaction is given in terms of the current-current interaction

$$M_{fi} = \frac{G_F \cos\theta_C}{\sqrt{2}} j^\mu J_\mu, \tag{7.1}$$

where the leptonic and baryonic currents are

$$j^\mu = \bar{u}_e \gamma^\mu (1 - \gamma_5) u_\nu, \tag{7.2}$$

$$J_\mu = \bar{u}_p (g_V \gamma_\mu - g_A \gamma_\mu \gamma_5) u_n, \tag{7.3}$$

with $G_F = 1.66 \times 10^{-11} MeV^{-2}$ is the Fermi constant, $g_V = 1$ and $g_A = 1.23$. Thus the squared matrix element $|M_{fi}|^2$ is given by

$$|M_{fi}|^2 = \frac{G_F^2 \cos^2\theta_C}{2} [\bar{u}_e \gamma^\mu (1 - \gamma_5) u_\nu][\bar{u}_\nu \gamma^\nu (1 - \gamma_5) u_e] \tag{7.4}$$

$$\times \quad [\bar{u}_p (g_V \gamma_\mu - g_A \gamma_\mu \gamma_5) u_n][\bar{u}_n (g_V \gamma_\nu - g_A \gamma_\mu \gamma_5) u_p] \tag{7.5}$$

Now one should average over initial and sum up over final states

$$|\bar{M}_{fi}|^2 = \frac{G_F^2 \cos^2\theta_C}{4} Tr[(\hat{p}_e + m_e)\gamma^\mu (1 - \gamma^5)\hat{p}_\nu (1 + \gamma^5)\gamma^\nu] \tag{7.6}$$

$$\times \quad Tr[(\hat{p}_p + m_p)\gamma_\mu (g_V - g_A \gamma^5)(\hat{p}_n + m_n)(g_V + g_A \gamma^5)\gamma_\nu], \tag{7.7}$$

where we used the notation $\hat{p}_i = u_i \gamma^\alpha$. Further calculation involves the standart evaluation of traces with γ-matrices, which can be found in [Ma05]. At the end we arrive to

$$|\bar{M}_{fi}|^2 = 16 G_F^2 \cos^2\theta_C \tag{7.8}$$

$$\times \quad [(g_V + g_A)^2 (E_e E_p - E_e p_p \cos\theta_{ep})(E_\nu E_n - p_n E_\nu \cos\theta_{\nu n}) \tag{7.9}$$

$$+ \quad (g_v - g_A)^2 (E_n E_e - p_n E_e \cos\theta_{ne})(E_\nu E_p - E_\nu p_p \cos\theta_{\nu p}) \tag{7.10}$$

$$- \quad (g_V^2 - g_A^2) m_p m_n (E_\nu E_e - E_\nu E_e \cos\theta_{\nu e})], \tag{7.11}$$

where $\cos \theta_{ij}$ is the angle between momenta of i-th and j-th particles. Afterwards the transition rate from initial to final states can be written as

$$\mathcal{T}_{fi} = \frac{|\bar{M}|^2}{16 E_\nu E_n E_e E_p}. \tag{7.12}$$

Inserting (7.8) in (7.12)

$$\begin{align}
\mathcal{T}_{fi} &= G_F^2 \cos^2 \theta_C [(g_V + g_A)^2 (1 - v_p \cos \theta_{ep})(1 - v_n \cos \theta_{\nu n}) \tag{7.13} \\
&+ (g_v - g_A)^2 (1 - v_n \cos \theta_{ne})(1 - v_p \cos \theta_{\nu p}) \tag{7.14} \\
&- (g_V^2 - g_A^2) m_p m_n (1 - \cos \theta_{\nu e})], \tag{7.15}
\end{align}$$

where we used nucleon velocities $v_i = p_i/E_i$. Since we consider nonrelativistic baryons ($v_i/c << 1$) the terms proportional to v_i can be simply neglected.

$$\mathcal{T}_{fi} = G_F^2 \cos^2 \theta_C [g_V^2 + 3g_A^2 + (g_V^2 - g_A^2) \cos \theta_{\nu e}]. \tag{7.16}$$

We can also omit the last term since it is proportional to $g_V^2 - g_A^2$. The cross section per unit volume or the inverse neutrino mean free path thus can be written

$$\frac{1}{\lambda} = \frac{\sigma(E_\nu)}{V} = G_F^2 \cos^2 \theta_C \int \frac{d^3 p_e}{(2\pi)^3} (1 - f(E_e))[g_v^2 + 3g_A^2] S(q, \omega), \tag{7.17}$$

where $f(E_i)$ stands for the Fermi-Dirac distribution

$$f(E_i) = \frac{1}{1 + \exp \left(\frac{E_i - \mu_i}{T} \right)} \tag{7.18}$$

and

$$S(q, \omega) = 2 \int \frac{d^3 p_p}{(2\pi)^3} \int \frac{d^3 p_n}{(2\pi)^3} (1 - f(E_p)) f(E_n) (2\pi)^4 \delta^4 (p_1 + p_2 - p_3 - p_4) \tag{7.19}$$

The function $S(q, \omega)$ is the so-called dynamic form factor and it characterizes the response of the system to the external probe with momentum transfer q and energy ω. In the charged current reaction $\vec{q} = \vec{q}_e - \vec{q}_\nu$ and $\omega = E_e - E_\nu$. By using the relation

$$d^3 p_e = 2\pi q (E_e/E_\nu) d\omega dq \tag{7.20}$$

we obtain

$$\frac{1}{\lambda} = \frac{G_F^2 \cos^2 \theta_C}{4\pi^2} (g_V^2 + 3g_A^2) \int_{-\infty}^{E_\nu} d\omega E_e/E_\nu (1 - f(E_e)) \int_{|\omega|}^{2E_\nu - \omega} dq q S(q, \omega) \tag{7.21}$$

The calculation of the response function is rather strightforward and we skip the details which can be found, e.g., in [RPL98]. The result is

$$S(q,\omega) = \frac{\frac{m^2 T}{\pi q}}{1 - \exp\left(-\frac{\omega}{T} - \frac{\mu_n - \mu_p}{T}\right)} ln \left[\frac{1 + \exp\left(\frac{\mu_n}{T} - \frac{m}{2q^2 T}(\omega - \frac{q^2}{2m})^2\right)}{1 + \exp\left(\frac{\mu_p}{T} - \frac{m}{2q^2 T}(\omega + \frac{q^2}{2m})^2\right)}\right] \quad (7.22)$$

Relations (7.21) and (7.22) determine the NMFP and response function of free fermi gas at finite temperature. In the limit of zero temperature the Fermi-Dirac distribution must be replaced by the θ-function and this particular solution for the response function is considered in [FW71].

Appendix B

Parameters for the fitted separable version of $V_{\text{low-k}}$.

Channel	i	a_i	α_i	β_i	γ_i	δ_i	μ_i	σ_i	λ_i
$^1S_0$	1	-0.16344E+02	0.10772E-03	-0.43234E-03	0.17650E+00	0.92610E+00	0.10316E-02	0.99335E+00	0.14191E+01
	2	-0.66770E+00	-0.20749E-03	-0.18295E-01	0.66232E-01	0.86815E+00	0.20236E-01	0.17925E+01	0.11085E+01
$^1P_1$	1	0.15105E+01	0.41103E-04	-0.30056E-02	0.46402E-01	0.12591E+01	0.36618E-02	0.22676E+01	-0.66286E-02
	2	0.14569E+02	-0.36052E-02	0.12380E-02	0.30093E+00	0.15720E+01	0.24098E-02	0.46996E+00	0.14196E+01
$^3P_0$	1	-0.36339E+01	0.12254E-03	0.20982E-03	-0.59888E+00	0.10769E+01	0.30373E-03	-0.21878E+01	0.96652E+01
	2	0.36518E+01	0.34915E-04	-0.39191E-03	0.74648E-01	0.35155E+01	0.35779E-03	0.20292E+01	0.14199E+01
$^3P_1$	1	0.11011E+01	-0.44421E-03	0.18896E-02	-0.63158E+00	0.24471E+01	0.94546E-04	0.73498E+00	0.22558E+00
	2	0.15410E+02	-0.33598E-03	0.15182E-02	-0.12701E-02	0.54199E+01	-0.85450E-03	0.59810E+00	0.52799E+00
$^1D_2$	1	-0.47228E+01	0.23948E-03	0.11514E-02	0.78532E-01	0.83080E+00	-0.14043E-02	0.15502E+01	0.12639E+01
	2	-0.42720E+00	0.43276E-03	-0.13308E-02	-0.76108E+00	0.22797E+01	0.89215E-03	0.12810E+01	0.17046E+01
$^3D_2$	1	-0.14755E+02	0.23661E-03	-0.16214E-03	-0.20028E+00	0.47727E+01	-0.79636E-04	0.12915E+01	0.17118E+01
	2	-0.20625E+01	0.46873E-03	-0.13299E-02	-0.70797E+00	0.22075E+01	0.85842E-03	0.14395E+01	0.16497E+01
$^1F_3$	1	0.45580E+00	0.45434E-03	0.34263E-02	-0.23846E-01	-0.12925E+01	-0.45576E-03	0.18623E+01	0.14425E+01
	2	0.21276E+01	0.11682E-03	-0.24864E-03	-0.15328E+01	-0.76112E+00	-0.11725E-03	0.20029E+01	0.14366E+01
$^3F_3$	1	0.26740E+00	0.44076E-03	0.35397E-02	-0.24171E+01	-0.12481E+01	-0.44204E-03	0.18298E+01	0.14500E+01
	2	0.11895E+01	0.12811E-03	-0.89537E-04	-0.63186E+00	-0.13835E+01	-0.12893E-03	0.20960E+01	0.13909E+01
$^1G_4$	1	-0.56713E+00	0.93511E-04	-0.32673E-03	-0.14289E+01	-0.10215E+01	-0.94613E-04	0.19148E+01	0.13505E+01
	2	-0.09176E+00	0.92267E-02	-0.14963E-01	-0.55660E+01	-0.18735E+01	-0.92335E-02	-0.37857E+00	0.16284E+01
$^3G_4$	1	-0.30270E+01	0.10774E-03	-0.16121E-03	-0.77810E+00	-0.15648E+01	-0.10940E-03	0.18745E+01	0.13214E+01
	2	-0.5061E+00	0.10191E-03	-0.62066E-03	-0.10817E+01	-0.10648E+01	-0.10392E-03	0.31194E+01	0.13385E+01
$^1H_5$	1	0.01455E+01	0.99849E-04	-0.38155E-03	-0.64624E+00	-0.24138E+01	-0.10803E-03	0.33677E+01	0.95975E+00
	2	0.06095E+01	0.14458E-06	-0.43467E-03	-0.30481E+00	0.34986E+01	0.43536E-03	0.13486E+01	-0.29605E+00
$^3H_5$	1	0.00727E+00	0.86739E-04	-0.36173E-03	-0.88687E+00	0.29817E+01	0.45115E-03	0.32408E+01	-0.20198E+01
	2	0.03736E+01	0.17206E-06	-0.45636E-03	-0.28889E+00	0.34083E+01	0.45708E-03	0.13780E+01	-0.31990E+00
$^1I_6$	1	-0.01407E+01	0.18615E-04	-0.27820E-04	0.15265E+01	0.97282E+00	0.15276E-04	0.20513E+01	0.15767E+01
	2	-0.00281E+01	0.63551E+00	-0.26703E+00	0.18734E+00	0.19309E+01	-0.36758E+00	0.39862E+00	0.15760E+01
$^3I_6$	1	-0.08297E+01	-0.18713E-04	-0.30695E+00	0.31341E-03	0.21961E+01	0.30694E+00	0.19374E+01	0.16207E+01
	2	-0.0153E+01	0.94460E-04	-0.30640E+00	0.53129E-03	0.14854E+01	0.30630E+00	0.33132E+01	0.79134E+00

Parameters of $V_{\text{fit}}^{[2,3]}$ for uncoupled channels. See Eq.(6.58).

Channel	i	a_i	α_i	β_i	γ_i	δ_i	μ_i	σ_i	λ_i
$^3S_1$	1	-0.39195E+02	0.14710E-03	-0.27882E-02	0.10166E+00	0.98761E+00	0.33148E-02	0.73493E+00	0.91775E+00
	2	-0.46417E+01	-0.21867E-04	0.31258E+00	0.17566E-02	0.78784E+00	-0.31368E+00	0.18855E+01	0.11761E+01
	3	0.20913E+02	-0.97562E-04	0.33292E+00	0.50609E-03	0.87732E+00	-0.33339E+00	0.14274E+01	0.12444E+01
$^3D_1$	1	-0.39195E+02	0.90122E-04	0.31369E-05	0.38917E-03	0.12444E+02	-0.93123E-04	0.13384E+01	0.15561E+01
	2	-0.46417E+01	-0.22645E-03	-0.41235E+00	0.40973E-03	0.18283E+01	0.41258E+00	0.15668E+01	0.15335E+01
	3	0.20913E+02	0.11207E-03	-0.13705E-04	0.48296E+00	0.24592E+01	-0.97861E-04	0.21818E+01	0.15329E+01
$^3P_2$	1	-0.11712E+02	-0.12771E-01	0.74967E-02	0.29157E-01	0.83736E+00	0.53084E-02	0.11992E+00	0.14904E+01
	2	-0.21898E+01	-0.92101E-04	0.28219E+00	0.19554E-02	0.11980E+01	-0.28296E+00	0.12014E+01	-0.12709E+00
	3	0.17808E+01	0.14009E-03	0.34622E+00	0.13719E-02	0.12162E+01	-0.34694E+00	0.12159E+01	0.29393E+01
$^3F_2$	1	-0.11712E+02	-0.37975E-09	-0.26753E-09	0.11862E+02	0.11520E+00	-0.69054E-05	0.10568E+01	-0.53109E+00
	2	-0.21898E+01	0.71589E-04	-0.98497E-14	0.22438E+02	0.54423E-01	-0.69308E-04	-0.23032E+01	-0.46525E+01
	3	0.17808E+01	0.24733E-03	-0.69363E-04	0.12429E+01	0.45015E+00	0.40433E-03	0.11919E+01	0.40019E+01
$^3D_3$	1	-0.60466E+01	0.18332E-03	0.14266E+00	0.41443E-03	0.17445E+01	-0.14284E+00	0.21656E+01	0.15038E+01
	2	0.91410E+00	-0.11606E-03	0.18114E+00	-0.13213E+00	0.12510E-02	-0.15901E+00	0.33728E+01	-0.79666E+00
	3	0.54641E+01	-0.27373E-03	-0.45681E+00	0.67993E-03	0.90916E+00	0.45713E+00	0.18906E+01	0.99510E+00
$^3G_3$	1	-0.60466E+01	0.41921E-04	-0.65759E-01	0.79378E-03	0.18207E+01	0.65717E-01	0.14240E+01	0.16750E+01
	2	0.91410E+00	0.78827E-04	-0.73989E-01	-0.17382E-02	0.15332E+01	0.74065E-01	0.30794E+01	-0.18745E+01
	3	0.54641E+01	0.15808E-03	-0.16419E+00	-0.10345E+00	-0.99477E+00	0.28959E-03	0.19522E+01	-0.25907E+01
$^3F_4$	1	-0.16095E+01	0.18033E-03	0.37879E+00	-0.39428E-03	0.37390E+00	-0.37852E+00	0.21928E+01	-0.23390E+01
	2	-0.30360E+00	-0.32058E-03	-0.11873E+01	0.28972E-03	0.16371E+01	0.11877E+01	0.20173E+01	0.11166E+01
	3	0.56160E+00	0.24168E-03	-0.11138E+01	-0.80823E-04	0.27458E+01	0.11135E+01	0.19919E+01	0.13089E+01
$^3H_4$	1	-0.16095E+01	0.30449E-07	0.28581E-01	-0.69621E+01	-0.54467E+00	0.15057E-05	0.10041E+01	0.30546E+01
	2	-0.30360E+00	-0.14910E-02	0.20920E+00	0.26023E-02	0.24400E+01	-0.20770E+00	0.59266E+00	0.16380E+01
	3	0.56160E+00	0.17531E-04	0.22351E+00	0.34114E-03	0.19278E+01	-0.22349E+00	0.16346E+01	-0.12499E+01
$^3G_5$	1	-0.12501E+01	0.13111E-03	-0.13521E+00	-0.10757E+00	0.10162E-02	0.12130E+00	0.28269E+01	0.70560E+00
	2	0.30880E+00	-0.31841E-03	-0.53598E+00	0.61243E-03	0.18397E+01	0.53633E+00	0.23654E+01	0.99154E+00
	3	0.16137E+01	-0.93523E-04	-0.48952E+00	-0.88510E-04	0.10928E+01	0.48961E+00	0.25801E+01	0.11545E+01
$^3I_5$	1	-0.12501E+01	0.19169E-04	0.29512E+00	0.15469E-03	0.26251E+01	-0.29510E+00	0.17038E+01	-0.16316E+01
	2	0.30880E+00	0.38821E-04	0.36156E+00	0.35017E-03	0.19665E+01	-0.36153E+00	0.30449E+01	-0.21756E+01
	3	0.16137E+01	0.14023E-04	0.36754E+00	-0.14039E-03	0.25880E+01	-0.36755E+00	0.17978E+01	0.15991E+01
$^3H_6$	1	-0.30540E+00	-0.65438E-03	0.65143E+00	0.56031E-03	0.23634E+01	-0.65075E+00	0.48747E+00	0.18318E+01
	2	-0.63700E-01	0.25601E-03	0.39808E+00	0.29243E-03	0.32313E+01	-0.39836E+00	0.22583E+01	0.10325E+01
	3	0.20960E+00	0.61333E-04	0.25966E+00	-0.32893E-03	0.13102E+01	-0.25972E+00	0.25754E+01	0.11963E+01
$^3K_6$	1	-0.30540E+00	-0.10269E-04	0.23504E+00	0.14785E-03	0.31131E+01	-0.23503E+00	0.18245E+01	0.14457E+01
	2	-0.63700E-01	-0.19663E-04	0.26322E+00	0.39336E-03	0.23907E+01	-0.26320E+00	0.29488E+01	0.91309E+00
	3	0.20960E+00	0.12093E-04	-0.36799E+00	0.11473E-03	0.30036E+01	0.36798E+00	0.18060E+01	0.14804E+01

Parameters of $V_{\text{fit}}^{[2,3]}$ for coupled channels. See Eq.(6.58).

Bibliography

[AC+77]   W. M. Alberico, R. Cenni, V. R. Manfredi, A. Molinari, Il Nuovo Ci-
           mento **40A** 449 (1977).

[AHI08]   S. Aoki, T. Hatsuda and N. Ishii, Comp. Sci. Dis. 1, 015009 (2008).

[AP+98]   A. Akmal, V. R. Pandharipande, and D. G. Ravenhall, Phys. Rev. C **58**,
           1804 (1998).

[AW93]   G. Audi, A. H. Wapstra, Nucl. Phys. **A565** 1 (1993).

[Ba99]   M. Baldo, in *Nuclear Methods and the Nuclear Equation of State*, edited
           by M. Baldo (World Scientific 1999).

[BBP71]   G. A. Baim, H. A. Bethe and C. J. Pethick, Nucl. Phys. **A175** 225
           (1971).

[BB+]   S. R.Beane, P. F. Bedaqua, W. C. Haxton, D. R. Phillips, and M. J.
           Savage, At the Frontier of Particle Physics, Ed. M. Shifman, Vol. 1, p.
           133, World Scientific, arXiv:nucl-th/0008064.

[BCS57]   J. Bardeen, L. N. Cooper, J. R. Schrieffer, Phys. Rev. **108** 1175 (1957).

[BC+90]   M. Baldo, J. Cugnon, A. Lejeune und U. Lombardo, Nucl. Phys. **A515**
           409 (1990).

[BC09]   O. Benhar, A. Carbonne, arXiv:nucl-th/0912.0129 (2009).

[BDM06]   P. Boźek, D. J. Dean, and H. Müther, Phys. Rev. C **74**, 014303 (2006).

[BE91]   G. F. Bertsch and H. Esbensen, Ann. Phys. **209** 327 (1991).

[BF88]   M. Baldo and L. S. Ferreira, Nucl. Phys. **A480**, 271 (1988).

[BF+85]   P. Bonche, H. Flocard, P.-H.Heenen, S. J. Krieger, M. S. Weiss, Nucl. Phys. **A443** 39 (1985).

[BF+08]   S. K. Bogner, R. J. Furnstahl, and A. Schwenk, arXiv:nucl-th/0806.1365 (2008).

[BF+85]   P. Bonche, H. Flocard, P.-H. Heenen, S. J. Krieger, and M. S. Weiss, Nucl. Phys. **A443** 39 (1985).

[BK00]   S. K. Bogner and T. T. S. Kuo, arXiv:nucl-th/0009077v2 (2000).

[BK+01]   S. K. Bogner, T. T. S. Kuo and L. Coraggio, Nucl. Phys. **A684** 432 (2001).

[BK+02]   S. K. Bogner, T. T. S. Kuo, L. Coraggio A. Covello and N. Itaco, Phys. Rev. C **65** 05130(R) (2002).

[BK+03]   S. K. Bogner, T. T. S. Kuo, and A. Schwenk, Phys. Rep **386**, 1 (2003).

[BL+05]   M. Baldo, U. Lombardo, E. E. Saperstein, and S. V. Tolokonnikov, Nucl. Phys. **A750** 409 (2005).

[BL55]   K. A. Brueckner and C. A. Levinson, Phys. Rev. **97**, 1344 (1955).

[BM+87]   A. Bouyssy, J.-F. Mathiot, N. Van Giai, and S. Marcos, Phys. Rev. C **36** 380 (1987).

[BM89]   D. Bonatsos, and H. Müther, Nucl. Phys. **A496**, 23 (1989).

[BM84]   R. Brockmann and R. Machleidt, Phys. Lett. **B149**, 283 (1984).

[Bo81]   J. Boguta, Phys. Lett. **B106**, 255 (1981); J. Lattimer, C. Pethik, M. Prakash and P. Haensel, Phys. Lett. **66**, 201 (1991).

[Br54]   K. A. Brueckner, Phys. Rev. **96**, 508 (1954), *ibid.* **100**, 36 (1955).

[Br98]   B. A. Brown, Phys. Rev. C **58**, 220 (1998).

[BRT06]   A. Burrows, S. Reddy and T. Thompson, Nucl. Phys. **A 777**, 356 (2006).

112

[BS+01]   S. K. Bogner, A. Schwenk, T. T. S. Kuo, and G. E. Brown, arXiv:nucl-th/0111042 (2001).

[BS+05]   S. K. Bogner, A. Schwenk, R. J. Furnstahl, and A. Nogga, Nucl. Phys. **A763**, 59 (2005).

[BV81]   P. Bonche, D. Vautherin, Nucl. Phys. **A372** 496 (1981).

[BZ34]   W. Baade, F. Zwicky, Proceeding of the National Academy of Science **20**, 254 (1934).

[CBH06]   O. L. Caballero, D. K. Berry and C. J. Horowitz, Phys. Rev. C **74**, 065801 (2006).

[CB+97]   E. Chabanat, P. Bonche, P. Haensel, J. Meyer, and R. Schaeffer, Nucl. Phys. **A627**, 710 (1997).

[CC+70]   F. Coester, S. Cohen, B. D. Day, and C. M. Vincent, Phys. Rev. C **1**, 769 (1970).

[Ch32]   J. Chadwick, Nature **129**, 312 (1932).

[Ch+96]   M. Chartier *et al.*, Phys. Rev. Lett. **77**, 2400 (1996).

[CI+03]   L. Coraggio, N. Itaco, A. Covello, and A. Sedrakian, Nucl. Phys. **A723** 32 (2003).

[CN+08]   N. Chamel, S Naimi, E. Khan and J. Margueron, Phys. Rev. C **75**, 055806 (2008).

[DD96]   J. Dobaczewski and J. Dudek, Acta Phys. Pol. **B27** (1996).

[DF+80]   K. T. R. Davies, H. Flocard, S. Krieger and M. S. Weiss, Nucl. Phys. **A342**, 111 (1980).

[DG95]   R. M. Dreizler, E. K. U. Gross, Density Functional Theory, Plenum Press New York, 1995.

[DM92]   D. H. Dickhoff and H. Müther, *Reports on Progress in Physics* **11**, 1947 (1992).

[DV05]   W. H. Dickhoff and D. Van Neck, *Many-Body Theory Exposed!* (World Scientific, Singapore, 2005).

[EG70]   J. M. Eisenberg and W. Greiner, *Excitation Mechanisms of the Nucleus* (North-Holland Publishing Company, Amsterdam-London, 1970).

[EGM00]   E. Epelbaum, W. Glockle, and U.-G. Meissner, Nucl. Phys. **A671** 295 (2000).

[EH98]   Ø. Elgarøy, M. Hjorth-Jensen, Phy. Rev. C **57** 1174 (1998).

[EM01]   D. R. Entem, and R. Machleidt, Phys. Lett. **B524** 93 (2001).

[EM03]   D. R. Entem and R. Machleidt, Phys. Rev. C **68**, 041001(R) (2003).

[Fa08]   N. Farina, PhD Thesis, Universita di Roma, 2008.

[Fe69]   E. Feenberg, in *Theory of Quantum Fluids*, (Academic Press 1969).

[FF98]   S. Fantoni and A. Fabrocini, in *Microscopic Quantum Many-Body Theories and Their Applications,* eds. J. Navarro and A. Polls (Springer 1998).

[FF⁺08]   A. Fabrocini, S. Fantoni, A. Yu. Illarionov, K. E. Schmidt, Nucl. Phys. **A803**, 137 (2008).

[FN⁺97]   H. Feldmeier, T. Neff, R. Roth, and J. Schnack, Nucl. Phys. **A632** 61 (1998).

[FOS04]   S. Fujii, R. Okamoto, and K. Suzuki, Phys. Rev. C **69** 034328 (2004).

[Fr74]   D. Z. Freedman, Phys. Rev. D **9** 1389 (1974).

[Fr⁺95]   G. Fricke *et al.,* Data. Nucl. Data Tables **60**, 177 (1995).

[FW71]   A. L. Fetter and J. D. Walecka, Quantum Theory of Many-Particle Systems, McGraw-Hill, New-York, 1971.

[G07]   P. Gögelein, PhD Thesis, University of Tübingen, 2007.

[Go57]   J. Goldstone, Proc. Roy. Soc. (London), **A239** 267 (1957).

[Gl00]   N. K. Glendenning, *Compact Stars* (2nd edition), Springer, New York, 2000.

[Go81]   A. L. Goodman, Nucl. Phys. **A352** 30 (1981).

[GM07]   P. Gögelein and H. Müther, Phys. Rev. C **76**, 024312 (2007).

[GS⁺99]   E. Garrido, P. Sarriguren, E. Moya de Guerra, and P. Schuck, Phys. Rev. C **60**, 064312 (1999).

[GV⁺08]   P. Gögelein, E. N. E. van Dalen, C. Fuchs, and H. Müther, Phys. Rev. C **77**, 025802 (2008).

[GV⁺09]   P. Gögelein, E. N. E. van Dalen, Kh. Gad, Kh. S. A. Hassaneen, and H. Müther, Phys. Rev. C **79**, 024308 (2009)

[GGM10]   P. Grygorov, P. Gögelein, and H. Müther, J. Phys. G: Nucl. Part. Phys. **37**, 075203 (2010), arXiv:nucl-th/0910.2796.

[GV⁺10]   P. Grygorov, E. N. E. van Dalen, J. Margueron, and H. Müther, arXiv:nucl-th/1003.4126 (2010).

[Ha08]   K. Harada, arXiv:nucl-th/0803.4371v4 (2008).

[HJ62]   T. Hamada and I. D. Johnston, Nucl. Phys. **34**, 382 (1962).

[HK64]   P. Hohenberg, and W. Kohn, Phys. Rev. **136**, B864 (1964).

[HKL01]   F. Hofmann, C. M. Keil and H. Lenske, Phys. Rev. C **64**, 034314 (2001).

[HP84]   J. Haidenbauer and W. Plessas, Phys. Rev. C **30**, 1822 (1984).

[HPP04]   C. J. Horowitz, M. A. Pérez-García and J. Piekarewicz, Phys. Rev. C **69**, 045804 (2004).

[HP⁺05]   C. J. Horowitz, M. A. Pérez-García, D. K. Berry, and J Piekarewicz, Phys. Rev. C **72**, 035801 (2005).

[HT70]   M. I. Haftel, F. Tabakin, Nucl. Phys. **A158** 42 (1970).

[IP82]   N. Iwamoto and C. J. Pethick, Phys. Rev. D **25**, 313 (1982).

[Iv32]   D. D. Ivanenko, Nature **129**, 798 (1932).

[KF⁺06]   H. Kamada, S. Fujii, E. Uzu, M. Yamaguchi, R. Okamoto, and Y. Koike, Prog. Theor. Phys. **115**, 839 (2006).

[KKR79]   C. L. Kung, T. T. S. Kuo, S. Y. Lee, and K. F. Ratcliff, Nucl. Phys. **A176**, 65 (1971).

[KLR71]   T. T. S. Kuo, and K. F. Ratcliff, Phys. Rev. C **19**, 1063 (1979).

[KLR71]   T. T. S. Kuo, S. Y. Lee, and K. F. Ratcliff, Nucl. Phys. **A176**, 65 (1971).

[Kl⁺06]   T. Klähn *et al*, Phys. Rev. C **74**, 035802 (2006).

[KLZ78]   H. Kümmel, K. H. Lührmann, and J. G. Zabolitsky, Phys. Rep. **36**, 1 (1978).

[KM⁺03]   J. Kuckei, F. Montani, H. Müther, and A. Sedrakian, Nucl. Phys. **A723**, 32 (2003).

[KSV05]   E. Khan, N. Sandulesku and N. Van Giai, Phys. Rev. C **71**, 042801 (2004).

[KSW98]   D. B. Kaplan, M. J. Savage, M. B. Wise, Nucl. Phys. **B534**, 329 (1998).

[KS⁺05]   E. Khan, N. Sandulescu and N. Van Giai, Phys. Rev. **C71**, 042801(R) (2005).

[KSO97]   H. Kumagai, K. Suzuki, and R. Okamoto, Prog. Theor. Phys. **97**, 1023 (1997).

[LLZ00]   A. Lejeune, U. Lombardo, and W. Zuo, Phys. Lett. **B477**, 45 (2000).

[LL⁺80]   M. Lacombe, B. Loiseau, J. M. Richard, R. Vinh Mau, J. Cote, P. Pires, and R. de Tourreil, Phys. Rev. C **21**, 861 (1980).

[LS80]   S. Y. Lee and K. Suzuki, Phys. Lett. **B91**, 173 (1980).

[Mac01]   R. Machleidt, Phys. Rev. **C63**, 024001 (2001).

[Ma05]   M. Maggiore, A Modern Introduction to Quantum Field Theory, Oxford University Press, 2005.

[Ma01]   J.Margueron, PhD thesis, University Orsay, (2001).

[MNV02]   J. Margueron, J. Navarro, and N. Van Giai, Phys. Rev. C **66**, 014303 (2002).

[Me65]   N. D. Mermin, Phys. Rev. **137**, A1441 (1965).

[MHE87]   R. Machleidt, K. Holinde, and C. Elste, Phys. Rept. **149**, 1 (1987).

[MH02]   P. Magierski and P.-H. Heenen, Phys. Rev. C **65**, 045804 (2002).

[Mi60]   A. B. Migdal, JETP **10**, 176 (1960).

[MMB90]   H. Müther, R. Machleidt, and R. Brockmann, Phys. Rev. C **42**, 1981 (1990).

[MMM04]   F. Montani, C. May and H. Müther, Phys. Rev. C **69**, 065801 (2004).

[Mo59]   M. Moshinsky, Nucl. Phys. **13**, 104 (1959).

[MP+85]   H. Müther, A. Polls, and T. T. S. Kuo, Nucl. Phys. **A435**, 548 (1985).

[MuP00]   H. Müther and A. Polls, Phys. Rev. C **61**, 014304 (2000).

[MP00]   H. Müther and A. Polls, Prog. Part. Nucl. Phys. **45**, 243 (2000).

[MSS96]   R. Machleidt, F. Sammarruca and Y. Song, Phys. Rev. C **53**, 1489 (1996).

[MVB03]   J. Margueron, I. Vidaña and I. Bombaci, Phys. Rev. C **68**, 055806 (2003).

[NHV99]   J. Navarro, E. S. Hernandéz and D. Vautherin, Phys. Rev. C **60**, 045801 (1999).

[NV72]   J. W. Negele and D. Vautherin, Phys. Rev. C **5**, 1472 (1972); *ibid.* C **11**, 1031 (1975).

[NV73]   J. W. Negele and D. Vautherin, Nucl. Phys. **A207**, 298 (1973).

[O54]   S. Okubo, Prog. Theor. Phys. **12**, 603 (1954).

[O93]   K. Oyamatsu, Nucl. Phys. **A561**, 431 (1993).

[ORK94]   C. Ordonez, L. Ray, U. van Klock, Phys. Rev. Lett. **72**, 1982 (1994).

[Pa$^+$98]   T. -S. Park, et al., Phys. Rev. C **58**, 637 (1998).

[PGR91]   P.-G. Reinhard, Computational Nuclear Physisc 1: Nuclear Structure, edited by K. Langanke, J. A. Maruch and S. E. Koonin, Springer Verlag Berlin (1991).

[PGW06]   D. Page, U. Geppert, F. Weber, Nucl. Phys. **A777**, 497 (2006).

[PM$^+$83]   A. Polls, H. Müther, A. Faessler, T. T. S. Kuo, and E. Osnes, Nucl. Phys. **A401**, 124 (1983).

[PR72]   M. M. Pant and A. K. Rajagopal, Solid State Communications **10**, 1189 (1972)

[PS91]   I. Zh. Petkov, M. V. Stoitsov, Nuclear Density Functional Theory, Clarendon Press Oxford (1991).

[PS64]   J. Da Providencia and C. M. Shakin, Ann. of Phys. **30** 95 (1964).

[RBP00]   S. Reddy, G. Bertsch and M. Prakash, Phys. Lett. **B475**, 1 (2000).

[Re68]   R. V. Reid, Ann. Phys. **50**, 411 (1968).

[RM$^+$03]   J. Rikovska Stone, J. C. Miller, R. Koncewicz, P. D. Stevenson, and M. R. Strayer, Phys. Rev. C **68**, 034324 (2003).

[RPL98]   S. Reddy, M. Prakash, and J. Lattimer, Phys. Rev. D **58**, 013009 (1998).

[RP$^+$99]   S. Reddy, M. Prakash, J. M. Lattimer and J. A. Pons, Phys. Rev. C **59**, 2888 (1999).

[RP$^+$06]   R. Roth, P. Papakonstantinou, N. Paar, H. Hegert, T. Neff, and H. Feldmeier, Phys. Rev. C **73** 044312 (2006).

[RPW83]   D. G. Ravenhall, C. J. Pethick and J. R. Wilson Phys. Rev. Lett. **50**, 2066 (1983).

[RPL98]   S. Reddy, M. Prakash, and J.M. Lattimer, Phys. Rev. **D58** 013009 (1998).

[RS80]   P. Ring and P. Schuck, "The Nuclear Many-Body Problem", Springer-Verlag New York, 1980.

[Sa75]   R. F. Sawyer, Phys. Rev. D **11**, 2740 (1975); *Phys. Rev.* C **40**, 865 (1989).

[SC91]   K. E. Schmidt and D. M. Ceperley, in *Monte-Carlo Methods III*, ed. K. Binder (Springer 1991).

[Sc01]   K. W. Schmid, Eur. Phys. J. A **12**, 29 (2001); *ibid.*, **13**, 319 (2002); *ibid.*, **14**, 413 (2002); *ibid.*, **16**, 475 (2003).

[SG90]   K. W. Schmid, F. Grümmer, Z. Phys. A **337**, 267 (1990).

[Sk59]   T. H. R. Skyrme, Nucl. Phys. **9**, 615 (1959).

[SK$^+$93]   V. Stocks, R. Klomp, m. Rentmeester, and J. de Swart, Phys. Rev. C **48**, 742 (1993).

[SK$^+$94]   V. Stocks, R. Klomp, C. Terheggen, and J. de Swart, Phys. Rev. C **49**, 2950 (1994).

[SL]   J. D. Walecka, *Muon Physics* vol. II ed Highes V H and Wu C S (Academic, New York), 1975; J. C. O'Connell, T. W. Donnelly, and J. D. Walecka, Phys. Rev. C **6**, 719 (1972); T. W. Donnelly and J. D. Walecka, Nucl. Phys. **A274**, 368 (1976); T. W. Donnelly and W. C. Haxton, *Atomic Data Nucl. Data Tables* **23**, 103 (1979).

[SL80]   K. Suzuki and S. Y. Lee, Prog. Theor. Phys. **64**, 2091 (1980).

[SM$^+$03]   J. R. Stone, J. C. Miller, R. Koncewicz, P. D. Stevenson, and M. R. Strayer, Phys. Rev. C **68**, 034324 (2003).

[SM01]   E. Schiller and H. Müther, Eur. Phys. J. **A11**, 15 (2001).

[SO94]   K. Suzuki and R. Okamoto, Prog. Theor. Phys. **92**, 1045 (1994).

[SP07]   J. R. Stone, and P.-G. Reinhard, Prog. Part. Nucl. Phys. **56**, 587 (2007).

[SR91]   K. W. Schmid, P.-G. Reinhard, Nucl. Phys. **A530**, 283 (1991).

[S82]   K. Suzuki, Prog. Theor. Phys. **68**, 246 (1982).

[St⁺04]   G. Stoicea *et al.* (FOPI Collaboration), Phys. Rev. Lett. **92**, 072303 (2004).

[St⁺01]   C. Sturm *et al.* (KaoS Collaboration), Phys. Rev. Lett. **86**, 39 (2001); C. Fuchs, A. Faessler, E. Zabrodin, Y. M. Zheng, *ibid.* **86**, 1974 (2001); C. Fuchs, Prog. Part. Nucl. Phys. **56**, 1 (2006).

[SW⁺07]   H. Sonoda, G. Watanabe, K. Sato, T. Takiwaki, K. Yasuoka and T. Ebisuzaki, Phys. Rev. C **75**, 042801 (2007)

[Ta52]   I. Talmi, Helv. Phys. Acta **25**, 185 (1952).

[Ta93]   I. Talmi, "Simple Models of Complex Nuclei", Harwood Academic Publishers (Chur, Switzerland, 1993).

[TMR09]   Y. Tian, Z.-Y. Ma, and P. Ring, Phys. Rev. C **80**, 024313 (2009).

[TS75]   D. L. Tubbs and D. N. Schramm, Astrophys. J. **201**, 467 (1975).

[VA⁺05]   D. Vretenar, A. Afanasjev, G. A. Lalazissis, and P. Ring, Phys. Rep. **409**, 101 (2005).

[VB72]   D. Vautherin and D. M. Brink, Phys. Rev. C **7**, 626 (1972).

[VDM09]   E. N. E. van Dalen and H. Müther, Phys. Rev. C **80**, 037303 (2009).

[VFF04]   E. N. E. van Dalen, C. Fuchs and A. Faessler, Nucl. Phys. **A744**, 227 (2004).

[VFF07]   E. N. E. van Dalen, C. Fuchs and A. Faessler, Eur. Phys. J. A **31**, 29 (2007).

[VGM09]   E. N. E. van Dalen, P. Gögelein and H. Müther, Phys. Rev. C **80**, 044312 (2009).

[WP⁺00]   R. B. Wiringa, S. C. Pieper, J. Carlson and V. R. Pandharipande, Phys. Rev. C **62**, 044310 (2000).

[WS⁺03]   G. Watanabe, K. Sato, K. Yasuoka and T. Ebisuzaki, Phys. Rev. C **68**, 35806 (2003).

[WS⁺95]   R. Wiringa, V. Stocks, and R. Schiavilla, Phys. Rev. **C 51**, 38 (1995).

[Yu35]   H. Yukawa, Proc. Phys. Math. Soc. Jpn, **17** 48 (1935).

Zusammenfassung

Die Beschreibung der Eigenschaften von Kernmaterie unter exotischen Bedingungen ist ist eine Herausforderung on die Theoretische Kernphysik, die vor allen Dingen durch die moderne Astrophysik gestellt wird. In den letzen drei Jahrzehnten wurden wesentliche Fortschritte in der Untersuchungen und Modellierung von Neutronensternen auf der Basis der kernphysikalischen Ergebnisse erreicht. Von besonderem Interesse ist dabei die Kruste der Neutronensterne, die von aussen nach innen mit zunehmender Dichte den Übergang von isolierten Atomkernen zu einer ausgedehnten Kernmaterie mit konstanter Dichte enthalten sollte.

Beispielsweise sagen Vielteilchen Rechnungen für diesen Bereich die Existenz einer inhomogenen nuklearen Materie, die sogenannte Pasta Phase, vorher. Diese Pasta Phase kann die Beweglichkeit von und die Absorption von Neutrinos und damit die Energietransporteigenschaften stark beeinflussen. Die Berechnung der mittleren freien Weglänge der Neutrinos ist besonders wichtig in Untersuchungen des Kühlungmechanismus und Kühlungsrate eines jungen Sterns.

Im ersten Teil der vorliegenden Dissertation wurde die mittlere freie Weglänge der Neutrinos in neutraler baryonischer Materie untersucht. Die Vielteilchen Rechnungen der inhomogenen Kernmaterie wurden in der Hartree-Fock Näherung mit sogenannten Skyrme Wechselwirkungen in kartesischen Wigner-Seitz (WS) Zellen durchgeführt. Im Dichtebereich zwischen 0.01 und 0.08 fm^{-3} wurden drei Pasta-Strukturen (Droplets, also Knöpfle artige Strukturen baryonischer Materie, Rods, also die Form von Spaghetti und Slabs, in der Form von Lasagne) beobachtet. die von neutronenreichen Kernen biz zu homogener Kernmaterie reichen. Dabei zeigte sich, dass im β-Gleichgewicht der Protonenanteil der inhomogenen Materie höher ist als in der homogenen Kernmaterie bei gleicher Dichte.

Die freie Weglänge wurde aus dem Streuquerschnitt der Neutrinos an der WS Zelle

für geladene und neutrale Reaktionen ausgerechnet. Der Unterschied im Protonenanteil wirkt stark auf die freie Weglänge der Neutrinos in geladener Stromreaktion ein. In der neutralen Stromreaktion spielt die Pasta Phase eine unwesentliche Rolle.

Um die Modellabhängigkeit der Ergebnisse abzuschätzen, wurden ähnliche Rechnungen in einer relativistischen Mittelfeldnäherung durchgeführt. Es zeigt sich, dass die Modellabhängigkeit grösser als die Effekte der inhomogenen Dichteverteilung ist.

Alle phenomenologischen Modelle (wie z.B. das Skyrme Potential), die die experimentellen Daten von endlichen Kernen und den empirischen Sättigungspunkt der symmetrischen Kernmaterie beschreiben, haben einen begrenzten Vorhersagekraft für die verschiedenen Eigenschaften der Kernmaterie unter extremen Bedingungen. Diese Modelle sind rein phenomenologisch und angepasst an die Eigenschaften von normalen Atomkernen. Einer Extrapolation dieser Modelle in Bereiche grösser Baryonendichte und starker Proton-Neutron Asymmetrien ist also mit Vorsicht zu begegnen. In dieser Hinsicht sollten die Vielteilchen Rechnungen auf der Basis von realistischen Nukleon-Nukleon Potentialen durchgeführt werden. Solche realistischen Modelle beschreiben sowohl die zugänglichen Zwei-Nukleon Daten aus der NN-Streuung, als auch die Eigenschaften des Deutrons mit hoher Präzision.

Im zweiten Teil der Dissertation wurden die Hartree-Fock Rechnungen mit der impulsrenommierten Wechselwirkung $V_{\text{low-k}}$ durchgeführt. Dieses Potential enthält keine starken kurzreichweitigen Komponenten und ist daher für die Hartree-Fock Näherung geeignet.

Die $V_{\text{low-k}}$ Hartree-Fock Rechnungen der symmetrischen Kernmaterie zeigen eine wesentliche Überschätzung der Nukleonenbindungsenergie und der Sättigungsdichte. Um diesen Nachteil zu beheben, wurde $V_{\text{low-k}}$ durch einen Kontakt-Term (CT) unterstützt, der die Effekte von Drei-Nukleon Wechselwirkungen darstellt. Die Parameter des Kontaktterms wurden so angepasst, dass die Sättigungseigenschaft symmetrischer Kernmaterie reproduziert wird. Damit erzielt man nicht nur eine erfolgreiche Beschreibung von unendlicher Kernmaterie sondern ist auch in der Lage die Ladungsradien, sowie Bindungsenergien endlicher Kerne in der Hartree-Fock Näherung sehr gut zu beschreiben.

Kernstrukturrechnungen mit diesem erfolgreichen Modell einer realistischen Wechselwirkung sind jedoch nicht einfach. Einerseits ist es ziemlich kompliziert, das $V_{\text{low-k}}$

Potential aus einem realistischen Potential durch die Anwendung von Renormierungsverfahren zu generieren. Andererseits hat diese Wechselwirkung eine nichtlokale Struktur. Deswegen wird sie numerisch für jede Partialwelle im Impulsraum gespeichert. Man umgeht dieses Probleme durch die Benutzung einer separablen Version von $V_{\text{low-k}}$. Im Rahmen der vorliegenden Arbeit wurde eine solche separable Darstellung erarbeitet und in einfacher algebraischer Form parameterisiert. Das ermöglicht eine weitere Anwendung von $V_{\text{low-k}}$ in kernphysikalischen Berechnungen.

In naher Zukunft sollen $V_{\text{low-k}}$, sowie die entsprechende separable Version in Hartree-Fock Berechnungen der Pasta Phase benutzt werden. Solche Berechnungen sollen die Vorhersagen der Skyrme und RMF Modellen überprüfen.

Acknowledgments

Constança Providência, Dr. Jérôme Margueron.

I would like to express my deep thankfulness to my wife Nadia and my parents for their belief and patience during these years.

Curriculum Vitae

Personal information

Name:	Pavlo Grygorov
Nationality:	Ukrainian
Date of Birth:	17.06.1984
Gender:	male
Marital Status:	married
Address:	Fichtenweg 28/401, 72076 Tuebingen
Email:	Pavlo.Grygorov@gmx.de

Academic preparation

07.2007 - till present	PhD Student at the University of Tuebingen. PhD Thesis: "On the transition from nuclear matter to finite nuclei". Scientific advisor: Prof. Dr. H. Müther
09.2005 - 02.2007	MSc. at the Kharkiv National University, Ukraine Master Thesis: "Translationaly invariant description of the elastic form factor and momentum distribution of nucleons in light nuclei with inclusion of short-range correlations". Advisor: Prof. A. Shebeko.
09.2001 - 06.2007	BSc. at the Kharkiv National University, Ukraine Bachelor Thesis: "The center-of-mass correlations in light nuclei". Advisor: Prof. A. Shebeko.

Professional experience

10.2008 - 04.2010	Teaching Assistant. Exercise classes in Mechanics,

Electrodynamics, Quantum Mechanics.

My academic Teachers were the following persons:

I. N. Adamenko, N. A. Azarenkov, N. R. Belyaev, Yu. A. Berezhnoj, V. P. Demut-skij, I. A. Girka, V. A. Girka, V. D. Khodusov, Yu. A. Kirochkin, V. F. Klepikov, A. Yu. Korchin, V. S. Michailenko, H. Müther, K. E. Nemchenko, V. P. Olefir, S. V. Peletminskij, A. V. Shebeko, N. F. Shul'ga, V. A. Slipko, K. N. Stepanov, S. B. Trubnikov, V. G. Zima

Tübingen, 3. Mai 2010